TECHNISCHE UNIVERSITÄT MÜNCHEN
Lehrstuhl Computation in Engineering

Double Experimental Procedure for Model-Specific Finite Element Analysis of the Human Femur and Trabecular Bone

Eduardo Grande García

Vollständiger Abdruck der von der Fakultät für Bauingenieur- und Vermessungswesen der Technischen Universität München zur Erlangung des akademischen Grades eines

Doktor-Ingenieurs

genehmigten Dissertation.

Vorsitzender: Univ.-Prof. Dr.-Ing. habil. F. Duddeck

Prüfer der Dissertation:

1. Univ.-Prof. Dr. rer. nat. E. Rank
2. Priv.-Doz. Dr. med. R. H. H. Burgkart

Die Dissertation wurde am 06.11.2012 bei der Technischen Universität München eingereicht und durch die Fakultät für Bauingenieur- und Vermessungswesen am 22.03.2013 angenommen.

Abstract

Hip replacement (total hip replacement), is a worldwide common surgical procedure in which the hip joint is replaced by a prosthetic implant. Replacing the hip joint consists of replacing both the acetabulum and the femoral head. Such joint replacement orthopaedic surgery generally is conducted to relieve arthritis pain or fix severe physical joint damage as part of hip fracture treatment.

In order to optimize this surgical procedure and the prosthetics used in it, accurate computational models of the bone are needed, which additionally require a large amount of information from the biomechanical field.

The stability of bone depends upon material properties and geometry. One of the major parameters of the material properties is the Young´s (elastic) modulus E. This value describes the deformation under loading for linear elastic behavior.

There are two types of bone tissue regarding its density and porosity: cortical (or compact) bone and trabecular (or cancellous) bone. Cortical bone has a porosity ranging between 5% and 10% and it is usually found along the exterior shaft section of long bones. Cortical bone forms the outer shell around the trabecular bone in joints and in vertebrae (Martin, 1998). Trabecular bone has a porosity ranging from 75% to 90%. It is usually found in cubicoidal bones (such as vertebrae), flat bones (such as the pelvis) at the end of long bones (such as the femur). Cortical bone accounts for about 80% of the total skeletal mass while trabecular bone constitutes some 70% for the skeletal volume.

The trabecular bone is more active, more subject to bone turnover, to remodeling. Common osteoporotic fractures sites, the wrist, the hip, and the spine, have a relatively high trabecular bone to cortical ratio. These areas rely on trabecular bone for strength. Therefore the osteoporosis may be considered as the trabecular bone loss, decrease of the density and the mechanical properties.

The aim of this work is to develop a procedure for generating specific finite element models of the human femur from a complete biomechanical analysis of the bone and of the trabecular tissue. This procedure includes:

- Design of the testing procedure and devices
- Sample preparation
- Experimental test of human femora
- Experimental test of trabecular specimens
- Generation of material models from the mechanical tests
- FE modeling and calculations
- Validation of the simulations with the experimental observations

Zusammenfassung

Die Implantation von Hüftendoprothesen hat sich als Standardtherapie der orthopädischen Chirurgie seit Jahren etabliert. In der Regel wird an der Hüfte eine Totalendoprothese (TEP) eingesetzt, die sowohl den Gelenkkopf als auch die Gelenkpfanne ersetzt.

Eine Gelenkschädigung an der Hüfte kann durch verschiedene Erkrankungen bedingt sein. Dazu gehören unter Anderem Arthrose (Gelenkverschleiß), Gelenkentzündungen wie Gelenk-Rheuma, sowie Tumore. Ebenfalls können Verletzungen am Gelenk, Knochenbrüche in der Nähe und Fehlstellungen die häufigsten Indikationen für ein künstliches Gelenk sein.

Ziel beim künstlichen Gelenkersatz ist eine dauerhafte Fixation und schmerzfreie Funktion der Prothesenkomponenten im Knochen und die Minimierung des Abriebs zwischen den Gleitpartnern Pfanne und Kopf.

Als häufigste Komplikation der Hüftendoprothese gilt die aseptische Lockerung, welche die Standzeit der Endoprothesen minimiert. Die durch die unphysiologische Krafteinleitung bedingten Adaptationsvorgänge (sogenanntes “stress shielding“) gelten als eine wesentliche Ursache für die aseptische Implantatlockerung in Verbindung mit einem Verlust der tragenden Knochensubstanz (Wirtz und Niethard, 1997).

Um diesen chirurgischen Eingriff sowie die entsprechenden Endoprothesen optimieren zu können, werden genaue Rechenmodelle des Knochens benötigt, die zusätzlich eine große Menge an Information aus dem biomechanischen Bereich erfordern.

Die Stabilität der Knochen hängt von Materialeigenschaften und Geometrie ab. Einer der wichtigsten Parameter der Materialeigenschaften ist der Elastizitätsmodul E. Dieser Materialkennwert beschreibt den Zusammenhang zwischen Spannung und Dehnung bei der Verformung eines festen Körpers bei linear-elastischem Verhalten.

Es gibt zwei Arten von Knochengewebe hinsichtlich ihrer Dichte und Porosität: kortikale (oder Substantia compacta) und trabekuläre Knochen (Substantia spongiosa). Kortikalis hat eine Porosität im Bereich zwischen 5% und 10% und befindet sich in der Regel entlang der äußeren Schaftabschnitte der Röhrenknochen. Kortikalis bildet die äußere Hülle um den trabekulären Knochen in den Gelenken und im Wirbelkörper (Martin, 1998). Spongiosa hat eine Porosität im Bereich von 75% bis 90%. Es wird normalerweise in platten Knochen (wie das Becken), am Ende der langen Knochen (z.B. dem Oberschenkel) und in den Wirbel gefunden. Kortikaler Knochen macht etwa 80% der gesamten Skelettmasse aus, während trabekulärer Knochen zu etwa 70% zum Skelettvolumen beträgt.

Die Spongiosa ist biologisch aktiver und wird durch Knochenumbau höher beeinflusst. Typische osteoporotische Frakturen betreffen das Handgelenk, die Hüfte und die Wirbelsäule und besitzen ein relativ hohes Spongiosa-Kortikalis Verhältnis. Genau diese Bereiche verlassen sich auf die Festigkeit des trabekulären Knochens. Deshalb kann die

Osteoporose als trabekulärer Knochenverlust, Verringerung der Knochendichte und der mechanischen Eigenschaften betrachtet werden.

Ziel dieser Arbeit ist es, ein Verfahren zur Erzeugung von spezifischen Finite-Elemente-Modellen des menschlichen Femurs, ausgehend von einer vollständigen biomechanischen Analyse des Knochens und der Spongiosa, zu entwickeln. Dieses Verfahren beinhaltet:

- Auslegung des Testverfahrens und der Geräte
- Probenvorbereitung
- Experimentelle Versuche der menschlichen Femora
- Experimentelle Versuche der trabekulären Proben
- Generierung von Materialeigenschafts-Modellen aus den mechanischen Prüfungen
- Entwicklung mechanischer FE-Modelle und Analyse
- Validierung der Simulationen mittels der experimentellen Beobachtungen

Contents

1 Introduction

The bone is a complex organ and like other organs is living. In the same way, bone is highly vascularized and the circulation of blood through bone is necessary for maintenance of bone vitality, bone growth, bone resorption and repair of fracture and other injuries. A remarkable fact about bone is that it adapts itself to external actions and loads involved in daily activities. Those mechanical stresses modulate the change, growth, and resorption of bone. An understressed bone can become weaker, but an overstressed bone can also become weaker. There is a proper range of stresses that is optimal for the bone (Fung, 1993).

Every year in Germany about 200.000 total hip replacements (THR) are carried out (BQS-Qualitätsreport, 2006). Furthermore, around 20.000 hip prostheses per year have to be changed due to some problems.

After a total hip replacement, the natural stress distribution in the femur is significantly altered. When the implant is introduced, it will carry a portion of the load, causing a reduction of the stress in some regions of the remaining bone. This phenomenon is commonly known as stress shielding. In response to the changed mechanical environment the shielded bone will remodel according to Wolff's law, resulting in a loss of bone mass through the resorption. Resorption can, in turn, cause or contribute to loosening of the prosthesis (Joshi, et al., 2000).

The aseptic loosening, caused mainly by stress shielding, represents by 75.4% the principal reason for THR revisions (Malchau, et al., 2002).

The proximal femur has a high trabecular to cortical bone ratio. In this area the trabecular bone supports a large portion of the loads applied to the bone. Therefore one method to alleviate this problem consists in reducing the stress shielding. The stress distribution of the bone with the prosthesis should match up with the natural stress distribution of the healthy bone.

Because of the complex nature of this mechanical problem, the most widely used analytical approach has been the finite element method (FEM). The modeling using FEM

requires input data, namely: geometry, material properties, boundary and load conditions. The simulations of the models can provide outputs: strains, stresses and local displacements.

1.1 Motivation

Given the amount of THR revisions, due mainly to aseptic loosening, the prediction and prevention should be the primary goal in order to reduce the stress shielding and thus the associated problems. This requires accurate diagnoses of the bone mechanical response. Patient specific data according to the individual mechanical properties of the involved bone are not considered so far in clinical routine. In the majority of clinical centers worldwide the preoperative planning for the selection of an implant, e.g. the endoprostheses for THR, is performed on an x-ray of the patient´s hip joint. Therefore in preparation for the surgical intervention the surgeon is only able to select on a 2D X-ray the approximately best fitting size of an endoprosthesis using simple, transparent template sheets with the outlines of the implants. The drawbacks and limitation of such a two-dimensional approach are obvious especially because rotational misalignment is not controlled and the position of the prosthesis is only revisable in the coronar plane. To overcome these problems new approaches were pursuit in the last years to use 3D information from patient specific computer tomography (CT) data (Handels, et al., 2001; Viceconti, et al., 2004). With these virtual 3D planning systems the surgeon - for the first time - can visualize the position of the implant components in three dimensions or may plan a custom-made implant for a specific bony contour. Still, these systems provide only geometric data and leave the decision about the best implant design or size according to the surgeon's subjective medical experience. However, most important is the additional knowledge of the patient specific biomechanical properties of the affected bone to select the optimal implant design, size and position according to the prediction of individual load transfer from implant to bone. This information is still missing in the available 3D planning systems. However, quantitative computed tomography (QCT) enables reconstruction of the threedimensional bone mineral density (BMD) distribution, which could be related to experimental data on bone stiffness and strength in vitro (Rho, et al., 1995; Keyak, et al., 1994; Kaneko, et al., 2003).

In the past two decades, three-dimensional finite element (FE) analyses in conjunction with QCT technique were carried out for predicting bone's mechanical behavior (Keyak, et al., 1990; Viceconti, et al., 1998; Yosibash, et al., 2007). At the macro level the bone presents elastic linear response for loads in the normal range of regular daily activities (Keaveny, et al., 1994). This fact represents a significant advantage for the application of the finite element theory. As previously mentioned, the bone's geometrical representation as well as the BMD distribution may be obtained from QCT scans and these data could be employed to build a FE analysis.

Biomechanical experiments can provide the necessary data in order to generate accurate FE models of the bone. The material properties of the bone can be obtained from

tests of bone specimens and introduced into the models. Then, the results of the simulations can be compared with the experimental observations from tests of the bones, both sharing the same boundary and load conditions.

Therefore, the current study proposes a procedure for specific-modeling the human femur from in-vitro experiments of the bone and of the trabecular tissue in order to predict the elastic mechanical behavior of patient-specific femora.

1.2 Background

As observed by Wolff (1892), the inner architecture of bone adapts to external influences. Instrumental in particular for the development of Wolff's theories was the work of the anatomist Meyer and the engineer Culmann (Huiskes, 2000). They discovered a remarkable similarity between the trabecular architecture of the proximal femur and the patterns of the stress trajectories, calculated with the new theory of "Graphical Statics", developed by Culmann.

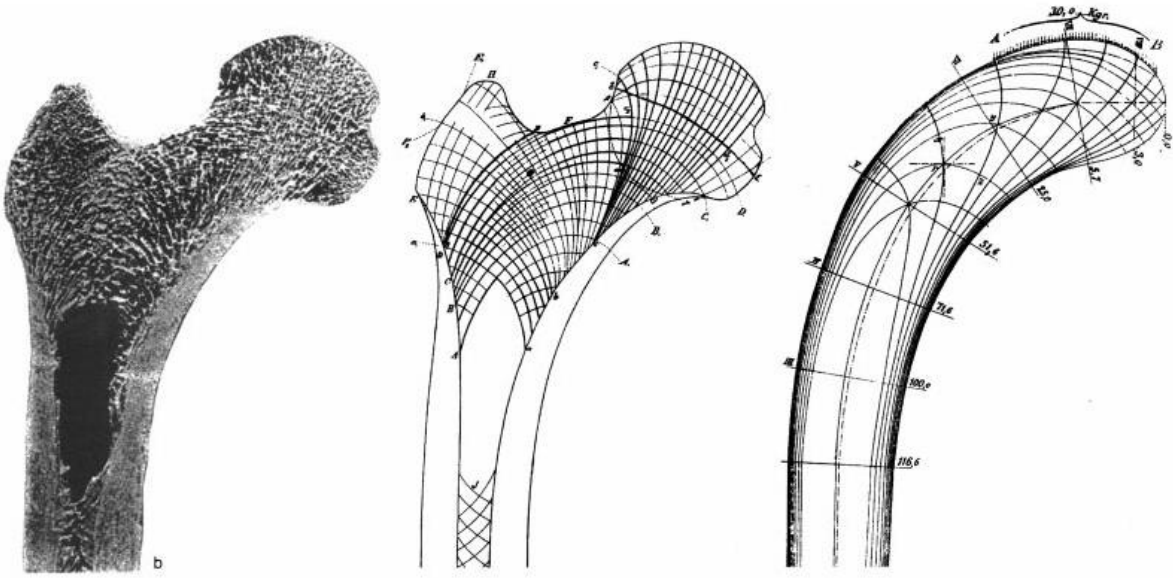

Fig. 1-1. The basis of Wolff's trajectorial theory. On the left a midfrontal section of the proximal femur showing trabecular architecture; in the middle the schematic representation drawn by Meyer (1867); and on the right the stress trajectories in a model analysed by Culmann, using graphical statics. Stress trajectories are curves representing the orientations of the maximal and minimal principal stresses in the material under load. The maximal and minimal stress trajectories always intersect perpendicularly. (Huiskes, 2000)

Bone is a viscoelastic material. Though, accordingly to Linde et al. (1991), the mechanical properties hardly depend on the strain rate in the range of 10^{-3}-10^{-2} s^{-1}, where most experiments were performed. Hence in the following, bone will be treated as an elastic material.

Additionally, the bone tissue presents a mechanical and structural anisotropy, whose degree highly varies between the different bones and within the inner structure of each of them.

One of the major parameters in the material science is the Young's modulus or elastic modulus. This parameter describes the behavior of material under load (Ugural, et al., 2003).

In the one-dimensional case of a bar under axial load, the mechanical properties of an elastic material are described in the linear range by the law of Hooke:

$$\sigma = E \cdot \epsilon \tag{1-1}$$

whereas,

$\sigma = F/A$: is the stress, with F the total axial force and A the cross-sectional area, where the force is applied

E: the Young's modulus.

$\epsilon = \Delta L/L_0$: the Cauchy strain or engineering strain valid for small strains, with L_0 the original length and ΔL the change of length. Or,

$\varepsilon = \int_{L_0}^{l} \frac{\delta l}{l} = \ln\left({}^{l}/_{L_0}\right)$: the logarithmic strain or true strain, with l the final length.

In a more general way the Hooke's Law may be expressed in the anisotropic form and matrix notation, also called Voigt notation. A material without any plane of symmetry is considered fully anisotropic and requires 21 elastic constants.

$$\begin{bmatrix}\sigma_{xx}\\ \sigma_{yy}\\ \sigma_{zz}\\ \sigma_{yz}\\ \sigma_{zx}\\ \sigma_{xy}\end{bmatrix} = \begin{bmatrix}C_{11} & C_{12} & C_{13} & C_{14} & C_{15} & C_{16}\\ C_{21} & C_{22} & C_{23} & C_{24} & C_{25} & C_{26}\\ C_{31} & C_{32} & C_{33} & C_{34} & C_{35} & C_{36}\\ C_{41} & C_{42} & C_{43} & C_{44} & C_{45} & C_{46}\\ C_{51} & C_{52} & C_{53} & C_{54} & C_{55} & C_{56}\\ C_{61} & C_{62} & C_{63} & C_{64} & C_{65} & C_{66}\end{bmatrix}\begin{bmatrix}\varepsilon_{xx}\\ \varepsilon_{yy}\\ \varepsilon_{zz}\\ \varepsilon_{yz}\\ \varepsilon_{zx}\\ \varepsilon_{xy}\end{bmatrix} \tag{1-2}$$

In contrast, an orthotropic material has at least 2 orthogonal planes of symmetry, where material properties are independent of the direction within each plane. Such materials require 9 independent variables (i.e. elastic constants) in their constitutive matrices.

By convention, the 9 elastic constants in orthotropic constitutive equations are comprised of 3 elastic moduli E_x, E_y, E_z, the 3 Poisson's ratios ν_{xy}, ν_{yz}, ν_{zx} and the 3 shear moduli G_{xy}, G_{yz}, G_{zx},

The compliance matrix takes the form.

$$\begin{bmatrix}\varepsilon_{xx}\\ \varepsilon_{yy}\\ \varepsilon_{zz}\\ \varepsilon_{yz}\\ \varepsilon_{zx}\\ \varepsilon_{xy}\end{bmatrix}=\begin{bmatrix}\frac{1}{E_x} & -\frac{\nu_{yx}}{E_y} & -\frac{\nu_{zx}}{E_z} & 0 & 0 & 0\\ -\frac{\nu_{xy}}{E_x} & \frac{1}{E_y} & -\frac{\nu_{zy}}{E_z} & 0 & 0 & 0\\ -\frac{\nu_{xz}}{E_x} & -\frac{\nu_{yz}}{E_y} & \frac{1}{E_z} & 0 & 0 & 0\\ 0 & 0 & 0 & \frac{1}{2G_{yz}} & 0 & 0\\ 0 & 0 & 0 & 0 & \frac{1}{2G_{zx}} & 0\\ 0 & 0 & 0 & 0 & 0 & \frac{1}{2G_{xy}}\end{bmatrix}\begin{bmatrix}\sigma_{xx}\\ \sigma_{yy}\\ \sigma_{zz}\\ \sigma_{yz}\\ \sigma_{zx}\\ \sigma_{xy}\end{bmatrix} \quad 1\text{-}3$$

where,

$$\frac{\nu_{xy}}{E_x}=\frac{\nu_{yx}}{E_y};\ \frac{\nu_{zx}}{E_z}=\frac{\nu_{xz}}{E_x};\ \frac{\nu_{yz}}{E_y}=\frac{\nu_{zy}}{E_z}$$

The elasticity matrix may be found from the inverse of the above shown compliance matrix.

A special class of orthotropic materials is those that have the same properties in one plane (e.g. the y-z plane) and different properties in the direction normal to this plane (e.g. the x-axis). Such materials are called transverse isotropic, and they are described by 5 independent elastic constants, instead of 9 for fully orthotropic.

By convention, the 5 elastic constants in transverse isotropic constitutive equations are the elastic modulus and Poisson's ratio in the y-z symmetry plane, E_y and ν_y, the Young's modulus and Poisson's ratio in the x-direction, E_x and ν_{xy}, and the shear modulus in the x-direction G_{xy}.

The compliance matrix takes the form.

$$\begin{bmatrix}\varepsilon_{xx}\\ \varepsilon_{yy}\\ \varepsilon_{zz}\\ \varepsilon_{yz}\\ \varepsilon_{zx}\\ \varepsilon_{xy}\end{bmatrix}=\begin{bmatrix}\frac{1}{E_x} & -\frac{\nu_{yx}}{E_y} & -\frac{\nu_{yx}}{E_y} & 0 & 0 & 0\\ -\frac{\nu_{xy}}{E_x} & \frac{1}{E_y} & -\frac{\nu_y}{E_y} & 0 & 0 & 0\\ -\frac{\nu_{xz}}{E_x} & -\frac{\nu_y}{E_y} & \frac{1}{E_y} & 0 & 0 & 0\\ 0 & 0 & 0 & \frac{1+\nu_y}{E_y} & 0 & 0\\ 0 & 0 & 0 & 0 & \frac{1}{2G_{xy}} & 0\\ 0 & 0 & 0 & 0 & 0 & \frac{1}{2G_{xy}}\end{bmatrix}\begin{bmatrix}\sigma_{xx}\\ \sigma_{yy}\\ \sigma_{zz}\\ \sigma_{yz}\\ \sigma_{zx}\\ \sigma_{xy}\end{bmatrix} \quad 1\text{-}4$$

1.3 Anatomy of the Proximal Femur and Hip joint

The hip is a ball and socket joint formed by the articulation of the spherical head of the femur and the concave acetabulum of the pelvis. It forms the primary connection between the lower limbs and the skeleton of the upper body and its primary function is to support the weight of the body in both static and dynamic postures (Fig. 1-2). Both the femur and acetabulum are covered with a layer of cartilage to provide smooth articulation and to absorb load. The entire hip joint is surrounded by a fibrous, flexible capsule to permit large ranges of motion but to prevent the proximal femur from dislocation. Several ligaments connect the pelvis to femur to further stabilize the joint and capsule. Muscles and tendons provide actuation forces for extension/flexion, adduction/abduction and internal/external rotation (Fig. 1-3) (Anderson, 2007).

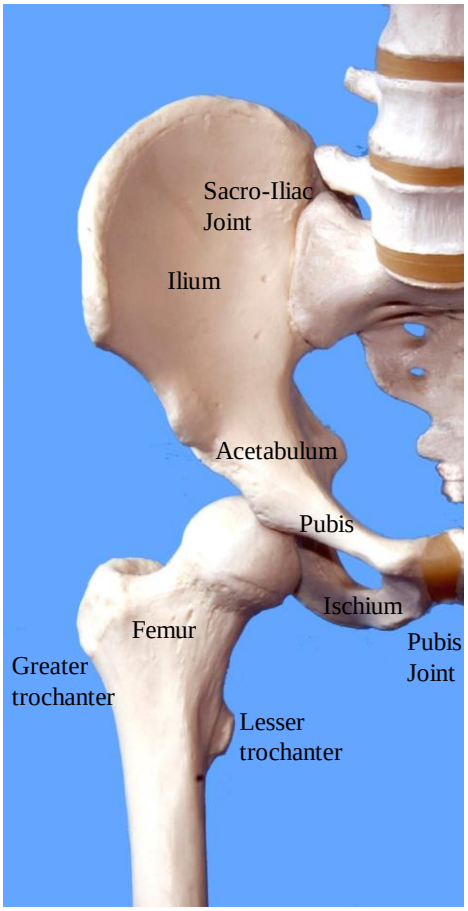

Fig. 1-2. Figure of a plastic hip showing the individual bones and joints.

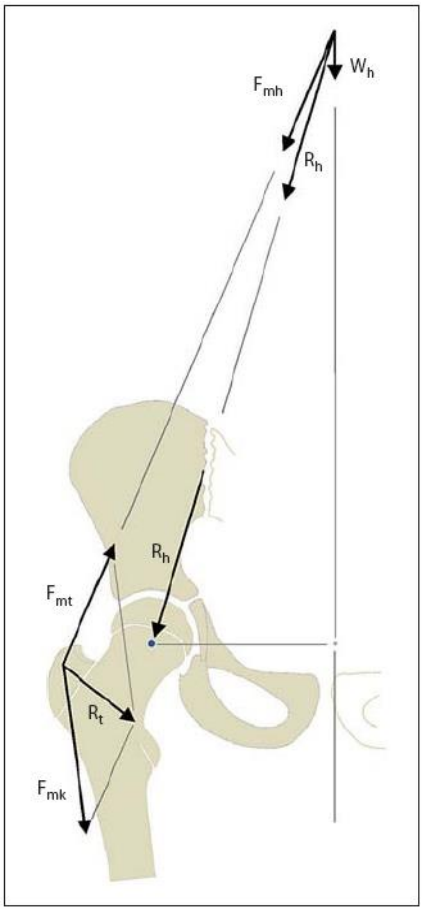

Fig. 1-3. Biomechanics model of the human hip joint (Heimkes, 2009).

The femur is the longest and strongest bone in the human body. It consists of a head and a neck proximally, a diaphysis (or shaft) and two condyles (medial and lateral) distally. The diaphysis of femur is a simplistic, cylindrical structure, while the proximal femur is irregular in shape, consisting of a spherical head, neck and lateral bony protrusions termed the greater and lesser trochanters. The trochanters serve as the site of major muscle attachment (Fig. 1-2). The lateral location of these structures offers a mechanical advantage to assist with abducting the hip (Gore, et al., 1977).

In 1993 Heimkes et al. set up the following model of the human hip joint biomechanics (Fig. 1-3). Regarding this model, the proximal femur is stressed by two resultant forces, R_h and R_t. The trochanteric resultant force R_t is the vectorial sum of the muscle resultant force F_{mt} exerted by all the abductor muscles and the force F_{mk}. The force F_{mk} is composed of the traction on the iliotibial tract and the force exerted by the knee extensors, which are connected by the vastus lateralis muscle to the greater trochanter apophysis (Skuban, et al., 2009).

1.4 Structure of the bone

Bone is an anisotropic, heterogeneous and viscoelastic material. It provides support for the body against gravity, serves as a lever system for the muscles, and protects internal organs. Chemically it is composed of collagen, water, hydroxyapatite mineral $Ca_{10}(PO_4)_6(OH)_2$ and several kinds of proteins.

Depending on shape, bone can be divided into three groups: long, short, and flat. In the leg and foot, only long and short bones are present.

In principle there are two types of bone, as determined by porosity: cortical (compact) bone and trabecular (cancellous, spongy) bone, both are present in the proximal femur.

1.4.1 Cortical bone

The hard outer layer of bones is composed of cortical bone tissue. This tissue gives bones their smooth, white, and solid appearance, and accounts for 80% of the total bone mass of an adult skeleton (Hall, 2007). Its porosity varies from 5% to 10% and its pores consist of space categorized as follows:

- Harvesian canals are approximately aligned to the long axis of the bone. They are about 50 µm in diameter and contain nerves and capillaries.
- Volkmann´s cannals are short and transverse canals connecting Harvesian canals to each other and to their outside surfaces of the bone.
- Others

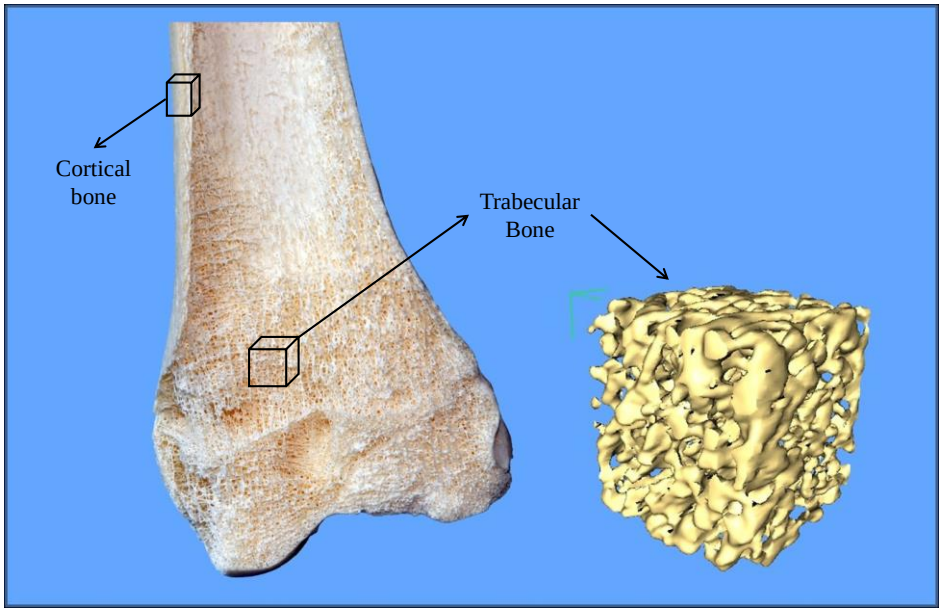

Fig. 1-4. Structure of the human femur.

1.4.2 Trabecular bone

Filling the interior of the bone is the trabecular bone tissue, an open cell porous network also called cancellous or spongy bone, which is composed of a network of rod- and plate-like elements that make the overall organ lighter and allowing room for blood vessels and marrow. Trabecular bone accounts for the remaining 20% of total bone mass and its porosity varies from 75% to 95% (Hall, 2007).

Trabecular bone can be described in terms of structural and material properties. Structural properties are extrinsic properties of both the trabeculae and the cavities and are important for the global stress analysis at the macroscopic level. Material properties are defined as intrinsic properties of the trabecular struts only.

1.5 Aim of the project

The aim of this project is to develop an experimental and numerical procedure to generate accurate specific FE models of the human femur, which describe its elastic mechanical behavior. This includes:

- Design of the testing procedure and devices
- Sample preparation
- Experimental test of human femora
- Experimental test of trabecular specimens
- Generation of material models from the mechanical tests
- FE modeling and calculations
- Validation of the simulations with the experimental observations

Therefore, the bone was experimentally studied at two structural levels. At the macro level, the mechanical response was evaluated from mechanical testing of human femora. At the meso level, trabecular specimens were prepared from these bones and tested mechanically enabling the determination of the elastic properties and thus the generation of material models based on the density. Furthermore, two material models were considered, namely isotropic and orthotropic model.

1.6 Thesis outline

The content of this thesis comprises four studies written in the form of articles. The following chapter presents an exhaustive literature review concerning the mechanical testing of bone as well as the numerical methods to analyze and predict the mechanical response of them (Fig. 1-5).

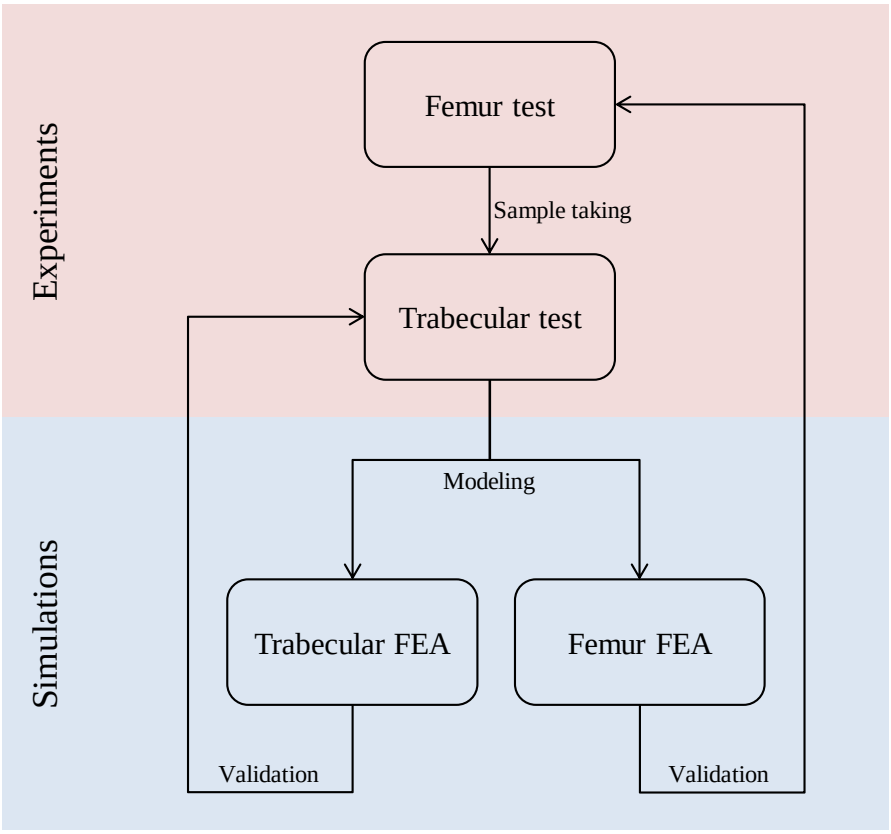

Fig. 1-5. Thesis flowchart.

The next two chapters present the experimental mechanical tests that were performed on fresh frozen human femora and on the cubical trabecular specimens, which were harvested therefrom. The mechanical response of the femora was recorded. In the same manner, the elastic properties of the trabecular specimens were evaluated and subsequently correlated with the bone mineral density.

The final two chapters consist of the FE model generation using the information from the mechanical tests. A modeling procedure was proposed to predict the mechanical behavior of the femora taken into account the inhomogeneous nature as well as the

orthotropic mechanical properties of bone. The scope of the continuum FE models was also evaluated at the meso level by means of the experimental data from the trabecular bone specimens and the numerical simulations of the specimens.

Finally, the thesis concludes with a summary of the results where the most remarkable aspects are discussed, and future perspectives are shown.

2 Literature Review

Much progress has been made in the last decades in the comprehension of the bone's mechanical properties. However, the complex nature and structure of bone makes it an almost uniquely difficult material to understand properly.

Most of the studies about bone can be classified regarding its scale, as follows:

- Studies of bone tissue at the meso/micro level. Usually, small specimens are harvested from different bones and locations and then mechanically tested in order to determine some specific mechanical properties.
- Studies of bone mechanical response at the macro level. In these cases, complete bones are subjected to complex mechanical experiments in order to assess the overall mechanical response of the bone. Sometimes, the results of these experiments could be commonly used as validation of analytical models based on computer simulation.

Firstly, the different experimental methods to obtain the mechanical properties of the trabecular bone are summarized and a large survey of published mechanical properties of human trabecular and cortical bone is presented. Afterward, several experimental procedures for testing complete bones are included as well.

2.1 Bone tissue testing methods

The common procedure to study the mechanical properties of bone at the tissue level consists in taking small and regular specimens and subsequently performing some tests. Depending on the mechanical parameter to be evaluated, the specimens may be tested mechanically by compression or tension or by means of acoustic techniques.

In some studies the specimens were tested intact with any previous treatment (Keller, 1994; Keaveny, et al., 1997) and in other ones the marrow and fat were removed and next the samples were rehydrated before the mechanical test (Keyak, et al., 1994; Majumdar, et al., 1998).

The most widely used method for evaluating of the mechanical properties of trabecular bone is the platens compression test, in which a cubic or cylindrical and unconfined or confined specimen is compressed. The inaccuracy of this method for unconfined specimens, due mainly to the "end artifact", is nowadays well established (Linde, et al., 1989; Rohl, et al., 1991; Linde, et al., 1992; Keaveny, et al., 1993; Keaveny, et al., 1994; Keaveny, et al., 1997) and the use of endcap technique and an extensometer is recommended. The term "end-artifacts" refers to the experimental inaccuracies and errors related to the specimen-platens interface. It is believed to be caused by a combination of: damage in the bone specimen caused during specimen machining (which causes underestimation of the elastic modulus), friction between the specimen and the platens with, in conjunction with unknown Poisson's ratio may caused an overestimation of the elastic modulus (Keaveny, et al., 1993). In addition, irregularities of the specimen geometry may lead to an incomplete contact between the compression platens and specimen, so underestimating the effective stress applied on the specimen.

The end-cap technique consists in fixing with glue or embedding in resin the ends of the specimens within two metal end caps. Thus the strain is measured by an extensometer across the central part of the specimen (Keaveny, et al., 1997; Kaneko, et al., 2004; Öhman, et al., 2007).

On the one hand, this procedure allows minimizing the effects of the end-artifacts and provides accurate values of modulus. On the other hand, the endcaps technique restricts the compression tests to only one spatial direction. The use of an extensometer, attached directly to the surface of the specimen, may present some problems as well. First, the extensometer measures the relative displacement between its knife edges which are attached to the surface of the specimen. The contact between the specimen and the compression platens, and consequently the load distribution on the cross section of the specimen might considerably influence the measurements of the extensometer. Additionally, the fixation knife edges of the extensometer may damage the trabecular structure of the specimen surface (Keaveny. et al.. 1997). The dimensions and gage length of the extensometer may limit the use of small specimens as well.

Since the endcaps technique prevents from testing the specimens in more than one direction, it is not appropriate to assess the orthotropic mechanical behavior of the trabecular bone.

In this case, cubical unconfined specimens are generally tested in three orthogonal directions and the strain is measured either from the displacement of the compression platens (Keyak. et al.. 1994; Goulet. et al.. 1994; Augat. et al.. 1998) or from the surfaces of the specimens by means of extensometers or optical devices (Odgaard. et al.. 1991; Kaneko. et al.. 2004).

The mechanical properties of the bone have been also measured using ultrasonic techniques. It bases on the ultrasonic wave propagation and how it may characterize the structure and elastic properties of the propagation medium (Sasso, et al., 2008). The ultrasonic technique is said to offer some advantages over mechanical testing, for example, the specimens can be smaller and it can also measure several anisotropic properties from

one specimen (Rho, et al., 1995). However, there have been significant discrepancies when comparing the results of the ultrasonic technique with those of the mechanical techniques (Grimal, et al., 2009).

2.1.1 Densitometry

A challenging and controversial aspect in the study of the bone and its mechanical properties has been the different measures of the density. This parameter, in its different forms, has been commonly correlated with the corresponding mechanical properties (e.g. strength, elastic modulus, shear modulus, etc.). Likewise, the different density measures have been occasionally compared themselves. However, there is frequently a lack of consistency regarding this parameter and the correlations from different sources might not be comparable due to mismatching density measures.

The most recurring densitometry measures from the literature are described in the following lines.

Wet or bulk density includes the mass of the marrow, essentially fluids, which contribute to the overall mass but not to the load carrying capability of the structure. In some cases, the bone marrow is removed from the specimens as well as the fat using chemical procedures and later rehydrated. The latter may be found referred to as apparent density or apparent wet density (Linde, et al., 1989; Keyak, et al., 1994).

Apparent dry density, dry density or directly apparent density by some authors (Ciarelli, et al., 1991; Keller, 1994), does not include this fluid contribution.

Ash density is obtained after bone specimens have been incinerated (Ciarelli, et al., 1991; Keyak, et al., 1994; Keller, 1994). This parameter usually presents a higher reproducibility than the other density measures and is strongly related to the bone mineral density (BMD) and the mineral concentration, respectively.

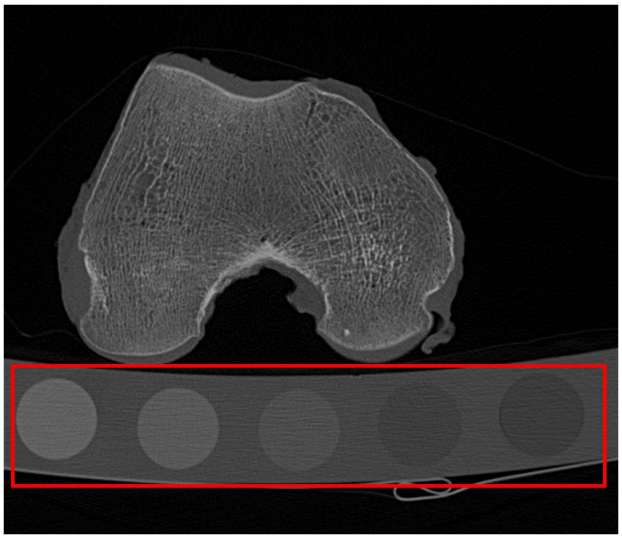

Fig. 2-1. Phantoms solutions for calibrated QCT density (BMD)

In other studies, quantitative computed tomography (QCT) has been used to provide an indirect measure of bone density. This technique is based on x-ray attenuation values, which are commonly referred to in Hounsfield units (HU). Hounsfield unit scale is a linear transformation of the original linear attenuation coefficient measurement in which the

radiodensity of distilled water at standard pressure and temperature (SPT) is defined as zero Hounsfield units, while the radiodensity of air at SPT is defined as -1000 HU. For a material X with linear attenuation coefficient μ_x, the corresponding HU value is therefore given by:

$$HU = \frac{\mu_x - \mu_{H_2O}}{\mu_{H_2O} - \mu_{air}} \times 1000 \qquad 2\text{-}1$$

where μ_{H2O} and μ_{air} are the linear attenuation coefficients of water and air, respectively, at SPT.

Therefore, QCT density for bone was frequently reported in raw form as CT numbers (HU). However, there might be differences of the measurements between scanners, making comparisons of CT numbers questionable. This problem was addressed by Cann and Genant, who developed a calibration phantom that contains several solutions of K_2HPO_3 in water (0, 50, 100, and 200 mg/cm^3), and was scanned simultaneously with the object under investigation (Keyak, et al., 1990).

The CT numbers for the phantom solutions are then used to calibrate the CT scan data for bone in terms of K_2HPO_3 concentration and the QCT data are reported in terms of mg/cm^3 K_2HPO_3 equivalent mineral density (also referred to as bone mineral density, BMD). A significant advantage of this approach is that the phantom is machine-independent, enabling calibrated QCT density data from different scanners to be compared (Keyak, et al., 1994).

Table 2-1. Correlation for young´s module and different densitometric measures

Correlation	**R^2**	**Reference**	**Remarks**
$E = 1.310(\rho_{wet})^{1.4}$	0.91	Lotz & Hayes 1990	Uniaxial mec. Test
$E = 0.5(QCT)^{1.2}$	0.90		
$\rho = 0.0012(QTC) + 0.17$	0.73		
$E = 10.5(\rho_{ash})^{2.29}$; femurs specimens	0.849	Keller 1994	Uniaxial mec. Test 8 mm cubes
$E = 10.2(\rho_{ash})^{2.01}$; femur specimens $\alpha > 0.5$	0.669		
$E = 10.5(\rho_{ash})^{2.57}$; spine and femur specimens	0.965		
$\rho_{ash} = 0.522\rho_{dry} + 0.007; \rho_{dry} < 1.0\ gcm^{-3}$	0.992		
$\rho_{ash} = 0.779\rho_{dry} - 0.250; \rho_{dry} \geq 1.0 gcm^{-3}$	0.968		
$E_{\mathrm{t-SI}}(\mathrm{CT}) = 269 + 4.86\ \mathrm{CT}$	0.80	Rho 1995	3-axis Ultrasonic test 10 m cubes
$E_{\mathrm{t-SI}} = 0.58(\rho_{wet})^{1.30}$	0.94		
$E_{t-ML} = 0.01(\rho_{wet})^{1.86}$	0.89		
$E_{t-AP} = 0.004(\rho_{wet})^{2.01}$	0.91		
$E_{\mathrm{c-SI}} = -6.087 + 0.010\rho_{\mathrm{wet}}$	0.61		
$E_{c-ML} = -4.007 + 0.009\rho_{\mathrm{wet}}$	0.47		
$E_{c-AP} = -6.142 + 0.014\rho_{\mathrm{wet}}$	0.77		
$\rho = 131 + 1.067\ CT$	0.84		
$E_{\mathrm{t-SI}} = 33900(\rho_{ash})^{2.20}$	0.916	Keyak 1994	3-axis Mec. Test 15 mm cubes
$E_{t-AP} = 1700(\rho_{ash})^{1.11}$	0.849		
$E_{t-ML} = 7330(\rho_{ash})^{2.07}$	0.916		
$\rho_{ash} = 0.000953\rho_{QCT} + 0.0457$	0.993		
$\rho_{QCT} = 0.529\ \mathrm{HU} - 1.30$	0.99		
$E_{\mathrm{trab}} = 33900(\rho_{ash})^{2.20};\ \rho_{ash} \leq 0.27$		Keyak 2003 (1998-2001)	Relations used for FEA (*) Relation for cortical bone was taken from (Keller, 1994)
$E_{cort} = 10200(\rho_{ash})^{2.01};\ \rho_{ash} \geq 0.6$ (*)			
$E_{trans} = 5307\ \rho_{ash} + 469;\ ;\ 0.27 < \rho_{ash} < 0.6$			
$\rho_{ash} = 1.22\rho_{QCT} + 0.0526$			
$E_{\mathrm{c-SI}} = 2065(\rho_{wet})^{3.09}$	-	Wirtz 2000	Statistical analysis from literature
$E_{c-AP.ML} = 2314(\rho_{wet})^{1.57}$	-		
$E_{\mathrm{t-SI}} = 1904(\rho_{wet})^{1.64}$	-		
$E_{t-AP.ML} = 1157(\rho_{wet})^{1.78}$	-		

Correlation	**R^2**	**Reference**	**Remarks**
$E_{\mathrm{t-SI}} = 0.161(\rho_{ash})^{1.61}$	0.775	Kaneko et al. 2004	3-axis Mec. Test 15 mm cubes Metastases cases
$E_{t-AP} = 0.00578(\rho_{ash})^{2.15}$	0.844		
$E_{t-ML} = 0.00155(\rho_{ash})^{2.30}$	0.741		
$\rho_{ash} = 0.839\rho_{QCT} + 69.8$	0.990		
$E_{\mathrm{optical}} = 0.00825(\rho_{ash})^{2.21}$	0.85	Odgaard & Linde 1991	Optical and mechanical (extensometer) measurements
$E_{\mathrm{extens}} = 0.0118(\rho_{ash})^{2.10}$	0.85		
$E = 8920(\rho_{app})^{1.83}$; All specimens	0.88	Morgan & Keaveny 2003	Endcaps and Extensometer. Unknown geometry.
$E = 6850(\rho_{app})^{1.49}$; Femoral head	0.85		
$E = -38.644 + 1.3665 \cdot \mathrm{HU}$; All specimens	0.791	Ciarelli et al. 1991	8 mm cubes unconfined
$\rho_{app} = 0.11837 + 0.001141 \cdot \mathrm{HU}$; All specimens	0.821		

Table 2-2. Experimental elastic modulus and testing methods for trabecular bone material.

Reference	**Elastic modulus [MPa]**	**Densitometry[1] [mg/cm³]**	**Location**	**Specimen configuration[2] [mm]**	**Technique**
(Linde, et al., 1989)	405 (113-853)	n.a.	Proximal Tibia	Ø7.5-L7.5	
	569 (195-1226)	n.a.	Proximal Tibia	Ø7.5-L7.5	End-Confined
(Rohl, et al., 1991)	485 ± 333	1049 ± 57 ρCT	Proximal Tibia	9 x 9 x 20	End-Confined
(Odgaard, et al., 1991)	689 ± 438	173 ± 53 ρ_{ash}	Proximal Tibia	7 x 6 x 6	Platens-extensometer
	871 ± 581				Optical
(Linde, et al., 1992)	320 ± 24	336 ± 17 ρ_{app}	Proximal Tibia	Ø6.5-L6.5	Platens-extensometer
	280 ± 25	342 ± 20 ρ_{app}		5.8 x 5.8 x 5.8	
(Linde, et al., 1993)	194 ± 32	n.a.	Proximal Tibia	Ø6.5-L6.5	Platens-extensometer
(Banse, et al., 1996)	1137 (72-3391)	n.a.	Proximal Femur	Ø6-L7.85	Indentation over a slice
(Keaveny, et al., 1997)	165 ± 110	n.a.	Lumbar Spine	Ø8-L16	End-confined Specimen-extensometer
	121 ± 97			Ø8-L?	Platens-extensometer
(Majumdar, et al., 1998)	(SI) 130.2 ± 116.9 (ML) 56.7 ± 69.7 (AP) 51.2 ± 47.5	166 ± 57.1 BMD	Proximal Femur	12 x 12 x 12	Platens-extensometer
	(SI) 118.8 ± 59.8 (ML) 42.2 ± 28 (AP) 59.6 ± 42.2	176.2 ± 54.1 BMD	Distal Femur		
(Augat, et al., 1998)	(SI) 137 ± 25 (AP) 54 ± 11 (ML) 68 ± 10	176 ± 11 BMD	Proximal Femur	12 x 12 x 12	Platens-extensometer
(Link, et al., 1998)	76.8	n.a.	Proximal Femur	12 x 12 x 12	Platens-extensometer
	45.7		Spine		

Reference	**Elastic modulus [MPa]**	**Densitometry[1] [mg/cm³]**	**Location**	**Specimen configuration[2] [mm]**	**Technique**
(Kaneko, et al., 2004)	(SI) 1090 ± 619 (222-3350) (AP) 701 ± 424 (77-1880) (ML) 448 ± 256 (37-1060)	214 ± 59.3 ρ_{ash} 172 ± 70 BMD	Distal Femur	15 x 15 x 15	Specimen-extensometer
(Burgers, et al., 2008)	376 ± 347	68.6 ± 28 BMD	Distal Femur	Ø8.1-L35	End-confined Extensometer
(Dendorfer, et al., 2008)	447 ± 117 1031 ± 461	n.a.	Spine Distal Femur	Ø11.2-L15	End-confined
(Nazarian, et al., 2008)	356.2 ± 89.7	n.a.	Spine and Femur	Ø5.53-L10.44	End-confined

[1] ρCT, is defined as an rescale CT density in Hounsfield units; ρ_{ash} is ash density; ρ_{app} is apparent density; BMD is the bone equivalent mineral density in terms of K_2HPO_3 concentration.

[2] Two specimen configurations are considered: cylindrical geometry, defined by the diameter (Ø) and the length (L), and rectangular parallelepiped defined by the three dimensions

Table 2-3. Experimental elastic modulus and testing methods for cortical bone material

	Elastic modulus (GPa)	**Densitometry (mg/cm³)**	**Location**	**Specimen configuration**	**Technique**
(Rho, et al., 1993)	18.6 ± 3.5	n.a.	Cortical-Tibia	0.3 x 0.3 x 2.2	Tensile testing
	20.7 ± 1.9		Cortical-Tibia		Ultrasound
	10.4 ± 3.5		Trabeculae-Tibia	Ø0.18-L2.3	Tensile testing
	14.8 ± 1.4		Trabeculae-Tibia		Ultrasound
(Turner, et al., 1999)	20.55 ± 0.21	n.a.	Cortical - Femur	10 x 10 x 10	Acoustic
	23.45 ± 0.21		Cortical - Femur		Nanoindentation
	17.50 ± 1.12		Trabeculae – Femur	10 x 10 x 10	Acoustic
	18.14 ± 1.7		Trabeculae – Femur		Nanoindentation
(Zysset, et al., 1999)	25.0 ± 4.3	n.a.	Cortical - Femur	N/A	Nanoindentation
	6.9 ± 4.3		Trabeculae – Femur		
(Hoffmeister, et al., 2000)	20.9 (E_{max})	n.a.	Cortical - Femur	Cubic	Ultrasound
	11.8 (E_{min})				
(Kaneko, et al., 2003)	19.8 ± 4.3	1157 ± 169 (416-1342) BMD	Cortical – Femur	6 x 6 x 2	Tensile and compressive testing
(Cuppone, et al., 2004)	18.6 ± 1.9	n.a.	Cortical – Femur	35 x 2 x 1	Three points bending test
(Dong, et al., 2004)	16.61 ± 1.83		Cortical - Femur		

2.2 Femur modeling and tests

In the 1970s and beginning of the 1980s, the photoelastic technique was commonly used to investigate the strain and stress fields of the femur under different loading situations (Jensen, 1978; Bianchi, et al., 1985).

By the time, this technique was progressively abandoned in favour of computer based methods as the finite element analysis (FEA), when computers became powerful. At the beginning, this method presented enormous limitations: number of material models, difficulties for digitalizing the bone geometry, etc. The computer-aided tomography constituted a real breakthrough allowing a great progress of the FEA technique. The computer tomography is a medical imaging method in which the specimen is scanned in virtual two-dimensional slices with an X-ray beam. Thereafter, an algorithm enables the density of the various parts of the specimen to be calculated, and the slices are then arranged in stacks to produce a three-dimensional density image of the object. The volume element or volumetric pixel of a CT is called voxel and its value is commonly reported in Hounsfield units (section 2.1.1). Therefore, each part of the scanned object, i.e. voxel, has both its density and 3-D position rendered objectively in numbers.

The FE models can be classified into two different groups, namely micro and continuum FE models. The latter notation was used in the present study to refer to FE models which do not include the micro structure of the bone and thus the models are treated as a continuum or none porous material, and not to be confused with the theory of continuum mechanics.

2.2.1 Micro-FE models

The models are generated based on micro CT (µCT) images of the specimens. This technique enables high resolution up to 5-10 µm for small trabecular bone specimens with dimensions of the order 5 to 10 mm (e.g. µCT 40, Scanco Medical AG, Brüttisellen, Switzerland) (Renders, et al., 2008; Charlebois, 2008). Also small complete bones such as distal radius or vertebrae can be scanned at high resolutions about 70-80 µm by means of peripheral computer. The trabeculae have a typical length of 1-2 mm and a diameter of 100-200 µm (Dagan, et al., 2004). In order to obtain the microstructure of the trabecular bone, it was recommended to use an image resolution less than one fourth trabeculae thickness (Chevalier, et al., 2007).

Thereafter, the µCT images have to be segmented by thresholding in order to distinguish between bone and fluids, e.g. marrow. This process has enormous influence on subsequent analysis as well as on different bone measures such as the bone volume fraction (Chevalier, et al., 2007).

The FE models generated from µCT images require an extremely refinement mesh with small element size and thus demand a huge computational effort. For example, the computation of the heads of two femora (Verhulp, et al., 2008) needed more than 3 weeks of many processors of a supercomputer. In other study (Eswaran, et al., 2007), the analysis

of large specimen consisting of vertebral bodies required 654 hours on a supercomputer having 144 parallel CPU and 300 Gb of memory. Furthermore, the scan time itself on a μCT scanner can be as much as 52 hours (Renders, et al., 2008).

Other relevant disadvantages of the μCT lie on the limited dimensions of the specimens to be studied on the one hand, and on the other hand, on the high X-ray doses, which might make it incompatible with in-vivo analysis of large bone specimens, e.g. the femur.

2.2.2 Macroscopic FE models

The quantitative computer tomography, used for clinical purposes, can provide a CT image resolution of 100-300 μm and the FE models based on QCT usually have an element dimension of at least ~1 mm. At this dimensional scale, the microstructure of the trabecular bone is homogenized so that the material property of each voxel corresponds to an average of the phases (bone, air, marrow) within it.

As with the micro FE model, the CT images have to be segmented previous to the FE analysis. In contrast to the first one, the segmentation only involved the outer boundary of the cortical bone and sometimes both types of bone (i.e. cortical and trabecular) are independently segmented.

At the beginning, the FE analysis consisted in homogeneous material and voxel-based hexahedral element models. Then, the bones voxel gray values were converted to bone density and correlated with the mechanical properties of the bone (Keyak, et al., 1990; Keyak, 2001). The use of hexahedral elements present some disadvantages such as an overestimation of stresses when large deformation occurs as well as an underestimation of the material properties at the boundary due to partial volume effect (Charlebois, 2008).

Thereafter, more accurate geometrical models were generated using tetrahedral elements (Taddei, et al., 2007; Bessho, et al., 2007). Some models based on the p-version FE were also proposed (Yosibash, et al., 2007; Trabelsi, et al., 2011). In this method, the convergence of the models was reached increasing the polynomial degree of the shape functions whereas the mesh is kept unchanged.

Most recently, some attempts were also carried out to describe the anisotropy of the complete femur. In some cases, the mechanical properties were correlated with different morphological parameters of the trabecular bone (Pahr, et al., 2009). Other studies were based on other experimental measures of the orthotropic mechanical response of bone (Peng, et al., 2006; Yang, et al., 2010).

The studies can be also classified into two groups: theoretical FE studies and experimental FE studies. The latter included the execution of mechanical in-vitro experiments of the specimens which were consequently modeled reproducing the same loads and constraints. In this way, the FE models can be compared and validated by means of these experiments (Taddei, et al., 2007; Bessho, et al., 2007; Yosibash, et al., 2007).

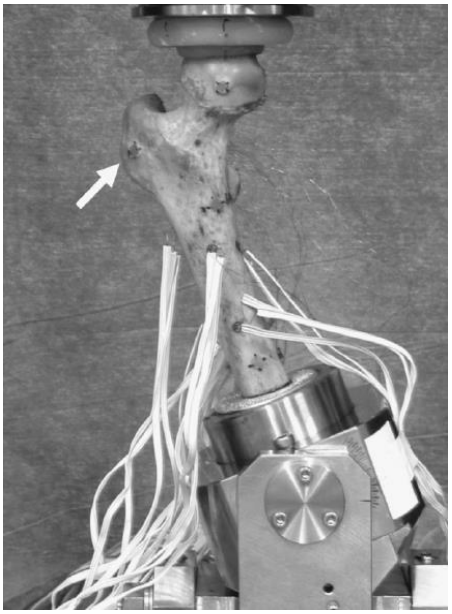

Fig. 2-2. Experimental setup (Bessho, et al., 2007).

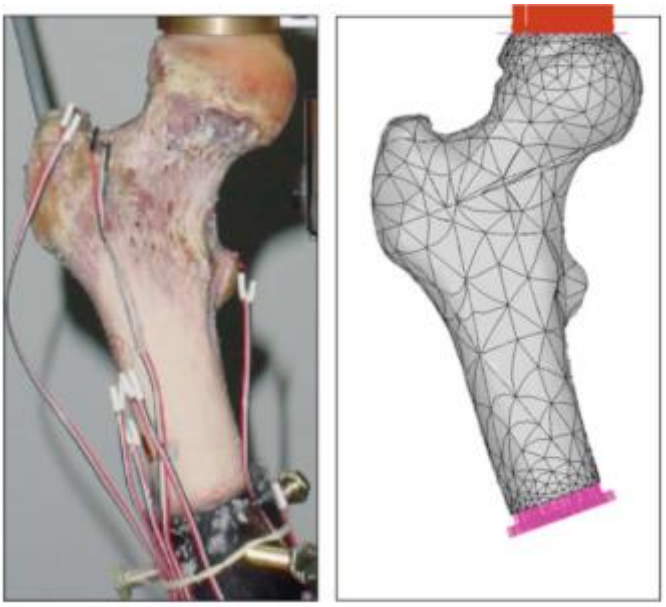

Fig. 2-3. Experimental setup and simulation (Yosibash, et al., 2007).

2.3 Conclusions for this project

Standard procedures to determine the mechanical properties of the trabecular bone as well as to describe the mechanical behavior of bone are well established.

However, there may be a missing link connecting both structural levels of the bone, namely the trabecular bone and the global behavior of bone. In the present study, the bone was studied from both points of view. From the analysis of trabecular specimens, some material relations were obtained and used to create bone-specific FE models. The latter were subsequently validated by in-vitro experiments, which were previously performed on the complete bones.

3 Compressive Tests of the Human Proximal Femur

3.1 Introduction

The first step for modeling the bone is to perform high resolution QCT scans. The use of CT data from the bone enables the generation of FE models based on the standard DICOM scan output (Keyak, 2001; Bessho, et al., 2007; Yosibash, et al., 2007). On the one hand, the specific geometry can be obtained by an analysis of the voxel coordinates. On the other hand, the elastic mechanical properties may be estimated according to the voxels intensity (given in Hounsfield units, HU, and corrected in terms of BMD in mg/cm³ of K_2HPO_3). The analysis of the CT data is presented in section 5.2.1.

The validation of FE models of the bone requires the comparison with a large amount of experimental observations on real bones. The mechanical behavior of the bone can be recorded using different measuring methods. In this section, these methods are presented.

3.2 Method

Fresh frozen femurs were prepared, scanned using a High Advanced Scanner (Philips) and tested on compression using a universal test machine Wolpert.

The experimental procedure included:

- Preparation of samples
- CT Scanning and definition of coordinate system and references
- Mechanical testing
  - Input: Force, constraints and position angles
  - Output: Strain and deformation (displacement)
- Data analysis

In order to validate the whole procedure a porcine bone were tested previously. The goal of this preliminary test was to identify possible issues in the procedure and to optimize the distribution of the tasks along the execution of the experiments.

3.2.1 Preparation of samples

First of all, the bones were examined looking for skeletal diseases by inspecting the general medical history of the donor. Later on, from the CT scan it would be ensured that no bony lesions were present.

Table 3-1. Donor and specimen data.

Specimen	Age (gender)	Height [m]	Weight [kg]
B3	69 (female)	1.65	67
B4	67 (male)	1.67	70
B5	62 (female)	1.62	72
B6	50 (male)	1.81	72.8
B7	59 (male)	1.75	67
B8	62 (female)	1.72	92

After defrosting, soft tissue as muscle, tendons and adipose tissue were removed from the bone using scalpel and other surgical instruments. The surface of the bones was preliminary degreased with ethanol. Then, the bones were QCT scanned using a High Advanced Scanner (Philips) for subsequent analysis, which are presented in Chapter 5.

Thereafter, the distal extremity of the femora was embedded using the bicomponent polyurethane resin Renncast FC53 (Huntsman Group) (Table 3-2). The shaft axis was vertically aligned and centered (Jensen, 1978; Yosibash, et al., 2007). The femur lied on its natural plane, defined by the condyles and the lesser trochanters (Fig. 3-1). A special tool was design to keep the bone on this plane and position during the embedding procedure. Then the femur was distally embedded up to 80 mm.

Table 3-2. Main physical properties of the casting resin Rencast© FC53.

Property	FC53
Demoulding time (min)	30-40
Density (g/cm³)	1.1
Viscosity at 25°C (mPa s)	80
Compressive strength (MPa)	41-44
Compressive Modulus (MPa)	1150-2400

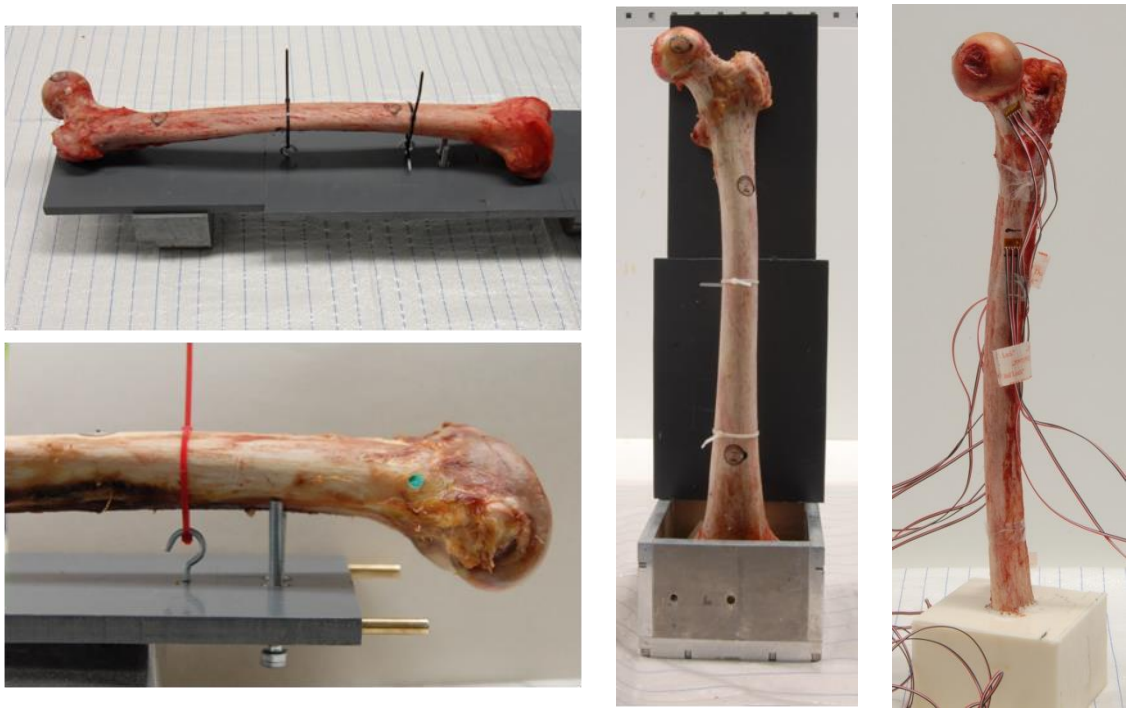

Fig. 3-1. Embedding procedure: a 11 cm central part of the diaphysis (femur's shaft) is fixed and centered. The presented tool allows keeping the correct position during the casting.

Some sites with minimal curvature were defined on which the strain gauges (SG) were to be fixed (Yosibash, et al., 2007). In order to attached the SGs, the bones in these sites were roughened with 400 grit sandpaper to removed any rest of soft tissue, periosteum or cartilage and then with 800 grit paper. Once again the bones at these specific sites were cleaned with ethanol and acetone. The SGs were bonded using M-Bond 200 (Vishay Measurements Group) following, for this purpose, the directions of the manufacturer. Thereafter, the strain gages were sealed with polyurethane coating (M-Coat A. Vishay Micro- Measurements).

In principle, five SGs were bonded to the surface of the bone: two on the superior and inferior parts of the femur neck, one under the greater trochanter, and two on the medial and lateral femur shaft (Fig. 3-2).

Fig. 3-2. Strain gage types: left a single strain gage and right a rectangular rosette gage.

Rectangular rosette gages (Vishay CEA-06-062UR-350/P2) were adopted for strain measurements. In some cases, single strain gages (Vishay CEA-06-062UW-350/P2) were used at reduced or irregular location or where the use of the larger rosette could be not recommendable (Fig. 3-2, Fig. 3-3). The employ of rectangular rosette gages allowed determining the principal directions (3.2.3). That could be considered a significant advantage especially in places with a high strain gradient, which are more sensitive to numerical errors due to possible mismatched orientation and position between experiments and simulations.

Additional points of interest were chosen for two different purposes. The first group of points (n = 4) was used as landmarks (Spee-D-Mark^{TM}, St. John Companies) for connecting the coordinate system of the CT scan, and subsequently of the FE Simulation with the coordinate system of the experimental setup. The second group of points was used to measure the global deformation of the bones under load. A 3D Digitizing system (Microscribe 3DX, Immersion Corporation, San Jose, California USA) were employed for such purposes and it is described in section 3.2.3. The points of the latter group were punched out helping to position the stylus tip of the Microscribe.

3.2.2 Scanning and referencing

CT scans of the bones were performed as it was previously mentioned. A specific procedure was defined to link the coordinate system of the Simulation based on the CT-data and the coordinate system of the real experiments based on the measurements of the Microscribe. This procedure allowed establishing the exact position of the bone regarding the load as well as the location and orientation of the strain gages and displacement points.

This procedure as well as the CT calibration will be explained in the Chapter 5.2.1.

3.2.3 Devices for measurements

The strain was measured at different locations using both single strain gages (Vishay CEA-06-062UW-350/P2, Vishay Precision Group, Malvern, USA) and 45° single-plane

rosette gages (Vishay CEA-06-062UR-350 P2, Vishay Precision Group, Malvern, USA) both with 1.57 mm active length and 350 Ω resistance.

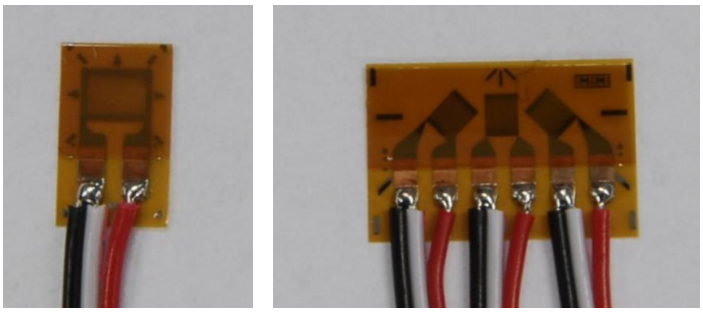

Fig. 3-3. Strain gages types used. Left: single strain gage (Vishay CEA-06-062UW-350/P2). Right: strain gage rosette 45° single-plane (Vishay CEA-06-062UR-350-P2).

The strain gages were connected to 4 channel amplifiers NI 9219 (National Instruments Corporation, Austin, Texas, USA) and to an 8-slot Data Acquisition chassis (NI CompactDAQ-9178). By means of a personal computer the strain gages signals were recorded by software (LabView SignalExpress, National Instruments Corporation, Austin, Texas, USA). Quarter bridge and 3-wire circuit was used for the measurements. The bridge was internally completed on the device.

Next, a short description of the strain gages measuring technique is presented.

Strain Gage Rosettes

Strain gage rosettes consist of two or more co-located strain gages oriented at a fixed angle with respect to each other. Strict co-location of the gages requires mounting each individual gage on top of the others in what is called a "stacked" rosette, but this leads to a complicated and often inaccurate type of gage. The more common approach is to place the gages in a tightly packed pattern as close as possible to the rosette center. Rosettes typically involve 2, 3 or 4 strain gages with relative orientations of 30°, 45°, 60° or 90° (Fig. 3-4).

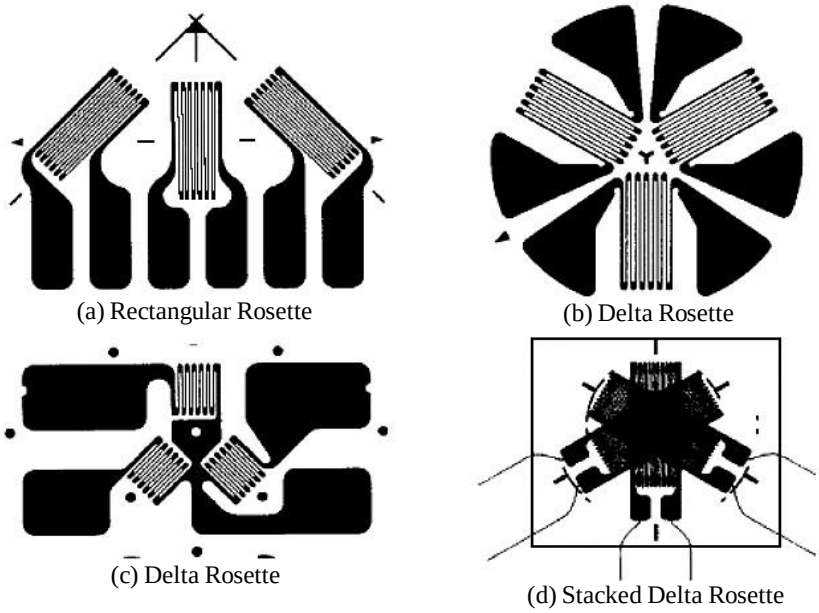

Fig. 3-4. Typical strain gage rosettes.

At least 3 independent strain readings are needed to define the 2D state of strain if no other information is available so the 3-gage rosettes are the most popular (the 90° 2-gage rosette can be used to measure principal strains when the principal direction is known and the gage can be oriented accordingly). The rectangular rosette and the delta rosette are the most commonly used 3-gage rosettes because of their simple geometry.

Rectangular Rosette Gage Equations

Given the measurement of 3 independent strains from the 3 gages in a rectangular rosette it is possible to calculate the principal strains and their orientation with respect to the rosette gage. It is also possible to calculate the state of strain at the gage location with respect to any particular XY axis system using either the rosette readings or the principal strains and their axis orientation. To illustrate this, it is considered a situation in which the rosette is oriented with gages labeled A, B and C at 45° apart as shown in Figure 3-5. It is also assumed that the principal strains at the rosette are oriented at an angle, φ, to the rosette gage A axis. For this case, it is easy to use the strain transformation equations (Eq. 3-1) to calculate the strain in each rosette gage in terms of the principal strains and the angle, φ, (assuming $\varepsilon_x = \varepsilon_1$ and $\varepsilon_y = \varepsilon_2$ and compute $\varepsilon_{x'}$ for angles of rotation φ, φ+45º, and φ+90º) to yield three equations:

$$\varepsilon_A = \frac{\varepsilon_1 + \varepsilon_2}{2} + \frac{\varepsilon_1 - \varepsilon_2}{2}\cos 2\phi \quad 3\text{-}1$$

$$\varepsilon_B = \frac{\varepsilon_1 + \varepsilon_2}{2} + \frac{\varepsilon_1 - \varepsilon_2}{2}\cos 2(\phi + 45°) \quad 3\text{-}2$$

$$\varepsilon_C = \frac{\varepsilon_1 + \varepsilon_2}{2} + \frac{\varepsilon_1 - \varepsilon_2}{2}\cos 2(\phi + 90°) \quad 3\text{-}3$$

These are 3 simultaneous equations relating ε_A, ε_B, ε_C to ε_1, ε_2 and φ. It is a relatively simple matter to invert the equations and solve for ε_1, ε_2, φ in terms of ε_A, ε_B, ε_C yielding:

$$\varepsilon_{1.2} = \frac{\varepsilon_A + \varepsilon_C}{2} \pm \frac{1}{\sqrt{2}}\sqrt{(\varepsilon_A - \varepsilon_B)^2 + (\varepsilon_B - \varepsilon_C)^2} \quad 3\text{-}4$$

$$\phi = \frac{1}{2}tan^{-1}\left(\frac{\varepsilon_A - 2\varepsilon_B + \varepsilon_C}{\varepsilon_A - \varepsilon_C}\right) \quad 3\text{-}5$$

Eq. 3-4 and Eq. 3-5 can be used to compute the principal strains and the principal axis orientation directly from the rectangular rosette gage readings. It has to be noted that there are many different possible gage numbering arrangements besides the particular ABC layout here, and they can lead to forms for the final results shown above but with A, B and C interchanged (Bauchau, et al., 2009; Sharpe, et al., 2008).

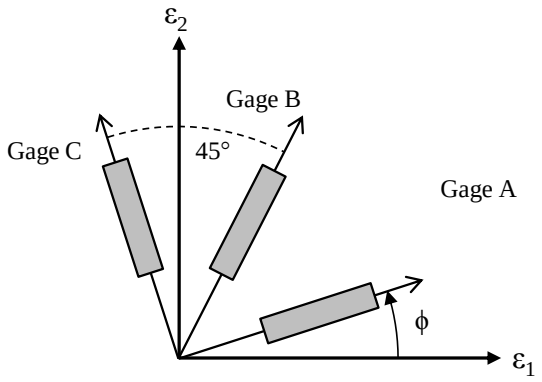

Fig. 3-5. Rectangular rosette gage orientation

The deformation of the bones was recorded from the displacement of the selected points between the unloaded and loaded states by means of the above mentioned 3D digitizing system Microscribe (Fig. 3-6). This device has the following technical specifications: position resolution 0.13mm, position accuracy 0.23 mm and reach of digitizing arm 127 mm.

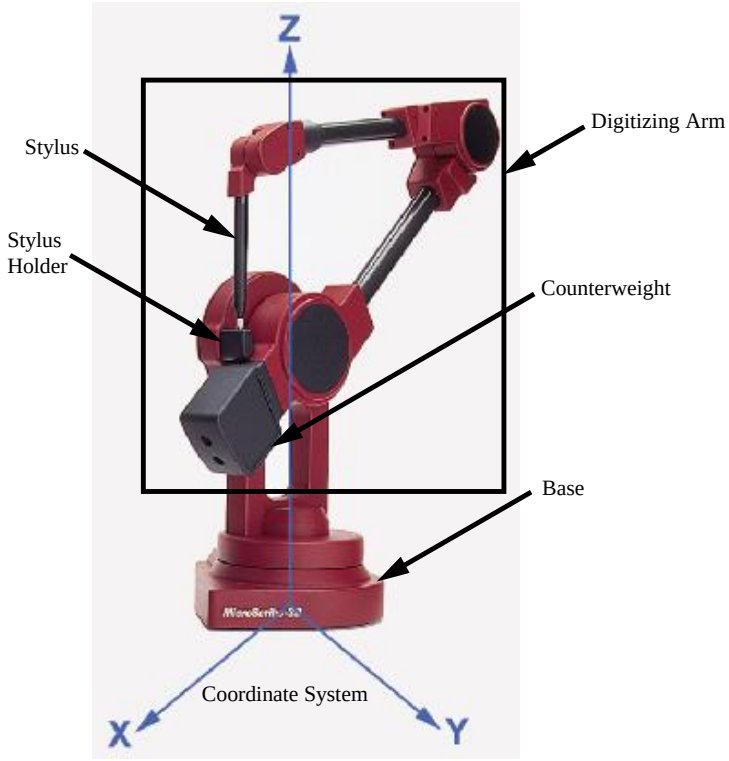

Fig. 3-6. Description of the 3D Digitizing system, Microscribe 3D.

The Microscribe was additionally employed to determine the relative position of the bone as well as the load, constraint and the strain gages position. This information would be taken into account in order to build the FE models.

3.2.4 Measurements procedure

Once the femurs have been properly potted and the strain gages bonded, the mechanical tests could be carried out.

The experiments consisted in a mechanical compression and considered three inclination angles (0°, 7°, 15°) and two load levels (500 N, 1000 N), which define six different load cases. A simple stance position configuration was simulated during the experiments. In this loading case, the force is applied in an inclination angle of 7° to the shaft axis (Jensen, 1978). Two additional inclinations (0° and 15°) (Keyak, et al., 1993; Yosibash, et al., 2007) were taken into consideration to obtain a comprehensive description of the anisotropic behavior of the bone.

By means of a servo-electric testing machine (Wolpert TZZ 707/386, Wolpert GmbH; Instron, Massachusetts, USA), a quasi-static compression test of the bones for each loading case was performed. The applied compression forces were smaller compared to bone's linear response regime (Yosibash, et al., 2007). The load was applied to the femoral head by means of a flat compression platen attached to a specifically made device, which allows the movement in the XY- plane and thus prevents the introduction of shear forces to the system (Fig. 3-7). This device consists of a set of ball bearings confined in a cage. In this way, the exact position and direction of the applied force stay constant along the execution of the experiments. The use of a ball and socket joint or of a cardan joint was ruled out because it would change the direction of the force in case of large displacements. This procedure simplifies the load definition for the FE modeling minimizing possible modelling errors and though represents mostly the mechanical physiology of the bone (Speirs, et al., 2007; Bessho, et al., 2007). In the same way, the use of the flat compression platen was preferred instead of a conical device because it allowed a more precise evaluation of the middle point of the applied load distribution (Yosibash, et al., 2007).

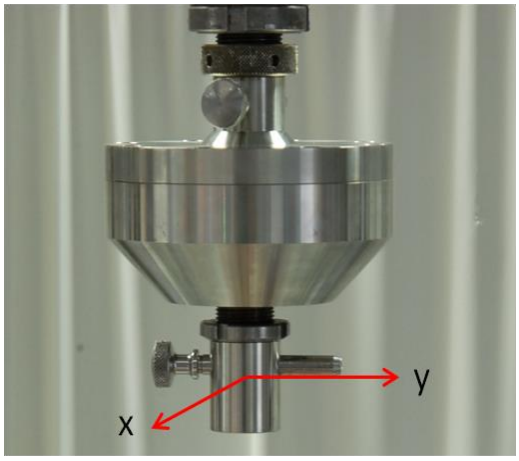

Fig. 3-7. XY-device. The compression plate is mounted within a double set of ball bearings enabling it to move in the transversal direction with a very low friction.

The measuring procedure consisted of the following steps. First, the bone was correctly placed and fixed to an adjustable angle plate at the corresponding angle (Fig. 3-8). The unloaded position of the bone, respectively the defined points used for this purpose, was measured using the Microscribe. Then the bone was loaded and, when the corresponding force was reached, the displacement was kept fixed. The loading was applied with a crosshead speed of 5 mm/min and alternatively performed with six compression cycles from 0 to 500 N and from 0 to 1000N. The position of the

displacement points was measured again in each loaded condition. Thereafter the position angle of the specimen was changed and tested in the same manner.

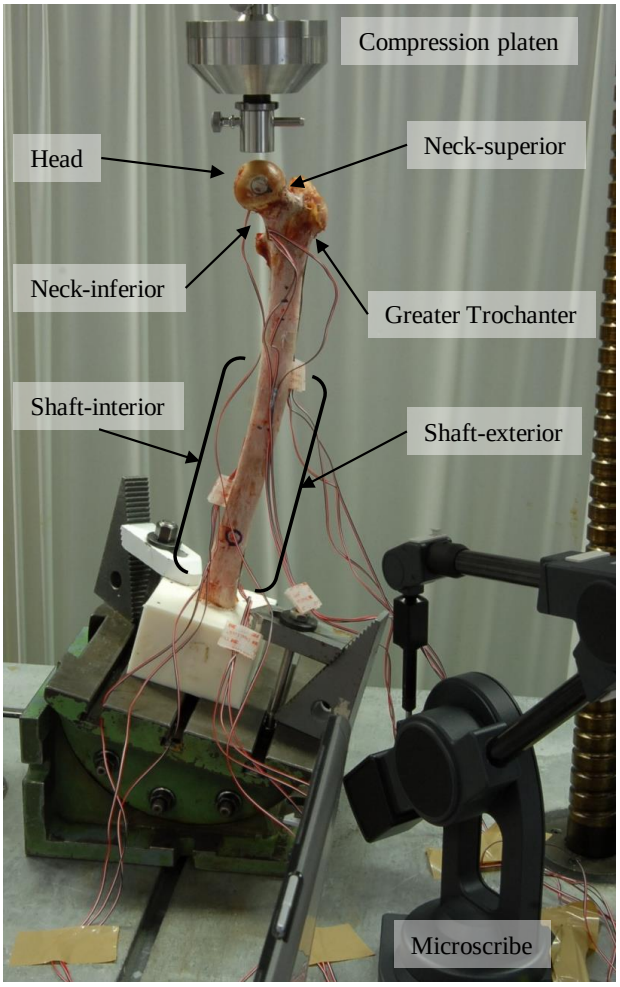

Fig. 3-8. Experimental setup. The bone was distally fixed on a tilting table and loaded on the head. Strain gages attached to some bone's locations recorded the strain. Overall deformation was measured by means of the Microscribe, which also enabled the acquisition of the bone position as well as the strain gages, load and constraints locations.

Meanwhile, the signals from the strain gages were recorded continuously during the compression test. For each of the three unloaded bone positions (0°, 7°, 15°) the coordinates of the following items were taken:

- CT landmarks
- Plane of the resin embedding block, defined by three points
- Strain gages, defined by three of the four vertexes
- Displacement landmarks

This information was required for referencing the experiments to the FE simulations.

3.3 Results

The linearity of the experimental data was analyzed by comparing the force-normalized strain and displacement values. High linear response was observed between the measurements for 500 N and 1000 N (Fig. 3-9).

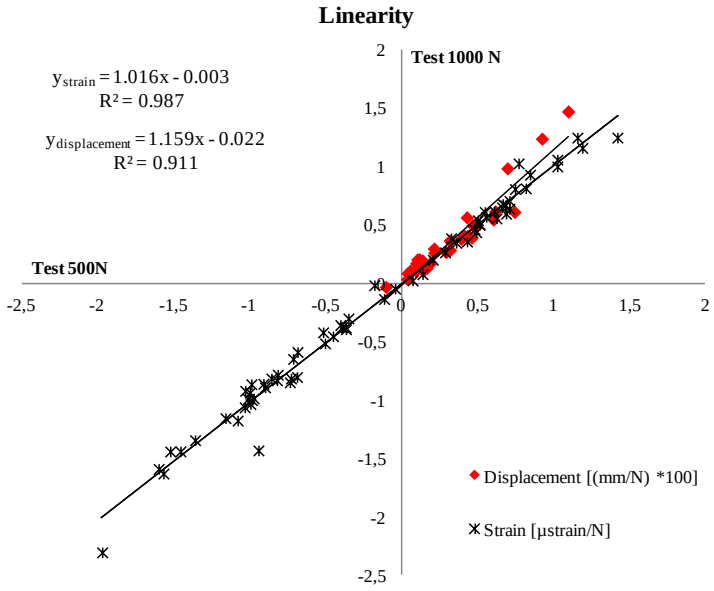

Fig. 3-9. Linearity of the experimental results. The strains and displacement has been normalized by the corresponding force.

The strain values presented a higher linearity ($R^2 > 0.98$) than the displacement values ($R^2 > 0.91$) (Fig. 3-9; Fig. 3-10). Two possible explanations for that difference are the manual measurement procedure for displacements as well as the accuracy of the displacement measuring device.

In the same way, a high repeatability of the strain measurements was observed for all the tests (Fig. 3-10). The signals from the strain gages presented also a good consistency all along the duration of the experiments, suggesting that the bone did not suffer any appreciable biological change.

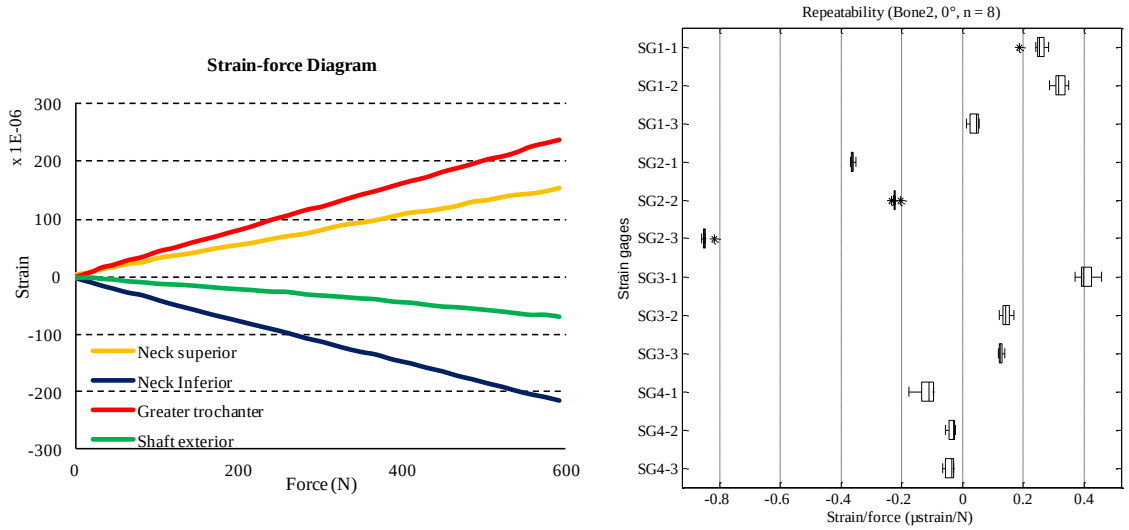

Fig. 3-10. Linearity of the strain/force (left) and repeatability of the strain measurements (right)

The experimental results were next plotted with respect to the bone angle position and to the different strain gages locations (Fig. 3-11). These locations could vary between

bones and might not be considered to represent exactly the same position on the bone geometry. On the one hand, the morphology of the bone could considerably differ between specimens. On the other hand, the requirements for fixing the strain gages conditioned the chosen measurement sites. However, this representation depicts an overview of the mechanical response of the bone and the influence of the bone position.

In this manner, it could be seem a mechanical pattern in the experimental observations. There were locations under tension, such as those of the superior neck, trochanter and the outer side of the femoral shaft (lateral). Compression was founded in the inferior neck and the inner side of the femoral shaft (medial). This response changed slightly for the 15 degree position of the bone, as it could be observed in the measurements of the strain gages located in the outer side of the bone shaft. In this case, the bones tended to bend to the lateral direction instead to the medial, so it happened for the 0 and 7 degree position, leading to compression in the outer face of the shaft.

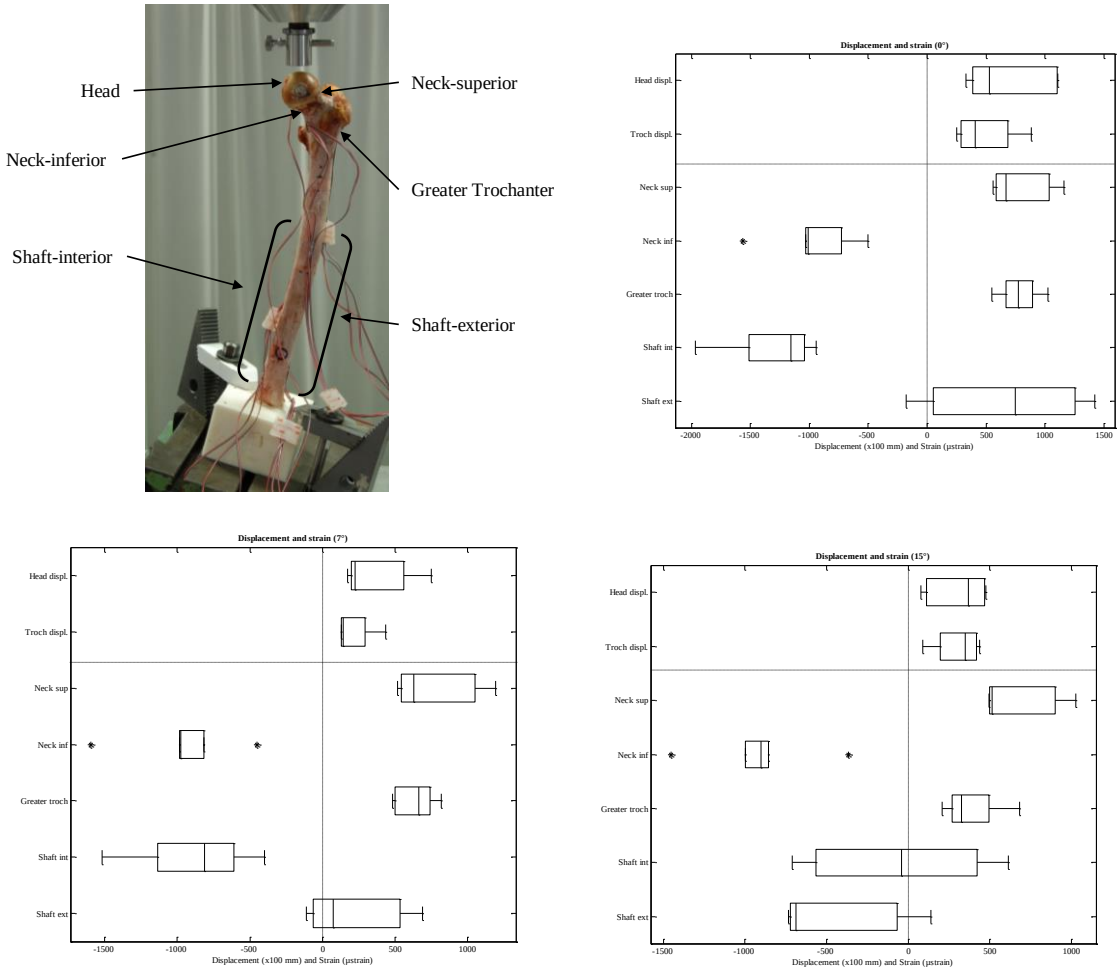

Fig. 3-11. Box plot of strain and deformation for the whole experimental dataset of bones (n = 6). The data is arranged by testing angle (0°, 7°, 15°) and within each group by the measurement location. The asterisks or stars represent outliers.

3.3.1 Estimation of errors

In the experimental procedure presented in this section, there can be some possible source of errors in evaluating the mechanical response of the human femur.

Besides the precision of the measurement devices, other aspects of the procedure can lead to errors. For instance, the technique of strain gages is well known to be prone to errors, as the cross-sensitivity, bonding faults, hysteresis, and temperature and humidity effects, among others. For perfect bonding, the manufacturer's recommendations were complied with. In general the adhesive layer must be continuous and as thin as possible. An excessive adhesive application could lead to an underestimation of the strain, and contrary, a lack of it could also distort the measurements of the strain gages.

To evaluate the dispersion of the measurement procedures, the coefficient of variation was defined as the ratio of the standard deviation σ to the absolute value of the mean μ, for a repeated measurement denoted by the subscript "i":

$$CV = \frac{1}{n}\sum_{i=1}^{n}\frac{\sigma_i}{|\mu_i|} \qquad 3\text{-}6$$

The measures from the strain gages presented a lower dispersion (CV = 5.3%) than the ones from the Microscribe (CV = 8.7%), which may explain the linearity differences between the measurements referred to above (Fig. 3-9).

3.4 Discussion

In this section a set of experimental procedures has been established in order to evaluate in a repeatable and reproducible way the mechanical response of human proximal femurs. The bones were loaded with two levels of force from the femur's head in several bone positions, which represented different anatomic situations, so capturing a wider range of the anisotropy of bone. This loading represented a simplification of the real physiology of the femur. As it was explained in section 1.3, the femur is subjected to multiple forces applied on the head, the lesser and greater trochanter. This situation can be immensely difficult to be reproduced by in-vitro experiments in a reproducible fashion. On the other hand, the experiments carried out in this section did not capture the bone response under extremely non physiological loading. These cases are commonly associated to accidental situations, as a fall on the side (Verhulp, et al., 2008). In this respect, it may be worthwhile for future studies that numerical models based on orthotropic properties were also evaluated with non physiological loading configurations.

The strain state of the bone was recorded by means of single strain gages and strain gage rosettes which were attached to the bone surface. Additionally, the overall deformation was assessed using a 3D digitizing system, enabling the coordinates of specific points to be measured on the unloaded and loaded bone. By means of the same device, a reliable procedure was developed to link the coordinate system of the experiments with that of the CT scans and, by extension, of the FE models.

4 Compression Tests of the Human Trabecular Bone Specimens

4.1 Introduction

From the point of view of continuum mechanics, the tensile and compression tests are fundamental material science tests in which a sample or specimen is subjected to uniaxial tension or compression. A transducer connected in series with the specimen provides an electronic reading of the load corresponding to the displacement or vice versa.

The proposed specimen geometry was cubical to allow the specimens to be tested in 3 orthogonal directions (Keyak, et al., 1994; Goulet, et al., 1994; Odgaard, et al., 1991; Kaneko, et al., 2004). The specimens were harvested following a specific protocol in order to standardize the sample-taking procedure.

Contrary to other materials, as composite materials, the trabecular bone does not present a significant difference between the tensile and compressive modulus (Keaveny, et al., 1994). Furthermore, it is as well demonstrated that the femur predominantly works under compression rather than tension (Rudman, et al., 2006).

Therefore, compressive testing method was established in this study in order to assess the elastic mechanical properties of the trabecular bone. For that purpose, two experimental techniques were taken into consideration.

First, the extensometer technique is a common method for compression testing of bone, in which an extensometer is attached to the center of the specimen, so recording the relative displacement between its knife edges caused by the deformation of the specimen. Therefore, the determination of the elastic modulus involves the strain measured from the extensometer and the whole cross section of the specimen for stress calculation.

A new experimental technique was developed in order to estimate the effective contact area between the trabecular specimen and the compression platens. The machining of trabecular specimens as well as the inhomogeneous nature of bone may lead to

inaccuracies by unconfined compressive testing, in form of a reduction of the effective contact area. This may cause an underestimation of the mechanical properties of the unconfined tested specimens and it may also contribute to the so called end artifacts. The effective contact area may subsequently be used to assess the mechanical properties of unconfined trabecular bone specimens in the orthogonal directions.

The contact interface or contact area may be evaluated using pressure sensitive film such as Fuji Film Prescale Pressure Measuring System (Fuji Photo Co. Ltd., Tokyo, Japan). Since 1980, when Fukubayashi and Kurosawa (1980) first used this method to measure contact area and contact pressure distribution in the knee, this system has become a standard technique in orthopedics and bioengineering research (Bachus, et al., 2006). The measuring of contact area between two metal plates was also introduced in several studies (Drewniak, et al., 2007; Xiong, et al., 2010).

The pressure film method bases the calculation of the elastic modulus on an "effective stressed geometry" of the specimen, which consisted in the total length of the specimen (in contrast to the gage length of the extensometer) and the effective contact area (in contrast to the whole cross section).

In the same way as it was done for the femora, the cubical specimens were scanned in a high resolution CT-scanner. The CT-scans incorporate the bone mineral distribution and a rough overview of the trabecular structure of the specimens.

The purpose of this section is thus the study of the mechanical properties of human trabecular bone from the proximal femur in order to obtain suitable material relations between the elastic modulus and the bone mineral density, which could be introduced into FE models.

4.2 Method

From three previously tested femora, cubical trabecular specimens were taken following a specific sample-taking procedure and tested mechanically. This experimental procedure included a series of different tasks:

- Preparation of samples
  - Construction of customized tools
- CT scanning
- Compressive testing. Two methods were considered:
  - Extensometer method
  - Pressure film method
- Data analysis

Once again, some preliminary and validation test were performed on porcine bone specimens. The purposes of these experiments were diverse: assess the most suitable storage method (Linde, et al., 1993), the sensitivity of the experiments to boundary conditions (e.g. moisture) and validation of the sample cutting procedure.

4.2.1 Preparation of samples

In biomechanical research with human or animal bones, a first and major challenging step is the definition of a consistent coordinate system. The difficulty of this step is caused by the high variability of the morphology of individual human bones as well as their complex geometry. The Cartesian coordinate system in this research was defined by an axis through the middle points of the femoral head and neck and a plane defined by the most posterior points, i.e. lesser trochanter and the lateral and medial condyles (Fig. 3-1).

The goal of this section was to establish a standard procedure in order to take cubical specimens from the proximal femurs in a defined anatomical direction. Thus, it was not sought to align the cutting planes with the main trabecular directions (MTD) of the specimen. In the proximal femur, the main trabecular direction changes relatively fast from one site to another, as it was shown in Figure 1-1. In consequence, this experimental consideration may limit the number of specimens to be harvested from the bone. Usually, the studies which consider the MTD took only one specimen per femur's head (Öhman, et al., 2007). Because of the fact that this study focused mainly on the bone mineral density distribution as well as on some morphological parameters, the consideration of the MTD was dismissed.

The cutting planes were defined by an axis, which goes through the center of the femur's head and neck (Fig. 4-1), and a plane, which contains the mentioned axis and represents one of the three cutting planes. The second one was described normal to the middle axis and finally the third one was defined orthogonal to the other two.

Previous to the mechanical testing, the middle axis of the femur's head and neck was geometrically defined using a tool which was specifically designed and built for that purpose (Fig. 4-1, Fig. 4-2). It consists of a conical part to center the femur's head and two connected sliding blades with a "V-profile" in order to center the femur's neck.

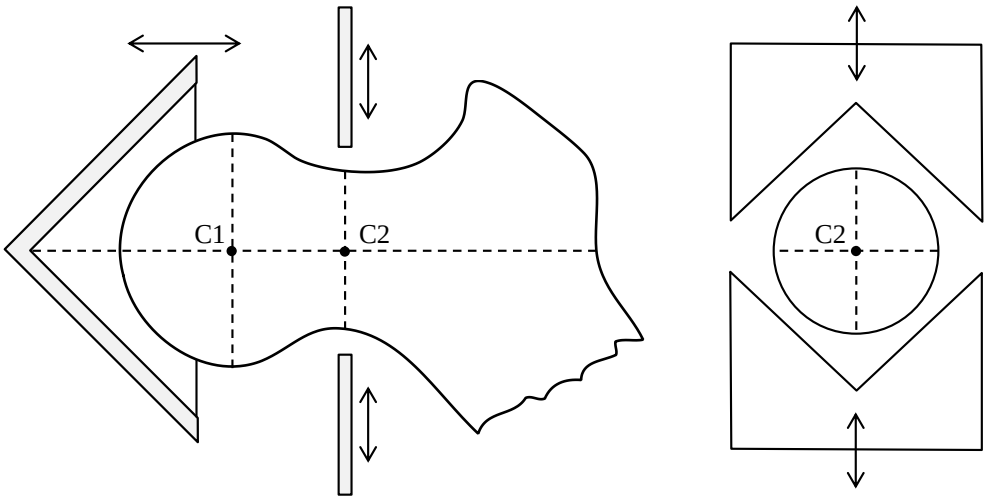

Fig. 4-1. Definition of the proximal femur's middle axis. The point C1 represents the center of the head and the point C2 represents the center of the neck.

After positioning the bone in the tool, two points of the middle axis could be mark out by means of a prick punch on the greater trochanter and with a trocar on the femur's head (Fig. 4-3).

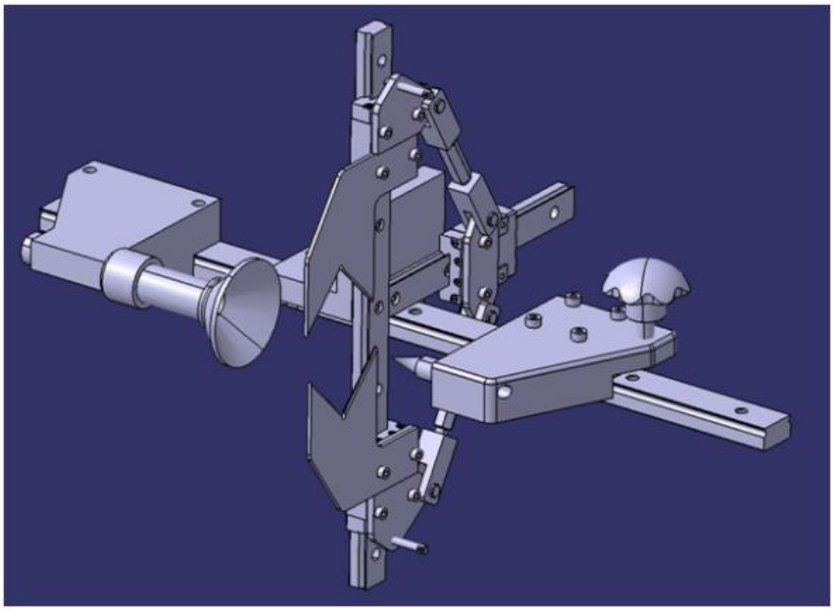

Fig. 4-2. CAD representation of the centering tool for the proximal femur.

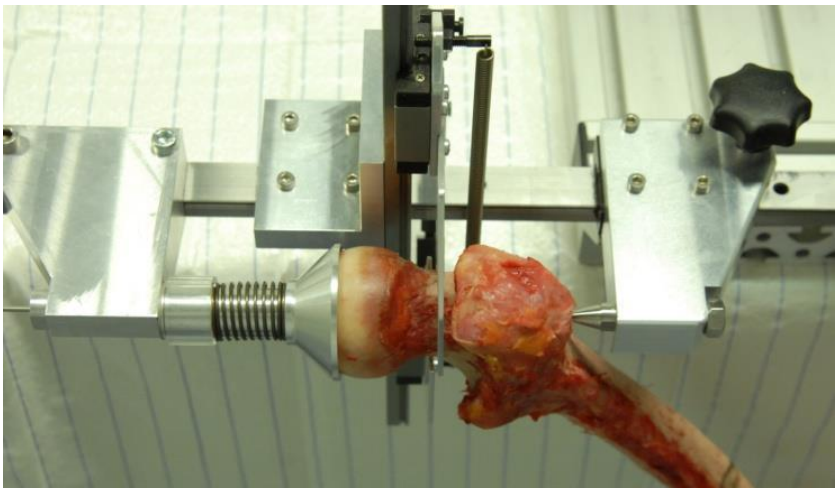

Fig. 4-3. Marking out of the reference points. The femoral neck is centered by the "v-blades" and the head by the conical part. A trocar goes through this part (left on the picture) to mark the point on the femoral head.

In order to define the first plane, the bone was laid on its three natural supporting points (condyles and lesser trochanter). The second necessary axis is found as the line that is orthogonal to the first axis and parallel to the supporting plane. The first cutting plane could be defined as that which contains the abovementioned two orthogonal axes.

A second tool was used to define this first cutting plane of the bone. It was attached by two trocars to the two markers on the proximal femur, which defined the middle axis. A third trocar was then inserted perpendicular to the other sides of the tool, which allowed to mark out a third point on the femoral neck. These three points would be used as landmarks for casting the bone in correct position (Fig. 4-4).

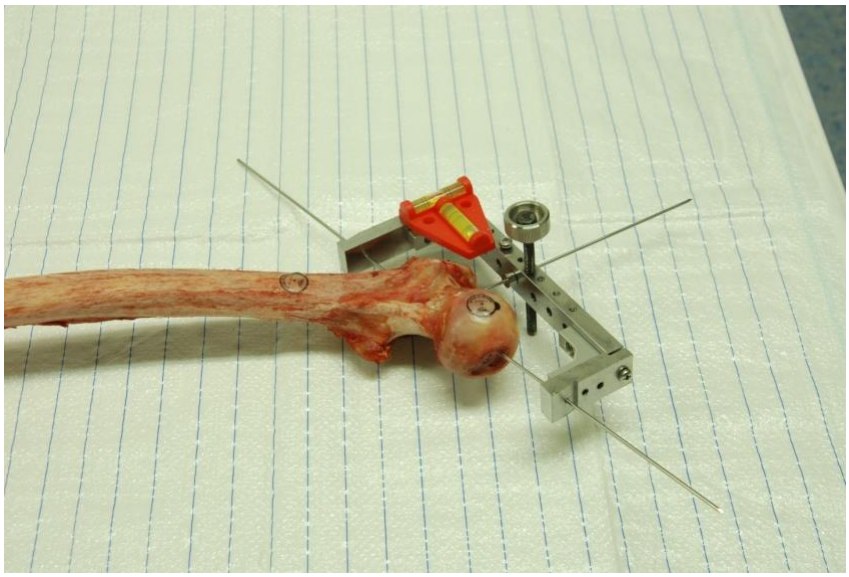

Fig. 4-4. Defining the first reference plane. The femur lies on its three natural landmarks (lesser trochanter and condyles). The tool is attached to it and the second axis leveled. A third reference point is marked out on the femural neck.

The third tool was a casting mold which enabled to hold the femur in the correct position during the molding using the three markers previously made. In this position, the proximal femur was molded in polyurethane resin (Rencast FC-53, see Table 3-2). The surfaces of the resin block were therefore used as a reference in the cutting process since they are each parallel to one of the three basic planes in the cartesian coordinate system. After demolding, the resin cast could be attached to a carrier that allowed the machining of the cubical specimens.

The casting mold comprises five aluminum plates bolted together (Fig. 4-5). Three of them have drillings to be able to carry the trocars that fix the bone in the proper position. The whole casting mold opens in an acute angle that allows enough space for bones even with a coxa-valga[1].

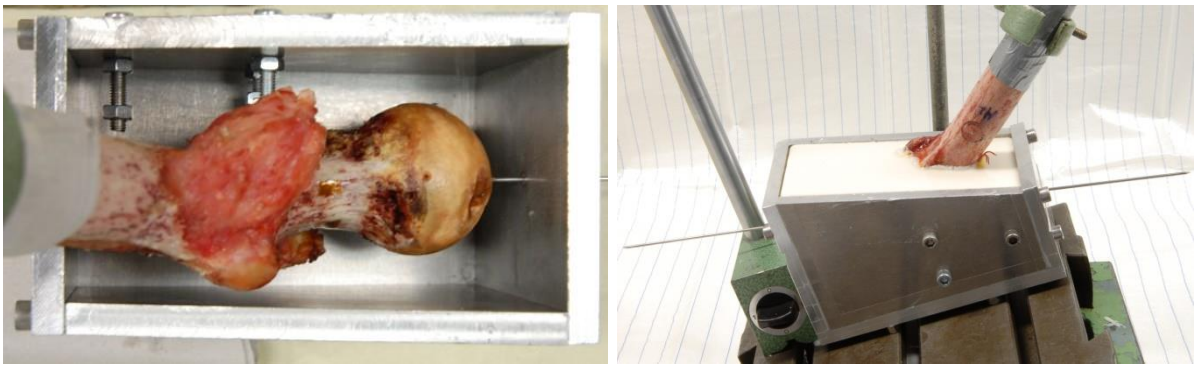

Fig. 4-5. Casting mold. The femur is properly placed by means of the reference points and three trocars. Then it could be cast with resin. The left picture shows the fixation screws. The nuts are embedded as well and provided support for fixing the resin cast to the band saw.

[1] Coxa-valga it is a deformity of the hip where the angle formed between the head and neck of the femur and its shaft is increased, usually above 135 degrees

One of the lateral plates of the tool holds three screws with distance nuts. These nuts remain in the mold during the molding and provide support to fix the femur on a carrier for the band saw (Fig. 4-6).

The frozen proximal femur was embedded in several layers of polyurethane resin as the manufacturer recommends, so avoiding thermal problems due to the exothermic reaction of the resin polymerization (Banse, et al., 1996).

From the head of three fresh frozen human femurs (50 year-old male, 1.81 m, 72.8 kg ; 62 year-old female, 1.62 m, 72 kg and 62 year-old female, 1.72 m, 92 kg) n = 18 cubical specimens (10 x 10 x 10 mm) were prepared. The femurs were macroscopically free of pathological lesions.

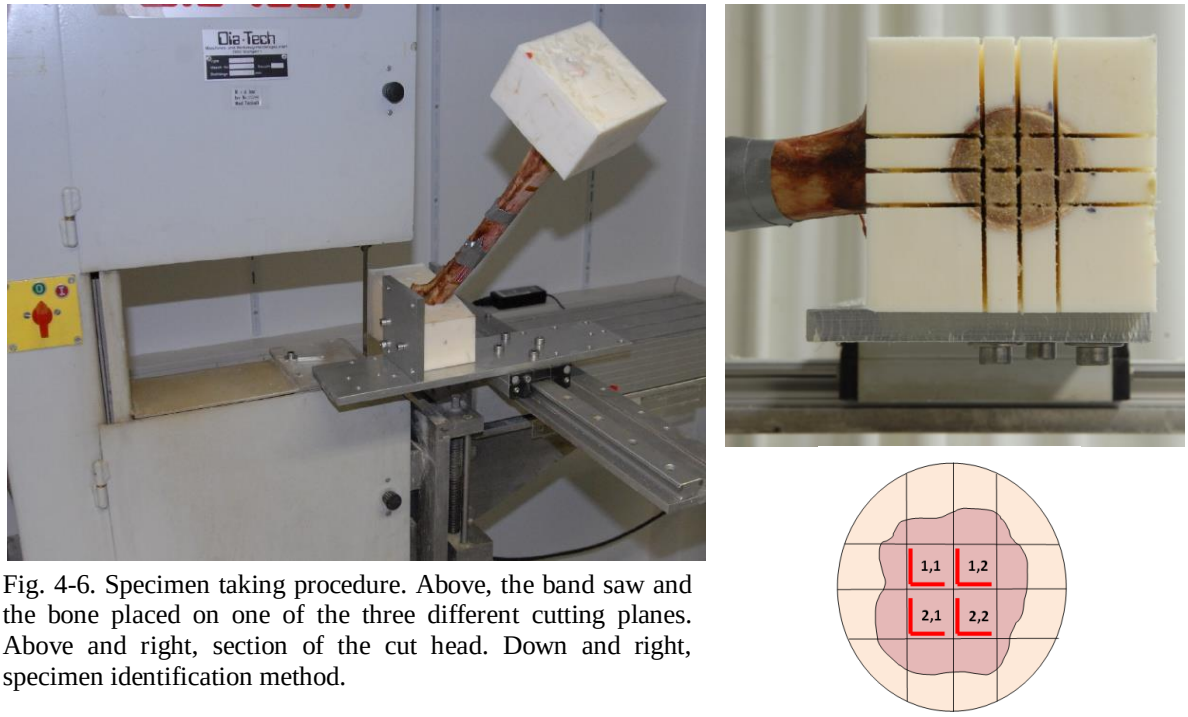

Fig. 4-6. Specimen taking procedure. Above, the band saw and the bone placed on one of the three different cutting planes. Above and right, section of the cut head. Down and right, specimen identification method.

The bone specimen was irrigated with 0.9% saline during machining using a low speed diamond saw (Dia Tech, Dia BS200, GmbH, Stuttgart, Germany) (Fig. 4-6). The cubical bone specimens were kept frozen at -20°C at all other times, except during mechanical testing. Previous to it, the specimens were thawed and degassed and mounted in plastic holders on a CT calibration phantom (Mindways USA). Thereafter CT imaging of the specimens was performed using a High Advanced Scanner (Philips). An average voxel resolution of 100 x 100 x 300 µm was obtained, resulting in scan images of 100 x 100 x 35 voxels per cubical specimen. The bone mineral density, BMD (mg of K_2HPO_4 per cm^3), of each specimen was measured in an 8x8x8 mm^3 cubical region of interest in the center of the specimen CT data.

4.2.2 Measurements procedure

The specimen dimensions were examined and measured three times with a caliper prior to the mechanical testing. Specimens damaged during the cutting process or with geometrical disproportion were rejected.

In order to be able to compare the elastic moduli calculated by the two experimental techniques using different strain measuring devices, a reference force corresponding to a "loading platens-strain" of 0.4% was established for mechanical testing of the specimens. This first approach presents some underestimation of the mechanical properties of the specimens as it was published by (Odgaard, et al., 1991). However, it may be considered as a safety factor, in such a way that the cubes were mechanically nondestructively tested (<0.4% strain) (Keaveny, et al., 1994; Kaneko, et al., 2004).

Thus, a first compression ramp was performed until -0.4% strain, measured directly from the displacement of the compression platens, for each cube and for each anatomic direction: superior-inferior (SI), anterior-posterior (AP) and media-lateral (ML).

All the tests were performed on a Zwick testing machine (Model 1120, Zwick Roell AG, Ulm Germany) with a set of compression platens, comprised by a fixed lower platen and an adjustable upper one (Fig. 4-7, Fig. 4-8). A compressive preload of 5N was first applied followed by a cyclic loading at a strain rate of 0.05% strain/s between the lower limit of 5N and an upper limit of the reference force for -0.4% strain, as mentioned above. The loading was repeated for 10 cycles in order to reach steady state (Keaveny, et al., 1997). Then, the strain was recorded both from an extensometer and from the displacement of the compression platens with a correction for system compliance (Keller, 1994).

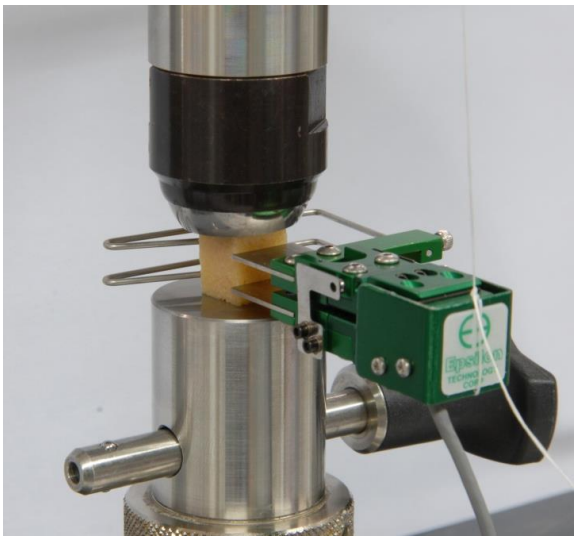

Fig. 4-7. Extensometer technique.

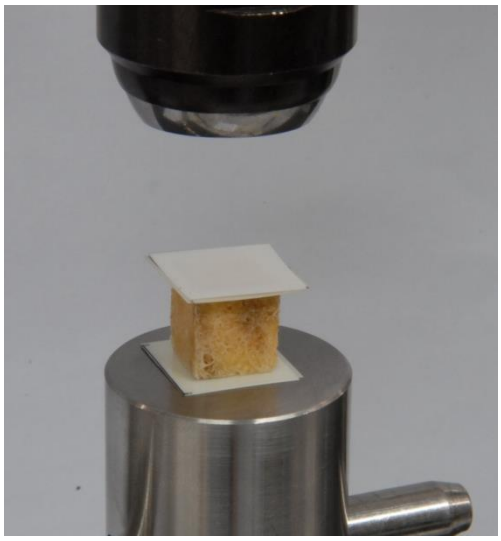

Fig. 4-8. Pressure film technique

4.2.3 Extensometer technique

The first considered technique was the extensometer technique. In order to minimize the end effects artifacts, the strain was recorded by a 5-mm gage length extensometer (Epsilon 3442-005M-010-ST, Epsilon Technology Corporation, Jackson, USA), which was directly attached to the center of the specimen. Four nondestructive tests were performed in each test direction, one with the extensometer mounted on each of the four vertical sides of the cube, for a total of 12 nondestructive tests per cube (Kaneko, et al., 2004). During the mechanical testing, several specimens were simultaneously and sequentially tested. The twelve nondestructive tests for each specimen were not performed consecutively. Between the individual tests the specimens were kept in saline solution. The weight of the

extensometer was counterbalance by means of a pulley system. The stress was expressed as the applied force divided by the total cross sectional area of the specimen perpendicular to the loading direction. Stress-strain diagram was represented using these data and the apparent elastic modulus for each direction was averaged from the four measurements of each testing direction.

Inaccuracies of the cubes' geometry as well as the inhomogeneous nature of them caused a dispersion of the four elastic modulus measured on the different sides. Furthermore, the cubical geometry of the specimens is more sensitive to irregular load distribution. According to Saint-Venant's Principle

"... the difference between the effects of two different but statically equivalent load becomes very small at sufficiently large distances from load."(Love, 1927)

The principle is nevertheless not applicable to the performed experiments, since the length is comparable to the cross section where the load is applied. Consequently, the most suitable manner had to be evaluated in order to assess the mean elastic modulus. Generally, and for the cases for which the four moduli were of similar value and order of magnitude, the arithmetic mean of the four values were calculated (eq. 4-1). However, the arithmetic mean could present some disadvantages in such cases that one value of the dataset is much larger than the others (Fig. 4-9). In these cases the harmonic mean provides a truer value of the average.

$$H = \frac{n}{\sum_{i=1}^{n} \frac{1}{x_i}} \qquad 4\text{-}1$$

In some extreme cases, one side could present an opposite elastic modulus (tension) due to a higher inhomogeneous load distribution. All of this was taken into account in the current analysis.

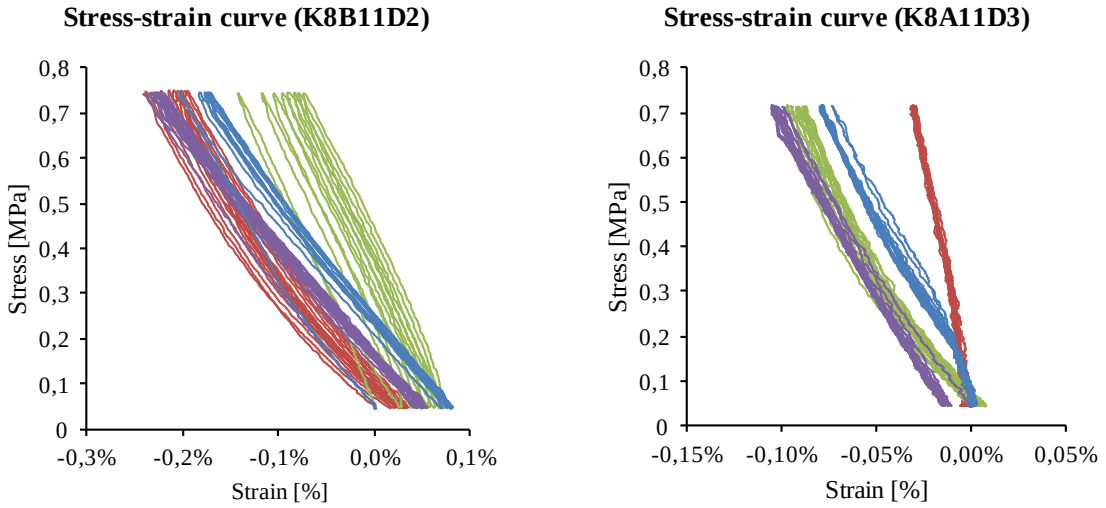

Fig. 4-9. Example of the four measurements of strain-stress curves taken by the extensometer for one testing direction. Right: the four measurements present similar values. Left: one measurement present higher value than the three others.

The averaging procedures were analytically validated by some proposed theoretical cases, which were calculated by means of FEA (7.2Appendix A, Appendix B). There, exemplary irregular load distributions and constraints were presented. The elastic modulus was measured in the same manner as the extensometer does, i.e. from the relative displacement between two lines separated 5 mm between them. The stress was evaluated as the force divided by the cross sectional area of the specimen (not the theoretical loading area). Elastic moduli were computed for each side of the virtual specimen and the better averaging procedure was established. Then, the experimental data could then be compared with the theoretical cases and the averaging procedure of the most similar of them could be applied.

4.2.4 Pressure film technique

After testing, the interface contact between the compression platens and the specimen was evaluated using a pressure measuring film (Fuji Prescale Super Low Pressure LLW). The contact area could not be measured simultaneously during the mechanical test because of the stiffness of the pressure film would distort the measurements of the specimens. Squared pieces of film were located on the lower and upper surfaces of the specimen and then a compressive ramp until the reference force was performed. As recommended by the manufacturer, the force was hold (±1N) for 2 minutes (Liggins, et al., 1995). In this way, two pressure maps were obtained for both specimen surfaces (upper and lower). In order to analyze this pressure maps and to estimate the contact interface area, the following image calibration approach was carried out before.

Image analysis calibration

Two cubical calibration specimens (10x10x10 mm) were made of biomechanical test material (Sawbones Polyurethane foam 30 pct and 40 pct, one each). These materials have similar mechanical properties to those expected of the bone specimens ($E_{30pct}^{comp} = 557\ MPa$; $E_{40pct}^{comp} = 943$, (MatWeb)) (Kaneko, et al., 2004). Compressive tests were performed in order to verify the material properties using constrained long specimens and macro extensometer (Zwick 325888).

Single compression test of the calibration specimens were carried out up to 150 N in the previously described manner. This force level was chosen regarding the upper limit of the bone specimen tests. The strain was measured from the corrected displacement of the compression platens. To assess reproducibility the measurements were repeated 10 times. Mean stiffness values were calculated from the slope of the force-strain curve, which was almost linear, at different points (80 N, 100 N, 120 N, and 140 N). For these load conditions, the interface contact area between the calibration specimen and platens was acquired using pressure measuring film following the same procedure as mentioned above. To assess the reproducibility of this procedure the pressure map was measured 6 times for one load condition (Liggins, et al., 1995).

The pressure films were scanned with high resolution at 2400 dpi (Canon Canoscan Lide 70) and then analyzed using an image processing tool (ImageJ, National Institute of Health, Maryland, USA). First of all, the scanned color images were converted from RGB

to 16 bits grayscale. Next, a series of segmentations were done using different threshold pixel values (Fig. 4-10). The area of each segmentation was measured as well as its pixel histogram (maximum Tmax, mean Tmean and minimum Tmin).

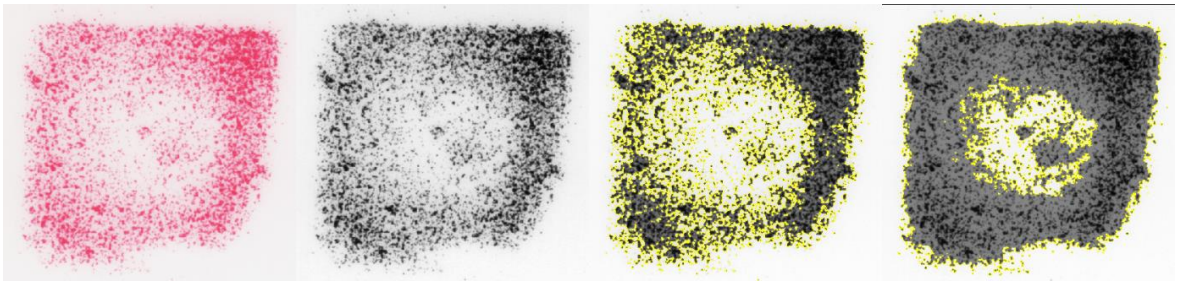

Fig. 4-10. Stain of the calibration specimen; a. original scan image; b. 16-bit image; c. and d. segmentations with different pixel threshold. The dark shade indicates possible contact areas.

The stiffness, calculated from the mechanical tests, was corrected using the area of the image analysis and recalculated in terms of elastic modulus. Since the mechanical properties of the specimen's material are well known, the most suitable segmentation and threshold could be interpolated from the closest segmentations. Following this procedure for other load conditions a calibration dataset (n = 8) (Liggins, et al., 1995), namely stress and pixel values could be generated.

A multiple linear regression analysis was used to investigate whether there was a relationship between the dependent variable (stress) and the independent variables (Tmax, Tmean, Tmin) and between the independent variables themselves.

For calibration, a multiple regression was created between the following variables:

$$y = C_1 x_1 + C_2 x_2 + \varepsilon \tag{4-2}$$

where,

$$y = \frac{F}{A_{eff}} = \sigma_{eff}, \qquad x_1 = T_{max} - T_{min}, \qquad x_2 = T_{mean} - T_{min} \tag{4-3}$$

The coefficients of the regression presented a high statistical significance (x1, $p < 0.01$ and x2, $p < 0.05$) which rejects the null hypothesis of null coefficients. A high correlation was found for the selected variables (adjusted $R^2 = 0.91$, $p < 0.01$).

The pressure films from the trabecular specimens were analyzed following the same procedure as for the calibration. A number of segmentations were performed across a wide threshold range. The parameters considered in the segmentation were: pixel values (Tmax, Tmean, Tmin) and area, which was conveniently converted to stress according to the applied force (known data). These values were introduced in the following function derived from the multiple regression:

$$f(\sigma, T_{max}, T_{mean}, T_{min}) = \sigma - [C_1 x_1 + C_2 x_2 + \varepsilon] = \sigma_{segmentation} - \sigma_{predicted} \tag{4-4}$$

The selected segmentation was that, which minimized the expression (4-4). Thus, predicted stress values were generated introducing the pixels values of each segmentation in the multiple regression, where the most suitable threshold value was determined. Since

the applied force was previously defined, the effective contact area could be determined from the predicted stress.

Then the effective contact area was used to correct the measurements of the corresponding mechanical tests recorded by the load cell and the displacement of the compression platens. Thus, an effective compressed geometry (Fig. 4-11) was taken into account in order to calculate stress-strain curves, from which the elastic moduli were to be evaluated.

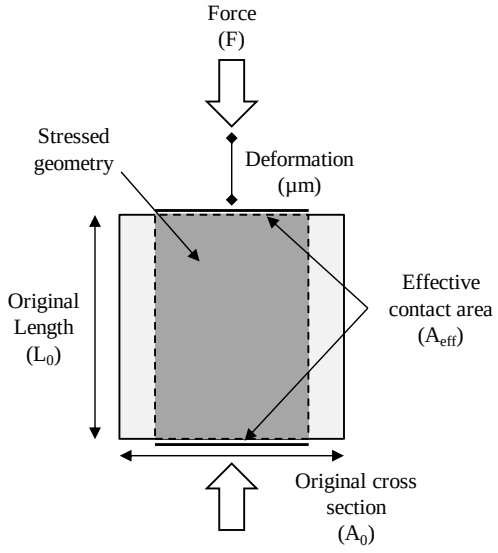

Fig. 4-11. Effective stressed geometry and parameters for calculation of the corrected elastic modulus.

An unpaired t-test was used to assess whether there were significant differences in the elastic modulus measurements between the two experimental techniques.

4.2.5 Estimation of errors

A coefficient of variation (CV) of the variable x was expressed as the root mean square standard deviation for repeated measurements in each testing direction (Augat, et al., 1998).

$$CV = \frac{1}{3n}\sum_{1}^{3n}\frac{\sqrt{\frac{1}{4}\Sigma_i^4(x_i-\bar{x})^2}}{\bar{x}} \qquad 4\text{-}5$$

4.3 Results

As it was previously described, the mechanical testing consisted in two different approaches. On the one hand, the extensometer technique considered the total cross section of the specimen for the determination of the stress and the displacement of an extensometer attached directly to the middle of the specimen for the determination of strain. On the other hand, the pressure film technique considered the corrected displacement of the compression platens for the calculation of strain and the stress were corrected using the effective contact area between specimen and compressive platens.

The results from both experimental approaches were compared in a mirror presentation (Banse, et al., 1996), for a simpler visualization of them (Fig. 4-12).

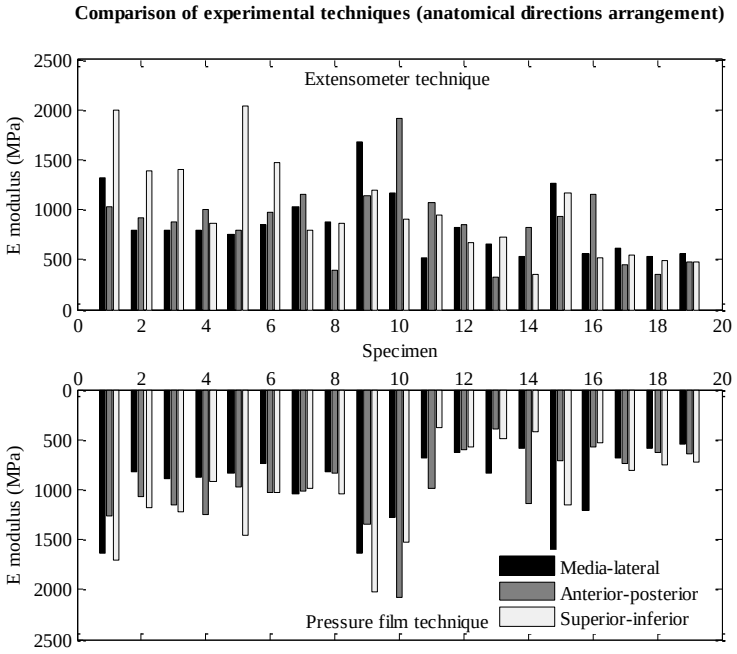

Fig. 4-12. Comparison of the experimental techniques. Elastic moduli are arranged by anatomical directions.

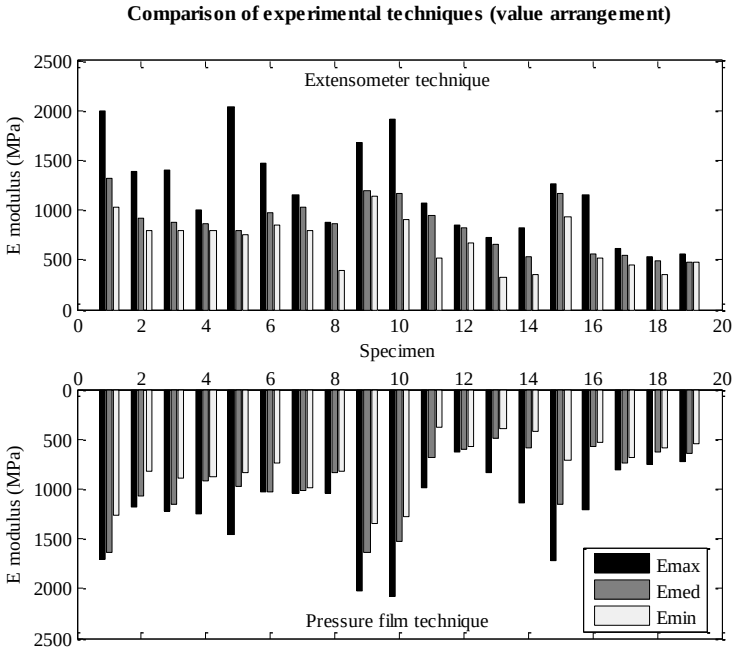

Fig. 4-13. Comparison of the experimental techniques. Elastic moduli are arranged by order of magnitude.

As it was explained in section 4.2.1, the anatomical directions of the specimens may not coincide with the main trabecular directions. Therefore, the anatomical directions may

not be comparable between specimens. The elastic moduli were also ranked by their values in descending order:

In the same manner, the data arranged by value was statistically presented in box-and-whisker plots.

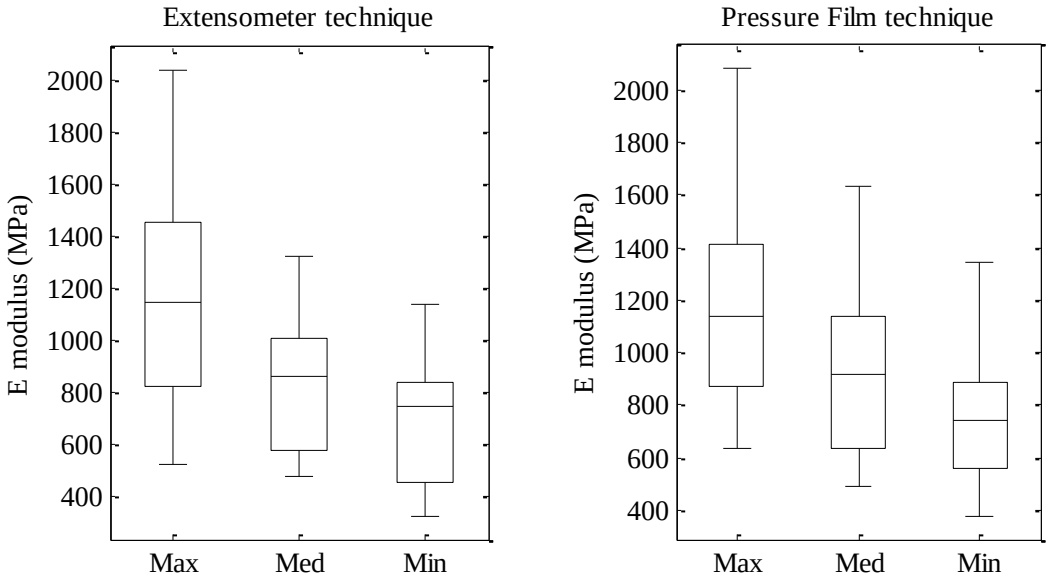

Fig. 4-14. Statistical representation of the results (data arrangement by value).

The data plotted above show that both experimental techniques yielded similar values of elastic modulus. To conclude whether there was a significant difference between the results of both techniques, a statistically analysis was carried out, as follows.

A statistical summary of all results are presented in Table 4-1.

Table 4-1. Summary of the elastic measurements of both experimental techniques and the bone mineral density analysis.

		E modulus [MPa] mean ± SD (range)				BMD [mg/cm³]
	CV (%)	SI	AP	ML	Mean	Mean ± SD
Compression test (uncorrected)	14.8 %	377± 176	378 ± 149	400 ± 139	385 ± 136	
Pressure film technique	16.0%	996 ± 455 (374-2024)	971 ± 380 (397-2084)	950 ± 371 (550-1713)	972 ± 339 (574-1668)	318 ± 54 (229-431)
Extensometer technique	N.A.	991 ± 492 (347-2042)	874 ± 376 (324-1909)	847 ± 317 (513-1677)	904 ± 305 (457-1450)	

No statistical significant difference was found between the measurements of the two techniques ($p = 0.07$, paired t-test). Additionally, the mean elastic modulus was significantly correlated with the BMD in both methods. The data from the extensometer

presented a higher correlation ($R^2 = 0.77$, $p < 0.01$) than the data from the pressure film technique ($R^2 = 0.65$, $p < 0.01$) (Fig. 4-15).

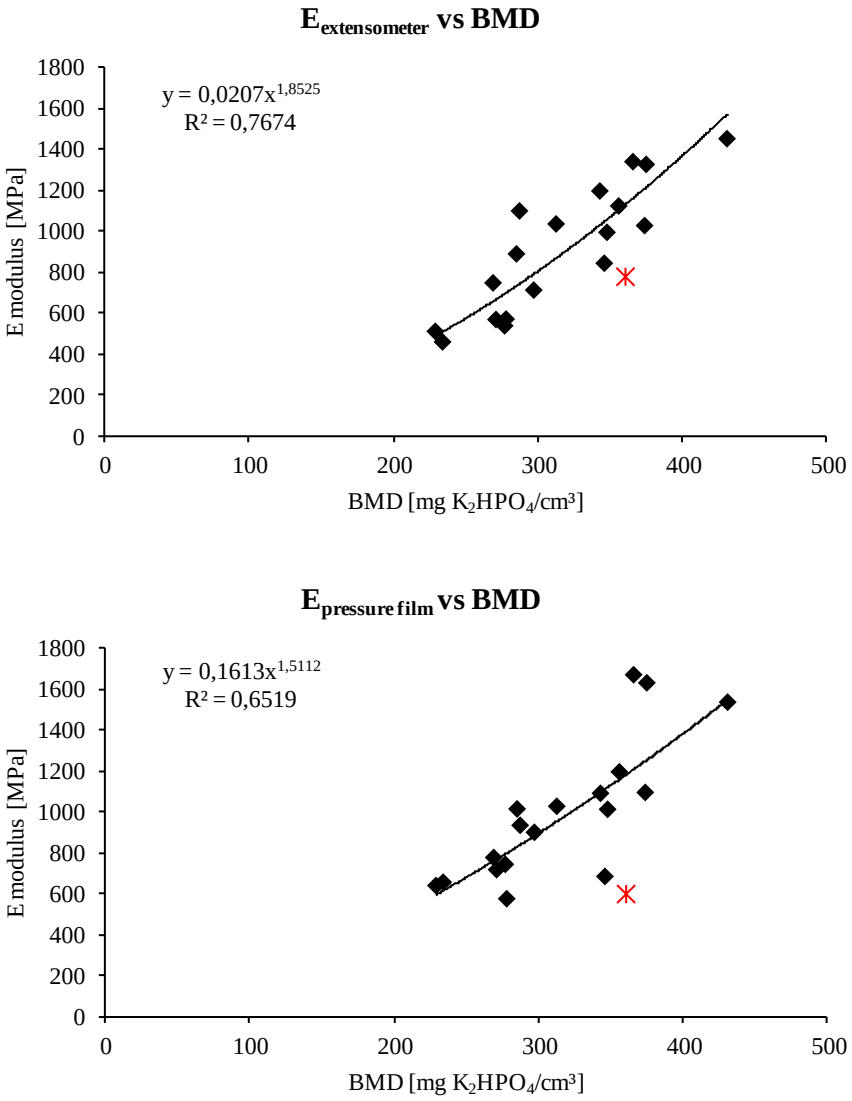

Fig. 4-15. Linear regression of the mean elastic modulus versus BMD, above the extensometer technique and below the pressure film technique. The measurement plotted by a red mark corresponds to one specimen which could be damage during the mechanical testing due to some technical problems and it was not introduced into the analysis.

The difference between the results from the compression test with and without the area correction was in the range of 24-67%.

Conversely, no significant difference was found in the compressive moduli between the different testing directions for both techniques. The highest difference was found for the extensometer technique between the measurements of SI and ML directions ($p = 0.07$). This result may be taken as evidence of the aforementioned remark concerning the mismatch of the anatomic and trabecular directions. Nevertheless, all specimens presented individually a high elastic anisotropy.

Afterward, the elastic moduli (ranked by value, i.e. E_{max}, E_{med}, E_{min}) were also correlated with the BMD in order to describe the orthotropic properties of the specimens (Fig. 4-16). The most significant difference was found for the results of the extensometer method between the E_{max} direction and the E_{med} ($p = 0.012$) and E_{min} ($p < 0.01$). The latter directions presented a lower but also significant difference ($p = 0.046$).

Finally, from this orthotropic representation a transversely isotropic material model was proposed by averaging the values of the E_{med} and E_{min} directions.

(a) (b)

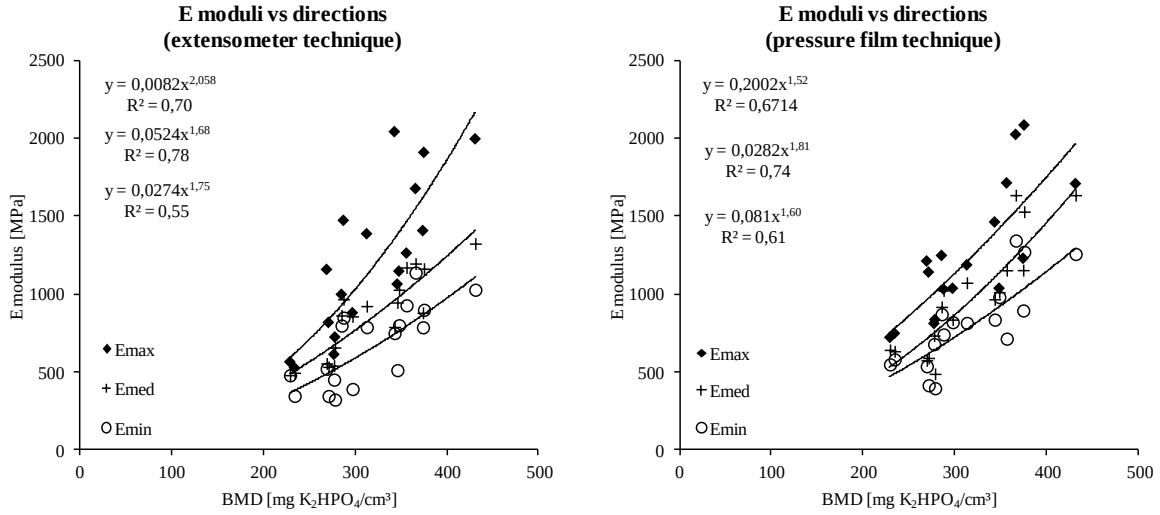

(c)

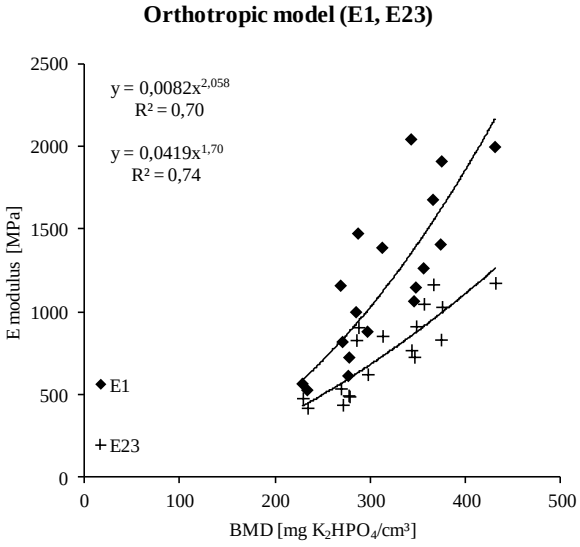

Fig. 4-16. Regressions of the orthogonal elastic moduli for the two experimental techniques. The data were ranked by value, (a) extensometer technique, (b) pressure film technique, (c) proposed orthotropic model (transverse isotropic).

4.4 Discussion

The aim of this section was to investigate trabecular bone's compressive behavior taken into consideration its orthotropic properties. In order to achieve this analysis, unconfined cubical specimens, extracted from three femoral heads, were submitted to mechanical test. Two different methods were used to overcome the experimental inaccuracies associated to the compression testing of unconfined specimens. First, the well known extensometer technique enabled the correction of the strain, which were measured directly on the sides of the specimens. Additionally, the most suitable averaging procedure was established by means of finite element analysis of the experimental method. Thereafter, the compressive modulus was highly correlated ($R^2 = 0.77$) with the bone mineral density measured from QCT scans of the specimens. The correlation coefficients obtained in the present study are consistent with values usually reported in the literature for the same experimental procedure ($R^2 = 0.74 – 0.84$, Kaneko et al. 2004) ($R^2 = 0.79$, Ciarelli et al. 1991).

Second, a new experimental technique was developed for evaluating the effective contact interface in compressive testing of unconfined trabecular bone specimens. By means of pressure sensitive film and a calibration image analysis, the effective contact area between the trabecular specimens and the compressive platens was assessed. This parameter was subsequently used in order to correct the calculation of the stress and thus of the experimental elastic modulus. Then, the elastic moduli of the specimens measured by the two experimental methods were statistically compared. The experimental results showed that there were no significant differences between the two techniques. This similarity between methods might be interpreted in such a way that the underestimation due to the effective contact area represents a substantial source of the end artifacts.

A limitation of the pressure film technique may lie on the pressure film sensitivity as well as on the calibration specimens which were used in the approach. The trabecular specimens, which were tested in this study, presented a relatively high bone mineral density (318 ± 54 mg/cm³). The influence of the selected calibration specimens has to be studied in future works and especially for the study of trabecular specimens with a low mineral density.

The underestimated elastic moduli from the uncorrected compressive test were in the range of 29-70 % with respect to the corrected values. This result confirmed the well known significant influence of the end artifacts in compressive testing. Keaveany (1997) reported a percentage difference in modulus due to end-artifacts as much as 86% for individual specimens and an underestimation range of 20-40%. The different specimen sources (bovine and human), geometry and methods may explain the difference between the present results and the lower difference values reported by Keaveny. However, the uncorrected elastic moduli reported in the present study are in consonance with those reported in the literature of unconfined testing (Linde, et al., 1992; Keyak, et al., 1994; Augat, et al., 1998).

The results also presented no statistical difference in the compressive mechanical properties for the different anatomic directions. The explanation of this result may consist in the differences between the anatomical direction and the main trabecular direction as it was reported by Öhman et al. (2007) concerning the article of Birnbaum et al. (2001). However the present study did not focus on the analysis of the orthogonal mechanical directions of the trabecular bone. In that respect, a standardized sample-taking procedure was also proposed. It based on some morphological landmarks (i.e. head-neck axis, condyles-lesser trochanter plane) of the bone to define the anatomical directions.

In conclusion, the pressure film technique may be used to quantify the effective contact area. It may be also preliminary considered an experimental alternative in compressive testing of unconfined trabecular bone for the determination of the elastic properties with partial end effects correction. Specific calibration procedure should be considered in the future, taking into account the mechanical and physical properties of the studied specimen material.

5 Patient-Specific Finite Element Analysis of the Human Femur

5.1 Introduction

The prediction of the elastic mechanical response of individual patient's bones may represent a great advantage in orthopaedic medicine. For instance, it may be used to prevent or reduce the stress shielding of bone and thus the associated problems, such as the aseptic loosening of prostheses. Besides, it has been reported that the bone presents at the macro-level elastic linear response for loads in the normal range of regular daily activities (Keaveny, et al., 1994).

In the past two decades, three-dimensional finite element (FE) analyses in conjunction with high resolution quantitative computed tomography (QCT) were carried out for predicting bone's mechanical behavior (Keyak, et al., 1990; Mertz, et al., 1996; Viceconti, et al., 1998; Yosibash, et al., 2007). The high resolution QCT enables the geometrical reconstruction of the bone based on its mineral density distribution, referred to in Hounsfield units (HU). Some correlations have been made between density measures and elastic properties (Keller, 1994; Rho, et al., 1995; Keyak, et al., 1994; Kaneko, et al., 2003). These correlations are reported in terms of apparent density, ash density or even in HU. Commonly the correlations are conveniently converted in terms of equivalent mineral density [K2HPO4 mg/cm³] (BMD) by means of some CT calibrations (Yosibash, et al., 2007).

The $E(\rho_{QCT})$ empirical relations used in these FE models were obtained by independent studies and from different bones (Bessho, et al., 2007; Yosibash, et al., 2007). In some cases the densitometric measures were not directly connected to CT measures and additional density relations had to be specifically proposed (Taylor, et al., 2002; Peng, et al., 2006; Trabelsi, et al., 2011).

Orthotropic models have been also reported, Peng et al. 2006, for example, made a theoretical comparison between FE models using inhomogeneous isotropic and orthotropic properties. However, the models were not validated through experimental data. In other studies, the orthotropic properties were derived by micromechanical homogenization approaches (Trabelsi, et al., 2011).

The experimental field may provide the necessary data to create and validate FE models. The material properties of the bone can be assessed from tests of some bone specimens and used to create mechanical models. The results of the simulations can be compared with the results from tests of the complete bone, both sharing the same boundary and load conditions.

The research analysis presented in this section focused on the elastic mechanical response of the human femur in combination with the experimental results of the previous chapters. Therefore, the bone material models proposed in this research project as well as from the literature were introduced into FE models and the predictions were compared with the experimental results from Chapter 3. Additionally, the bone anisotropy (i.e. orthotropy) was analyzed and some models were presented and compared to the isotropic ones.

5.2 Method

From the tested femurs, whose results were presented in Chapter 3, complete QCT scans were performed previous to the mechanical tests. The modeling of the bones included the following tasks:

- CT-Scanning and referencing of coordinate systems.
- Segmentation of the QCT scans. Boundary detection and CAD modeling.
- Material models and spatial bone mineral density function.
- Loads and constraints definition.

5.2.1 CT Scanning and referencing

The QCT scans were performed on a High Advanced Scanner (Philips) with the following parameters:

Table 5-1. Parameters of the QCT scans of the femur specimens (n = 6)

Specimen	Pixel size [mm]	Slice thickness [mm]
B3	0.38	0.5
B4	0.28	0.67
B5	0.14	0.67
B6	0.14	1.5
B7	0.15	0.75
B8	0.21	1

Image matrix 1024x1024,Voltage 120 kVp

For comparison reasons, the resolution of all CT scans was homogenized to a average resolution of 0.3x0.3x1.2 mm, when applicable.

In order to make comparable the results from the tests and from the FE simulations, it is completely necessary to know the exact position of the bone during the test regarding the applied forces as well as the position of the strain gages and displacement points. Moreover, this geometrical dataset should be transferable to the virtual coordinate system from the CT scans and FE models.

For that purpose, as it was mentioned on Chapter 3.2.1, a set of four CT-landmarks (Fig. 5-1) (Spee-D-Mark™, St. John Companies) were attached to the bones for connecting the coordinate system of the CT scan, and subsequently of the FE Simulation with the coordinate system of the experimental setup.

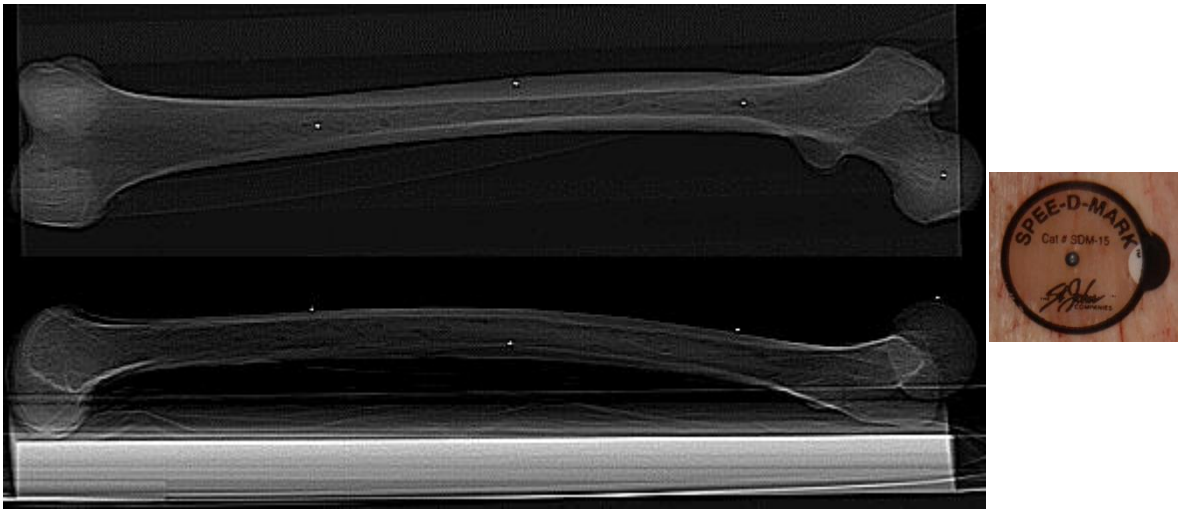

Fig. 5-1. CT-Landmarks used for referencing the coordinate systems of the experiments and CT scans.

In the course of the mechanical testing, the coordinates of the landmarks and other points of interest (POI) (i.e. locations of the constraint, load, strain gages, displacement points) were recorded by means of the Microscribe. In the same way, from the CT-scans the coordinates of the landmarks were determined. Thereby, the exact position of four points was known in both coordinate systems, which enables the calculation of a coordinate system transformation.

The coordinate transformation consisted in a translation and rotation and can be described by the following matrix equation:

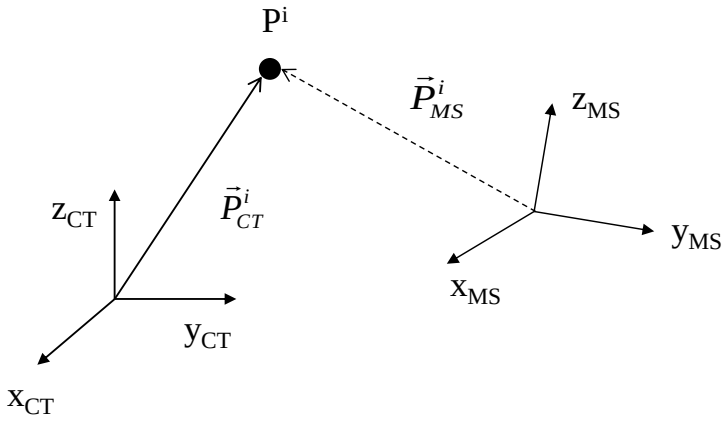

$$P^i_{CT} = P_{MS \to CT} + T_{MS \to CT} \times P^i_M \qquad 5\text{-}1$$

where P^i_{CT} is the position vector of a point P^i in the coordinate system of the CT; $P_{M \to CT}$ is the translation vector between coordinate systems; $T_{MS \to CT}$ is the rotation matrix; and, P^i_M is the position vector of the point P^i in coordinate system of the Microscribe.

The translation vector and the rotation matrix can be calculated solving a linear equation system. This problem requires at least four reference points, whose position should be known in both coordinate systems. For that reason, four CT landmarks were attached to the bones to calculate the coordinate transformation. First, the equation system was solved using a symbolic math toolbox to obtain the general expressions of the rotation matrix's coefficients. Second, a MatLab function was written from these expressions in order to determine easily both the rotation matrix and translation vector from the position vectors of the CT landmarks for each bone (Appendix D). Thereafter, the coordinates of the POIs in Microscribe system were conveniently converted into CT system using the transformation equation 5-1.

5.2.2 Estimating densities with the CT calibration phantom

The CT Calibration Phantom is composed of a plastic base material containing 5 rods of reference material embedded in the plastic base (Fig. 5-2). The base material is not used as a reference material. The reference materials contain known and varying amounts of low and high atomic number materials.

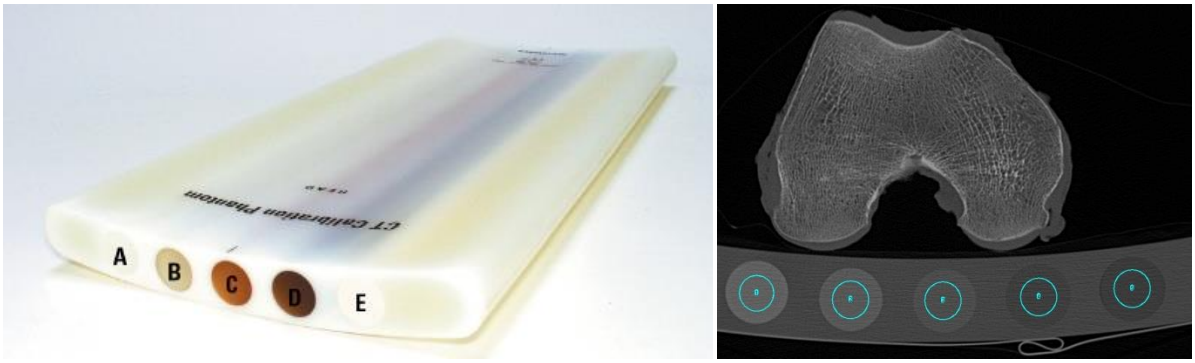

Fig. 5-2. CT calibration phantom. The 5 rods contain reference materials corresponding to different equivalent density values.

The following table contains information about the equivalent water and K_2HPO_4 densities for the calibration rods, which are labeled as shown below.

Table 5-2. Composition of the solid reference materials of the CT phantom.

Reference rod	Eq. H20 density (mg/cc)	Eq. K_2HPO_4 density (mg/cc)
A	1012.2 ± 2.3	-51.8 ± 0.1
B	1057.0 ± 1.9	-53.4 ± 0.1
C	1103.6 ± 1.7	58.9 ± 0.1
D	1119.5 ± 1.8	157.0 ± 0.3
E	923.2 ± 2.1	375.8 ± 0.9

This section outlines basic methods for estimating the densities of unknown materials within a CT image relative to the known densities of the CT Calibration Phantom reference materials (Table 5-2). The densities estimated using the techniques outlined in this section are referred to as K_2HPO_4 equivalent densities. The bone can be characterized by estimating the density of K_2HPO_4 dissolved in water that would have the same attenuation properties as bone under the conditions used to acquire the CT image data.

The following equation shows the relationship between the different parameters:

$$\rho_{K_2HPO_4}(unknown) = \frac{\mu_{ROI} - \beta_{CT}}{\sigma_{CT}} \quad 5\text{-}2$$

where

μ_{ROI} = CT number within a region of interest (ROI) in a reference or unknown material, in HU

$\rho_{K_2HPO_4}$ = K_2HPO_4 equivalent density of the material within the measured ROI

σ_{CT} and β_{CT} = are density estimates.

The analysis techniques use ROI measurements within reference materials of known composition to estimate σ_{CT} and β_{CT}. Once these parameters are known, then the equivalent K_2HPO_4 density ($\rho_{K_2HPO_4}$) can be estimated from an ROI measurement of the unknown material.

The density estimates can be calculated from the next equation (5-3) and from the measurements of the reference materials:

$$\mu_{ROI} = \rho_{water} + \sigma_{ref} \cdot \rho_{K_2HPO_4} + \beta_{ref} \quad 5\text{-}3$$

Each reference material ROI measurement corresponds to a measurement of μ_{ROI} on the left hand side of equation 5-3. $\rho_{K_2HPO_4}$ and ρ_{water} are assumed known for each measurement and are provided on the calibration by the manufacturer. Thus, the estimation of σ_{ref} and β_{ref} reduces to a linear estimation problem that can be handled by standard linear regression techniques.

Finally the density estimates σ_{CT} and β_{CT} can be related as shown in the following equations which are provided by the manufacturer as well:

$$\sigma_{CT} = \sigma_{ref} - 0.2174 \quad 5\text{-}4$$

$$\beta_{CT} = \beta_{ref} + 999.6 \quad 5\text{-}5$$

Introducing the density estimates in equation 5-2, the bone mineral density can be calculated in terms of K_2HPO_4 for each voxel in the CT-scans.

5.2.3 Segmentation and generation of FE models

The goal of segmenting a CT image data is to reconstruct or build the three-dimensional geometry structure to be analyzed, in the present case, the femur.

The flowchart for generation of the FE models can be summarized as follows (Fig. 5-3):

a. Segmentation of the CT images.
b. Boundary and point cloud generation.
c. Surface model
d. Solid model and material properties (BMD distribution)

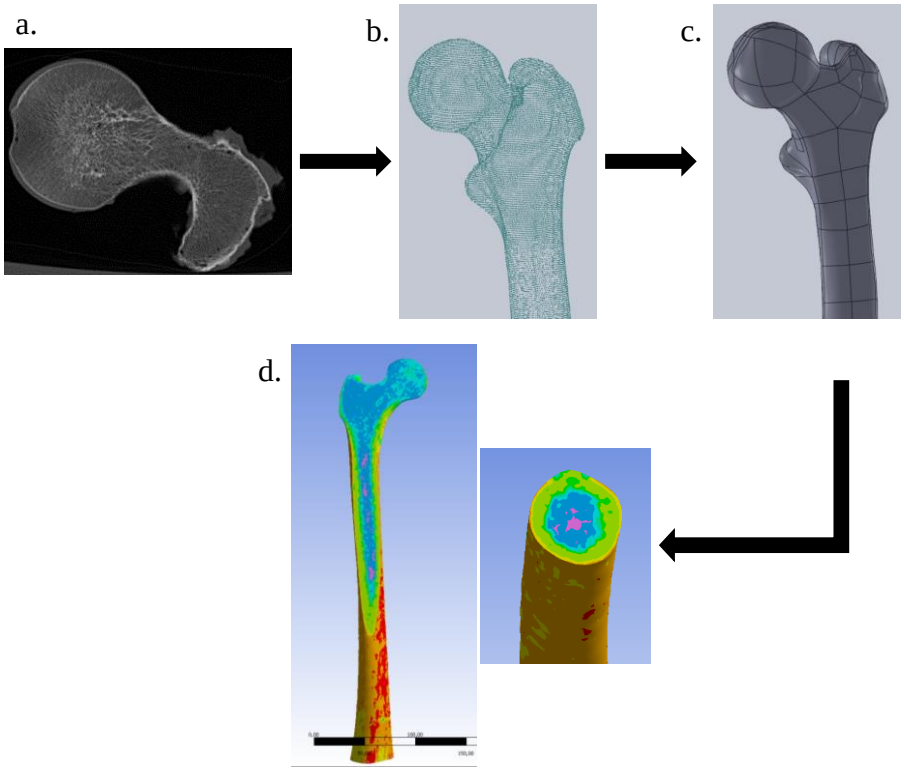

Fig. 5-3. Flowchart for generation the FE models: a. segmentation of the CT images; b. boundary of the bones and point cloud; c. surface model; d. solid model and material properties (BMD distribution).

The segmentation of the CT images consisted in extracting the coordinates of the voxel lying on the boundary surface, which encloses the structure. A semi-automated procedure was developed using the image processing program ImageJ. It is a Java-based open source program developed at the National Institutes of Health (NIH) of the United States.

The segmentation procedure can be also divided in the next sub-processes:

1. Region of interest selection where the femur is enclosed
2. Thresholding and binary conversion
3. Closing binary and filling holes
4. Median filter (smoothing)
5. Binary outline
6. Save XYZ coordinates of each voxel

The CT images with a resolution of 1024x1024 pixels (Table 5-1) depicted a wider scanning region, including the bone and the CT phantom; the latter used for density conversion. Then, unnecessary items within the scans could be omitted, thus reducing the region to be segmented.

The outer shell of the bone presents a higher bone density, which allows to perform a preliminary segmentation by thresholding. The selected threshold was defined to cover the highest bone densities of trabecular and cortical bone. After thresholding, the image was converted to a binary image, which presented empty spaces. An iterative process was applied to close the binary image and afterwards the empty holes were filled out. Because of the porous nature of bone, the outer contour for some slices should be manually closed. Once all bone contours were filled, they could be smoothed by means of o median filter. This is a nonlinear image filtering technique which is often used to reduce or remove noise. Thereafter, a series of smooth contour outlines could be generated (Fig. 5-4). Finally, the program ImageJ allows to write to a text file the pixel coordinates of all non-background pixels in the active CT image stack. The text file with the coordinates of the voxels on the boundary could be treated as a "point cloud".

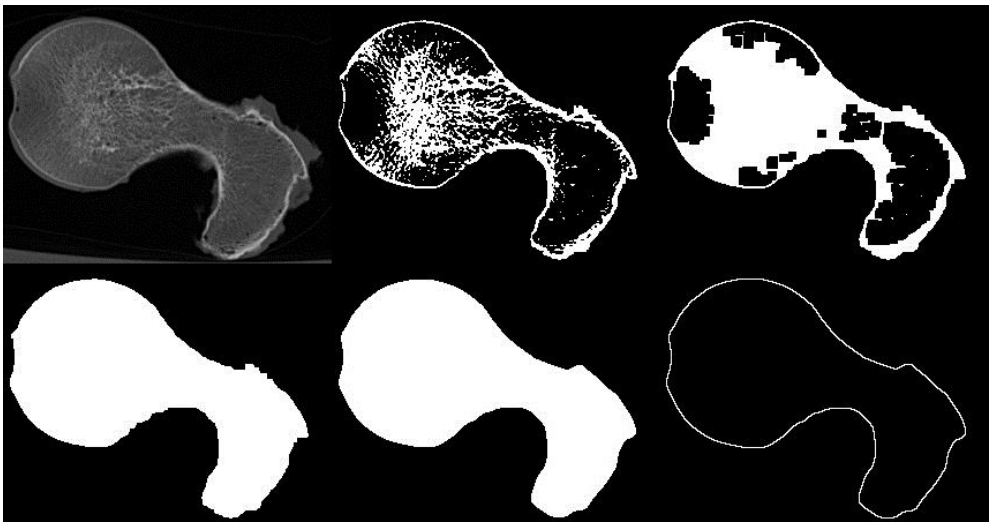

Fig. 5-4. Segmentation of the CT images.

The point cloud could be imported in SolidWorks (Dassault Systèmes SolidWorks Corp.) and conveniently converted to a surface CAD model. The position and area where the strain gages were attached were included in the surface model to simplify the post-

processing data analysis. Thereafter, the surface model could be directly imported by the FE software (Ansys Inc.).

5.2.4 Mesh generation

The FE mesh models were generated using 3-D 10 node quadratic tetrahedral elements by the patch conforming method. The Patch Conforming Tetra mesh method is a Delaunay tetra mesher with an advancing-front point insertion technique used for mesh refinement (ANSYS Inc. Release 13.0, Documentation).

To investigate the model convergence, several models were created with different mesh refinements (630k, 470k, 360k, 150k, 66k nodes) corresponding to elements measuring 1.8, 2, 2.2, 3 and 4 mm, respectively. The mesh quality, i.e. element size, aspect ratio, angle between faces, was controlled using an internal routine of ANSYS (Fig. 5-5) to determine the number of distorted elements.

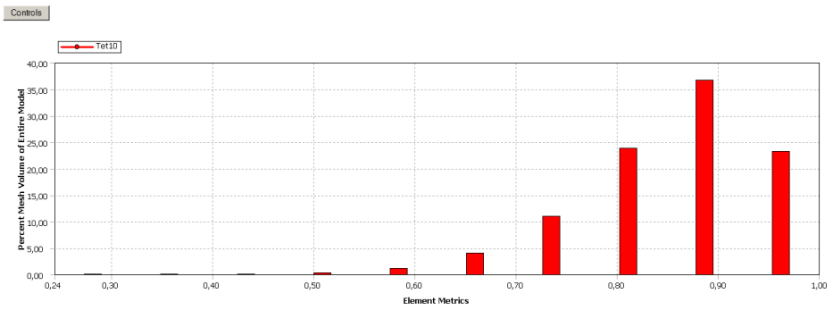

Fig. 5-5. Example of the Ansys metric "element quality" for the mesh refinement 470k. The element quality provides a composite quality metric based on the ratio of the volume to the edge length for a given element. A value of 1 indicates a perfect cube or tetrahedron while a value of 0 indicates that the element has zero or negative volume.

For each of the models, total strain energy was calculated at a load of 1000N under the same loading and boundary conditions. Data on the total strain energy were compared among the models.

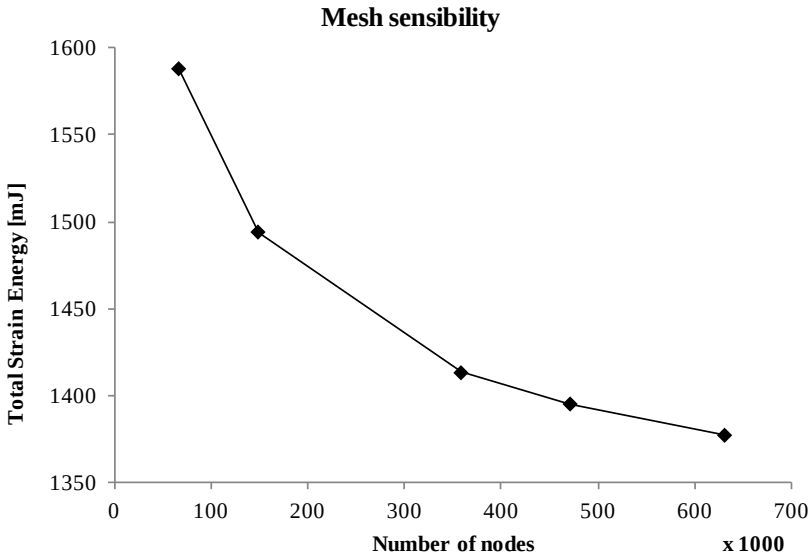

Fig. 5-6. Mesh sensitivity. Total strain energy was compared between the different mesh refinements.

The total strain energy of the simulation model was increased by 1.3% with decrease of the mesh refinement from 630k to 470k nodes. With a decrease from 630k to 360k nodes, it increased by 2.6%. The next refinement (150k nodes) supposed an increase of 8.5%. Therefore, the 360k nodes model corresponding to an element size of 2.2 mm was thought to achieve sufficiently precise prediction compared with the 470k and 630k nodes models, which were the most accurate among the five models (Fig. 5-6). The average computing time for the 630k nodes model was more than 6 h, but it was about 1 h for the 360k nodes model. Keyak and Skinner (1992) previously recommended adopting an element size of less than 3 mm. For these reasons, an average element size ranged from 2 to 2.3 mm was adopted generating FE models with approximately 400k nodes (Fig. 5-7).

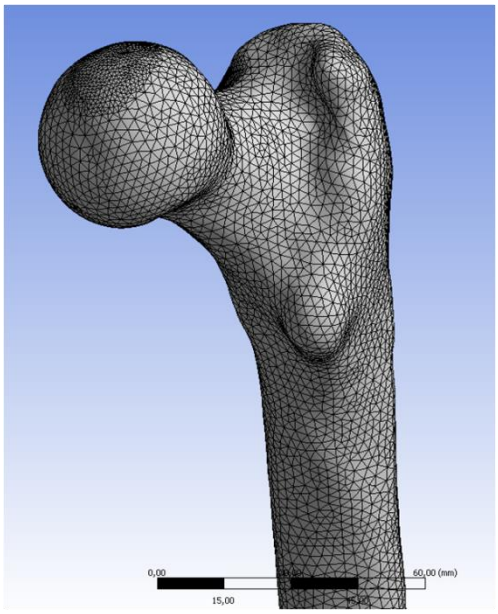

Fig. 5-7. Example of mesh refinement used in the models.

There is although a remarkable aspect of the presented sensitivity analysis. Since the material properties of the model are averaged and interpolated from the CT data, the properties of the model depends on the mesh. Homogeneous and isotropic model was also created to evaluate the mesh sensitivity from the point of view of the geometry. The variation of the total strain energy for the homogeneous model was less than 1% for all the mesh refinements above proposed.

The FE analyses were run on a workstation with dual core 2.0 GHz CPU and 4.0 GB RAM.

5.2.5 Material properties assignment

As it was mentioned in previous chapters, bone, in this instance the human femur, consists of a heterogeneous material. From the point of view of continuum mechanics, the elastic properties of bone could be assessed from its different densitometric measures (Keller, 1994; Rho, et al., 1995; Kaneko, et al., 2004). CT scans enables the generation of a three dimensional distribution function of the bone mineral density, referred to as K_2HPO_4 equivalent density. The latter could be consequently correlated with the mechanical properties of the bone specimens, which were experimentally obtained in the Chapter 4.

Thus, the first step consisted of the construction of the mentioned bone density distribution function from the CT images. At this point, it was convenient to regard the requested data structure when importing it from the FE software. This consideration facilitated the building of the FE models and helped to reduce the computation time.

Taking all of this into account, the CT images were converted to text images, where the voxel values (HU) were stored in an array, whose dimensions were the same as those of the images. A MatLab function (Appendix D) was created to automatically read the text image stacks of each bone and to adequately arrange and convert the data into equivalent mineral density. Then, the function generates the requested distribution function in an ASCII-text file.

The data was formatted as an ANSYS "Table array parameter" (Fig. 5-8). This type of variable consists of numbers arranged in a tabular fashion and has some specific features:

- A table array contains a 0 row and column used for data-access index values, which should be explicitly declare for each row and column.
- ANSYS can calculate (through linear interpolation) any values that fall between the explicitly declared array element values.

The latter functionality enables from the discrete distribution function the evaluation of the bone density within the whole CAD model. Obviously, both boundary and material distribution function shared the same coordinate system from the CT scans.

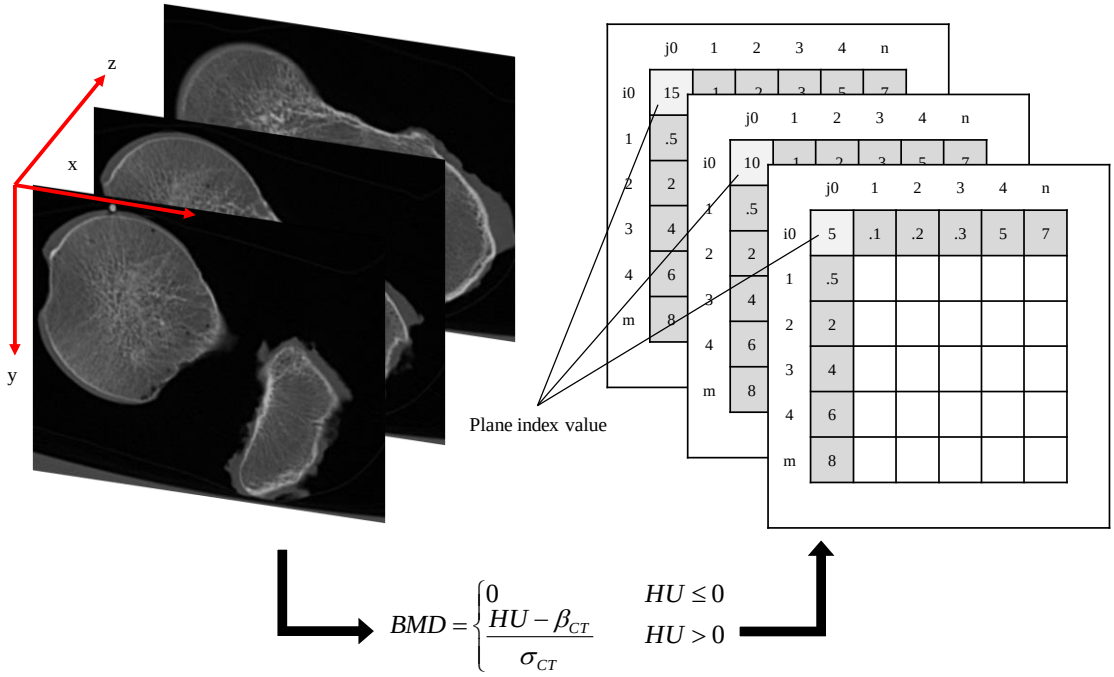

Fig. 5-8. ANSYS Table array paramenter definition. The CT images are saved as an array and arranged in "planes". In the same process, the voxel values are converted from the original HU into the CT specific bone mineral density (BMD) (5.2.1).

Since the files created with the Matlab function has the appropriate format, an internal routine was written in Ansys in order to read such files saving the data in an internal table array parameter. In the same routine, the table array parameter was defined as a

temperature field and thus the BMD was considered at this point as a "pseudo-temperature". Finally, the bone density assignment was performed "by node" (Appendix D). The elastic properties of each element were automatically calculated by the node *temperatures* and the material properties relationships below (Fig. 5-9).

This procedure presented some advantages, for instance the lower computation time for the material properties assignment. In contrast with other methods, which use third-party programs for such purpose, the calculation is internally performed saving a considerable amount of access time. On the other hand, this method may require more memory in order to save the information of the CT images in a very large array. For that reason, the CT data for all models were resized and homogenized to an average resolution of 0.3x0.3x1.2 mm. This image operation was also carried out by ImageJ using a bicubic interpolation for downsizing.

The elastic material constants (i.e. E modulus for isotropic model and E_{axial}, $E_{transversal}$ and shear modulus for the orthotropic model) were defined as a function of temperature, i.e. the BMD. The relationship between elastic modulus and BMD for trabecular bone was obtained using the experimental data of Chapter 4.3, from where an isotropic as well as an orthotropic material models were established (Fig. 5-9). For comparison, an additional isotropic material model was considered from the literature (Keyak, et al., 2003; Yosibash, et al., 2007). In the same way, the correlations for cortical bone as well as the Poisson's ratio ($\nu = 0.3$) (Peng, et al., 2006; Yosibash, et al., 2007) were also taken from the literature. All material properties relationships are presented in Table 5-3 (Fig. 5-9).

In some cases of the literature, the elastic modulus is reported as function of ash density (ρ_{ash}) or apparent density (ρ_{app}), whose relationships are also included in Table 5-3.

Similar criterion, to those from the literature, was used to distinguish between the cortical and trabecular bone. In Keyak, et al. (2003) the trabecular bone was associated with $\rho_{ash} < 0.6$ and in Yosibash et al. (2007) the cortical bone was associated with HU > 700 and trabecular bone with HU $\leq$ 700. In the present study, the trabecular bone was associated to BMD $\leq$ 500 and the cortical bone with BMD > 500. According to the CT calibration curves, this proposed criterion matches almost exactly with the latter (Yosibash, et al., 2007).

Table 5-3. Summary of the material properties relationships

Conn. Name	Properties relationships	Ref.
Isotropic	$E_{trab}(\rho_{BMD}) = 7607\rho_{BMD}^{1.853}$	Present study
	$E_{Cort}(\rho_{ash}) = 10200\rho_{ash}^{2.01}$	(Keller, 1994)
	$\nu = 0.3$	(Keyak, et al., 1993; Yosibash, et al., 2007)
Orthotropic	$E_{trab}^{axial}(\rho_{BMD}) = 12241\rho_{BMD}^{2.058} (= E_x)$	Present study
	$E_{trab}^{trans}(\rho_{BMD}) = 5275\rho_{BMD}^{1.70} (= E_y = E_z)$	Present study
	$E_{cort}^{axial}(\rho_{app}) = 2065\rho_{app}^{3.09}$	(Wirtz, et al., 2000)
	$E_{cort}^{trans}(\rho_{app}) = 2314\rho_{app}^{1.57}$	(Wirtz, et al., 2000)
	$\nu_{yz} = 0.25;\ \nu_{xy\|zx} = 0.33$	(Yoon, et al., 2008; Trabelsi, et al., 2011)
	$G_{yz} = \frac{E_{y\|z}}{2(1+\nu_{yz})}; G_{xy\|zx} = \frac{E_{mean}}{2(1+\nu_{xy\|zx})}$	Transverse isotropy
Keyak	$E_{\text{trab}} = 33900(\rho_{ash})^{2.20};\ \rho_{ash} \leq 0.27$	(Keyak, et al., 2003)
	$E_{trans} = 5307\,\rho_{ash} + 469;\ ;\ 0.27 < \rho_{ash} < 0.6$	(Keyak, et al., 2003)
	$E_{cort} = 10200(\rho_{ash})^{2.01};\ \rho_{ash} \geq 0.6$	(Keller, 1994; Keyak, et al., 2003)
Ash density	$\rho_{ash} = 1.22\rho_{QCT} + 0.0526$	(Keyak, et al., 2003)
Apparent density	$\rho_{app} = 2/1500$ HU	(Peng, et al., 2006)

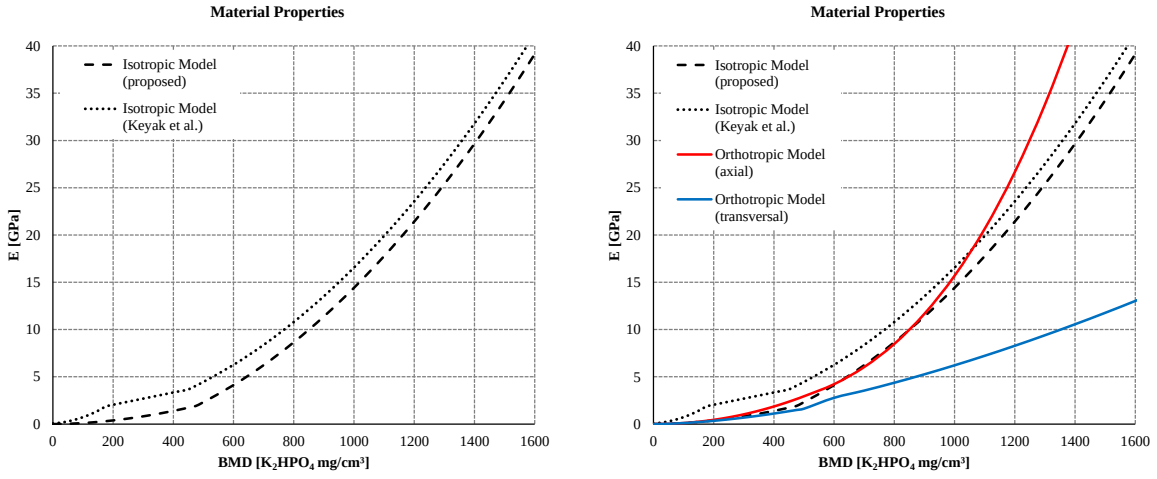

Fig. 5-9. Material properties relationships. Left, comparison of the isotropic models; right, comparison of the isotropic and orthotropic models.

Orthotropic material directions assignment

According to Wolff's Law, there is a remarkable similarity between the trabecular architecture of proximal femur and the stress trajectories. Therefore, the following method based on the stress field was proposed in order to assign the material directions.

From the isotropic models simulations, the stress field was recorded and the principal stresses were computed. Thereafter, the principal stresses were arranged according to their absolute value. Hence, the direction of the highest value was defined as the main material direction and noted as the X-direction according to Ansys notation convention. The other two directions were considered orthogonal (E_y and E_z, in Ansys notation convention) (Fig. 5-10). Three different load orientations (0°, 7° and 15°) were considered for the generation of the material principal directions enabling the definition of three orthotropic models, one for each load orientation.

Then the orthotropic model was included in the simulation and the coordinate system of each element was aligned with the defined material principal directions.

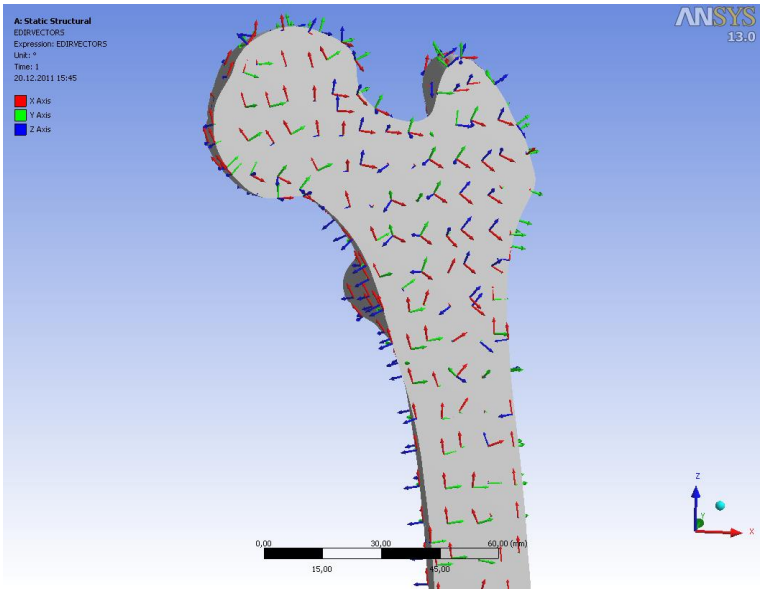

Fig. 5-10. Assignment of the material directions extracted from the stress field of the isotropic model simulations. The X-direction is considered to be the axial or main direction of the orthotropic model.

The mesh remained unchanged between the isotropic and orthotropic simulations because the element numeration was used for the directions extraction and assignment. These functionalities were programmed in APDL modules on the Ansys Workbench (Appendix D)

5.2.6 Load and constraint definition

The loads and constraints of the numerical models were defined to reproduce the loading experiments in Chapter 3.2. The distal face of the bone was fixed at the location where it resided in the polyurethane resin, and a pressure load with a resultant of 1000 N was applied on a simplified circular area over the femur's head. The exact direction and position of the load was defined by means of the Microscribe and the coordinate transformation procedure explained in 5.2.1. No additional movement restriction was defined on the femur's head reproducing so, the same conditions of the experimental setup (Fig. 3-7, Fig. 3-8).

5.3 Results

The bone mineral distribution was evaluated from the nodes of the FE models. Since the elastic properties were related to the BMD, this parameter had a major influence on the models. After a preliminary visual inspection of the BMD representation, the two types of bone could be distinguished (Fig. 5-11). Moreover, the BMD on the boundary was examined at the sites were the strain were measured, corresponding to the strain gage locations. An inexact geometry representation could lead to an underestimation of the BMD and thus of the elastic properties, thereby distorting the strain measurements.

Two regions could be clearly observed in the histograms corresponding to the different bone tissues, i.e. trabecular and cortical bone. It has to be noted that the minimal bone density of the models corresponding to zero was, in this way, defined in the material properties assignment procedure (Fig. 5-8). In the original CT images, the presence of fat and air bubbles reported negative attenuation values in HU, which in turns would have reported negative bone mineral density values. Values of bone mineral density close or equal to zero represented the empty regions of the bone filled with water, bone fluids and bone marrow among others.

Due to the non-Gaussian distribution of the mineral density, an ANOVA test is not applicable to the data. In this case, a nonparametric statistical test, such as Kruskal-Wallis test, should be performed to assess whether the bone mineral distribution of the specimens statistically differ or not. However, this test requires a large amount of computing resources, and because of the large sample size (~400,000) make this comparison unfeasible. The most common statistical measures are also presented in Table 5-4.

(a) (b)

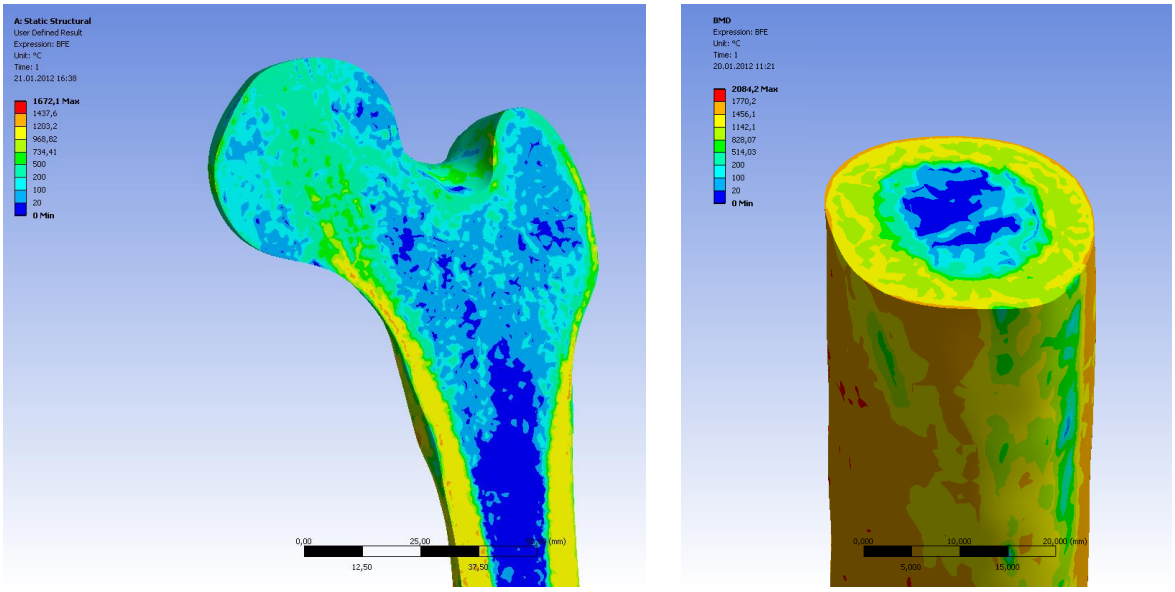

Fig. 5-11. BMD representation of the bone models. Dark blue regions represent the bone fluids and no contribution to the bone stiffness. Yellow regions represent the cortical bone. Light blue regions represent the trabecular bone. Finally, green regions represent the transition between trabecular and cortical bone. (a) Proximal femur, (b) bone shaft. It has to be noted that the parameter Temperature corresponds to bone mineral density [K_2HPO_4 mg/cm^3].

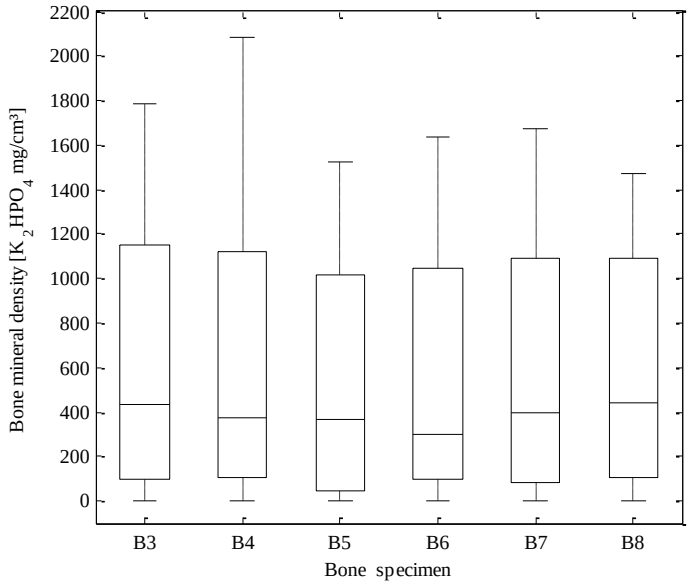

Fig. 5-12. Box and whisker plot of the BMD of the specimens.

Table 5-4. Statistical measures of the specimens' bone mineral density.

Specimen	Bone mineral density [K_2HPO_4 mg/cm³]	
	Mean	Standard deviation
B3	602	511
B4	596	543
B5	506	460
B6	511	463
B7	566	486
B8	572	473

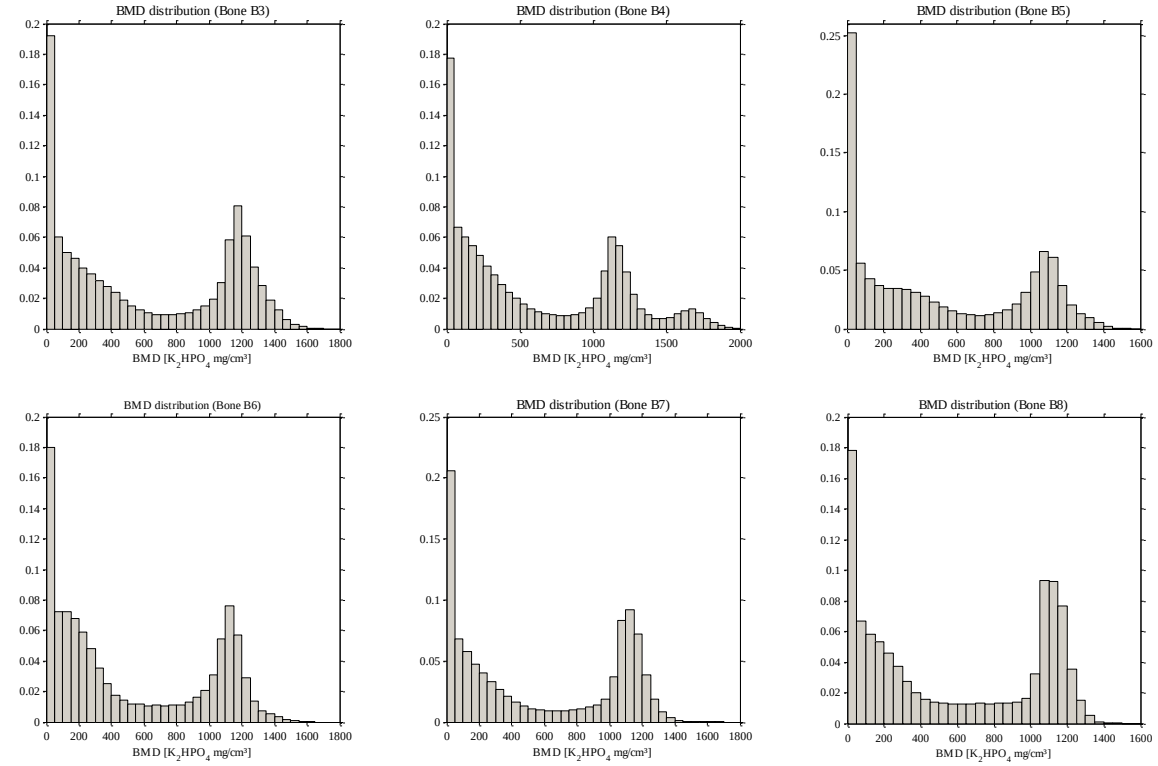

Fig. 5-13. Distribution histogram of the bone mineral density taken from the nodes values of the FE models. The distribution presented two distinguished regions corresponding to the trabecular and cortical bone tissue.

A large number of experimental observations (n = 136, for the complete dataset of six bones and n = 83, for the three modelling bones) were compared with the corresponding results of the FE models.

Therefore, there were a very large analysis combination regarding the experimental groups (modelling, control, all), the measures (strain, displacement, all) and the material models (two isotropic models, and 3 orthotropic models). Because of that, the most relevant results are presented in separate graphs below and, at the end of the section a summary of all data was also included (Table 5-5, Table 5-6, Table 5-7).

First of all, only the data from the three modelling bones (Fig. 5-14a) and of the control bones (Fig. 5-14b) were independently compared. Then, all data together were also introduced in the comparison. The latter were separately represented by strains and displacements.

The isotropic-FEA of the modelling group correlated with the experiments by (R^2 = 0.957, slope 1.099). In the same way, the predictions for the control group of bones correlated by (= 0.908, slope 0.938). The complete dataset correlated by (R^2 = 0.933, slope 1.035). The strains presented higher correlation with the experiments (R^2 = 1.041, slope 0.93) than the displacements (R^2 = 0.823, slope 0.94). This behavior was observed for every analysis combination.

The experimental observations were also compared with the FE models generated using the correlations from literature (Keyak et al.). In this case, the FEA for all measurements correlated by (R^2= 0.926, slope 0.871) and by (R^2 = 0.842, slope 0.96) for displacements. The material model used in (Keyak, et al., 2003) created stiffer prediction models, as the slope of the data regression showed. However, the predictions presented high coefficients of determination, meaning that the FEA models behaved like the experimental specimens but the elastic response presented a proportional overestimation in stiffness.

Finally, the results from the orthotropic models were correlated as well with the experimental observations. As mentioned above, three orthotropic models were generated corresponding to the three different material direction definitions.

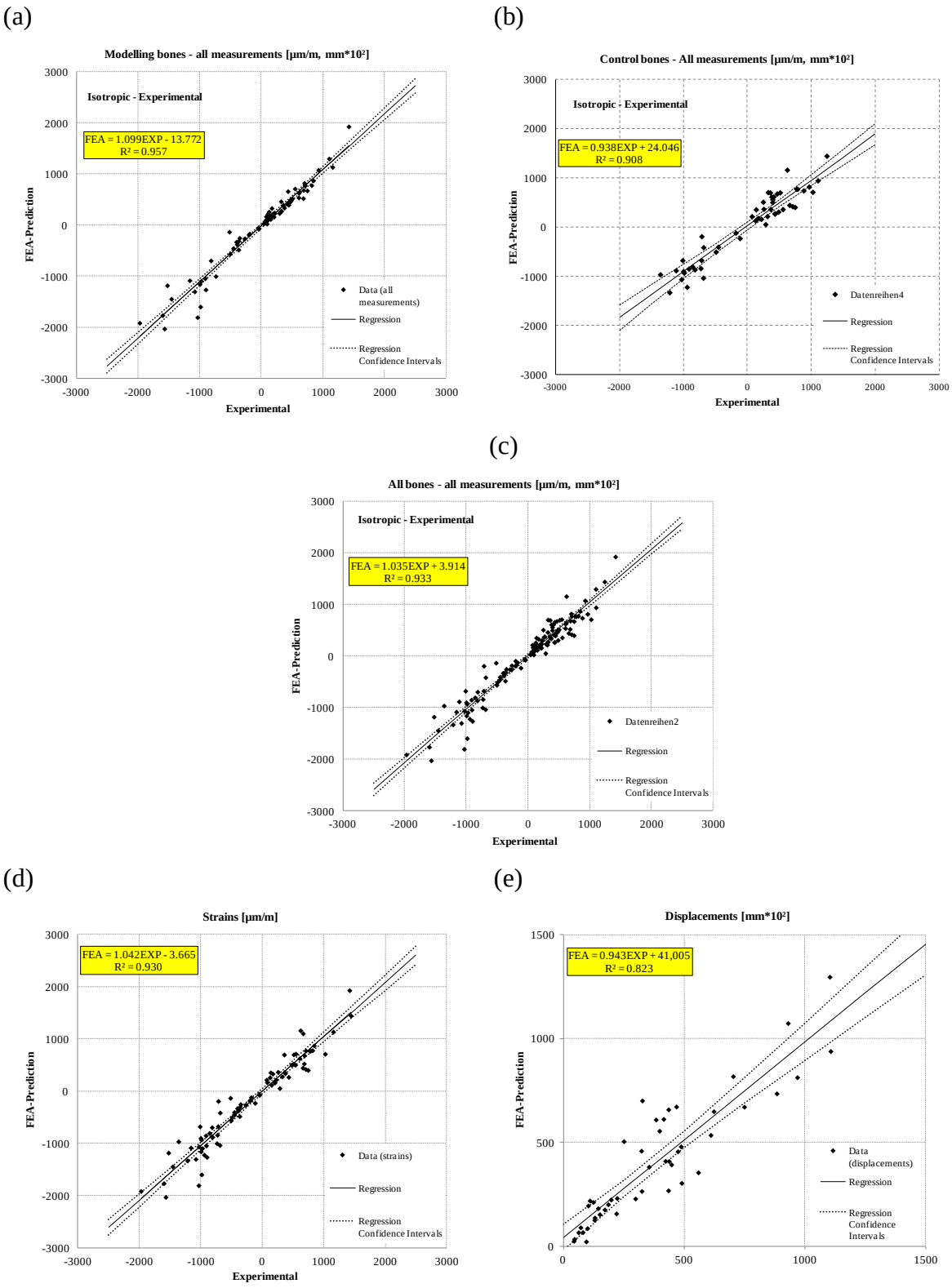

Fig. 5-14. Regressions of the isotropic model (current study): (a) Modelling group of bones (n = 3), all measurements (n = 83): FEA versus experimental observations, (b) control group of bones (n = 3), all measurements (n = 53): FEA versus experimental observations, (c) all bones (n = 6), all measurements (n = 136): FEA versus experimental observations, (d) all bones (n = 6): FEA strains versus experimental observations, (e) all bones (n = 6): FEA displacements x100 versus experimental observations.

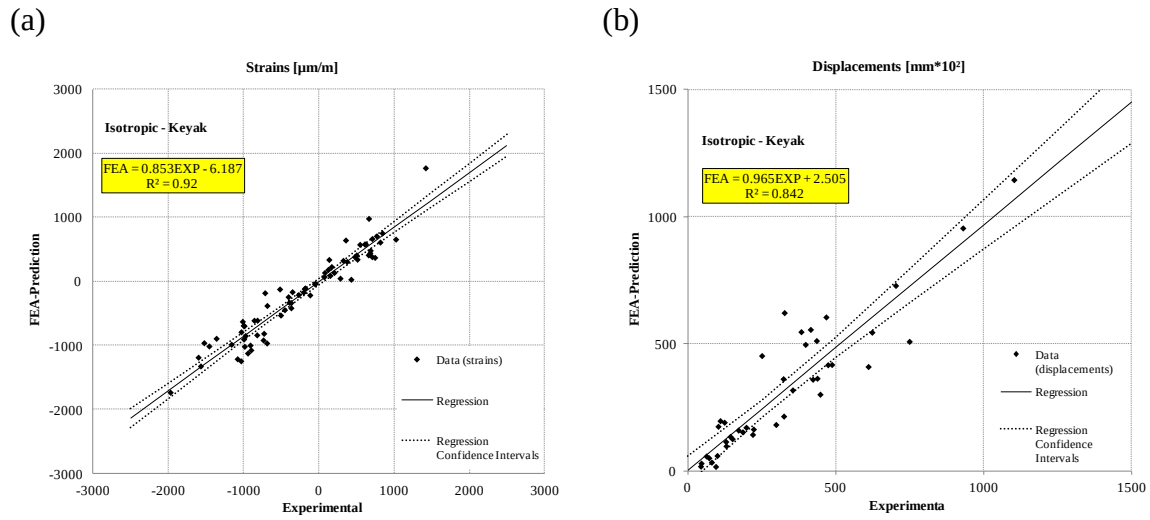

Fig. 5-15. Reference model with Keyak's material relationships: (a) Isotropic model (all bones): FEA all measurements versus experimental observation, (b) Isotropic model (all bones): FEA displacements versus experimental observations.

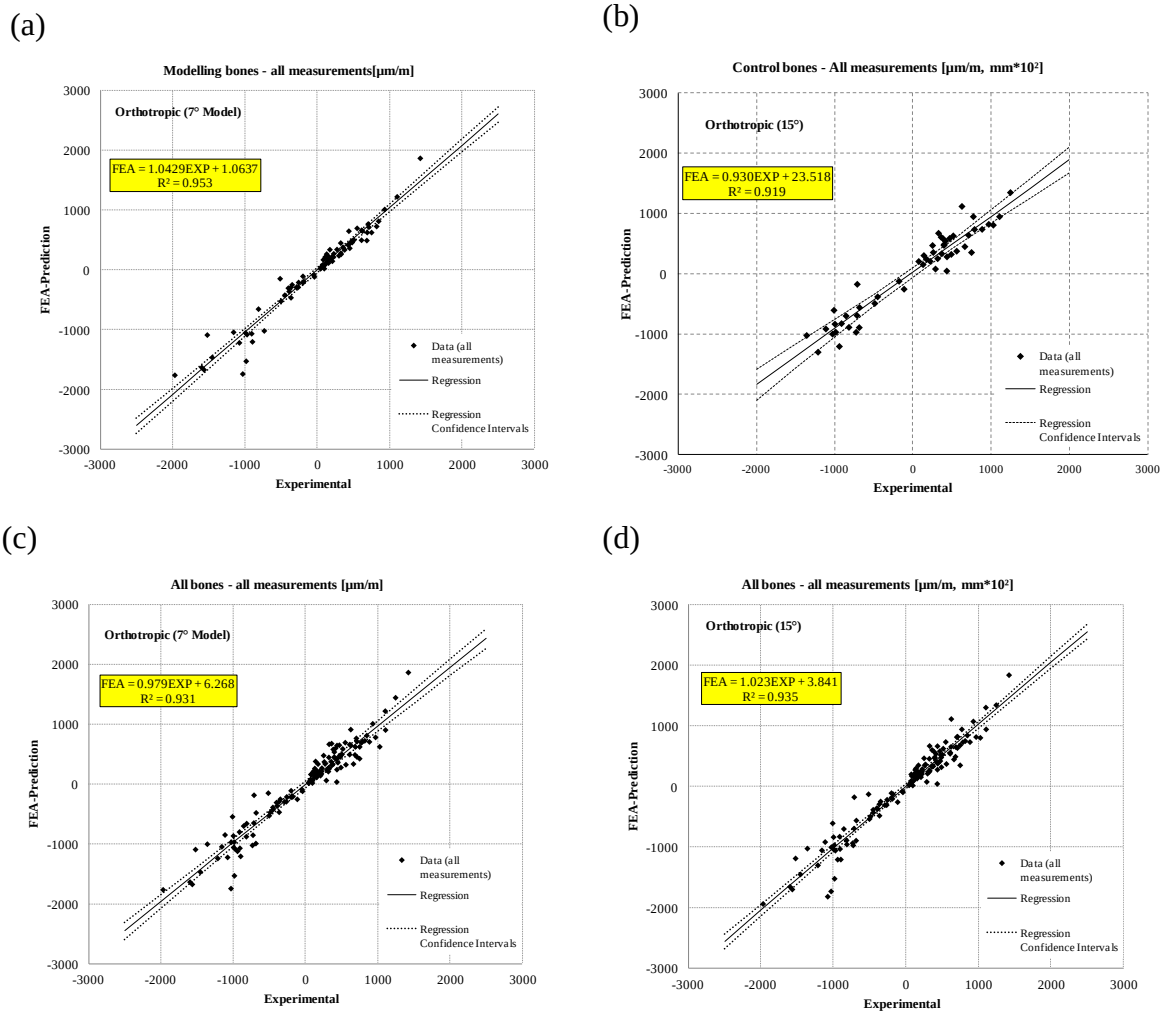

Fig. 5-16. Regressions of the orthotropic models: (a) modelling group of bones (n = 3), all measurements (n = 83): FEA versus experimental observations, (b) all bones (n = 6), all measurements (n = 136): FEA versus experimental observations, (c) all bones (n = 6): FEA strains versus experimental observations, (d) all bones (n = 6): FEA displacements x100 versus experimental observations.

Table 5-5. Summary of the data for all bones (n = 6).

Model	Material	Data	R^2	Slope
Isotropic	Present study (trab)	All	0.933	1.035
		Strains	0.93	1.041
		Displacements	0.823	0.943
	Keyak et al.	All	0.926	0.871
		Strains	0.920	0.853
		Displacements	0.842	0.965
Orthotropic	Directions 0°	All	0.930	0.971
		Strains	0.922	0.974
		Displacements	0.836	0.878
	Directions 7°	All	0.931	0.979
		Strains	0.924	0.978
		Displacements	0.819	0.897
	Directions 15°	All	0.935	1.023
		Strains	0.928	1.027
		Displacements	0.848	0.942

Table 5-6. Summary of the data for modeling bones (n = 3).

Model	Material	Data	R^2	Slope
Isotropic	Present study (trab)	All	0.957	1.099
		Strains	0.947	1.110
		Displacements	0.941	1.083
Orthotropic	Directions 0°	All	0.952	1.037
		Strains	0.943	1.043
		Displacements	0.940	1.015
	Directions 7°	All	0.953	1.043
		Strains	0.944	1.046
		Displacements	0.939	1.032
	Directions 15°	All	0.953	1.088
		Strains	0.944	1.092
		Displacements	0.938	1.088

Table 5-7. Summary of the data for the control bones (n = 3).

Model	Material	Data	R^2	Slope
Isotropic	Present study (trab)	All	0.908	0.938
		Strains	0.909	0.943
		Displacements	0.565	0.661
Orthotropic	Directions 0°	All	0.907	0.878
		Strains	0.904	0.878
		Displacements	0.61	0.608
	Directions 7°	All	0.906	0.888
		Strains	0.906	0.884
		Displacements	0.554	0.622
	Directions 15°	All	0.919	0.93
		Strains	0.916	0.936
		Displacements	0.661	0.656

5.4 Discussion

The aim of the current study was to create an experimental-specific model of the human femur to be used in FE analyses. In Chapter 3, a total of six fresh frozen human femora were mechanically tested. From three of them, several cubical trabecular specimens were harvested and orthogonally tested enabling to obtain some relationships between the elastic properties and the bone mineral density (Chapter 4). An isotropic as well as orthotropic model were derived from the experimental data and introduced in FE models. Subsequently, the predictions from the FEA were compared and correlated with the experimental observations of the complete femora.

The elastic properties of the trabecular bone were assessed from the mechanical and orthogonal tests of several specimens of bones, which were previously macroscopically tested. The elastic moduli were directly correlated with the equivalent bone mineral density (QCT density). No intermediate density relationship was considered to minimize the propagation of numerical errors.

FE simulations present some limitations from the point of view of the idealization and discretization. The geometry of the FE models depends on the resolution of the CT and the segmentation procedure. In the same manner, the bone density distribution assigned to the FE models depends on both the CT data, where it was determined, and the geometric representation. In sites with high curvature, the smooth surface approximation may lead to an underestimation of the bone mineral density on the surface, which may affect the local strains but not the global displacement. This aspect was taken into consideration for the post-processing analysis evaluating the bone mineral distribution at the locations of the strain gages.

The bone density assignment may also introduce some inaccuracies due to the averaging method. This property was assigned by node to the FE model. Afterwards, the elastic properties were evaluated for each quadratic tetrahedral element from the nodes values, making these material models mesh-dependent. However, in this study the mesh refinement was chosen regarding the CT resolution, so that the average node separation was similar to the voxel average size.

No separation between cortical and trabecular bone was considered in the models. In the one hand, the mineral density histograms of the bone models showed a obvious separation between the two kinds of bone tissues. The chosen criterion used for the elastic property assignment was seen to be consistent with these density histograms. On the other hand, a separation of the bone into two regions may present some advantages of an independent elastic property definition but it also may represent a source of errors because inaccuracies and discontinuities of the interface between regions (Yosibash, et al., 2007).

The results from the FE simulations have shown that:

The empirical relationships for trabecular bone obtained in this study and empirical relationships for cortical bone from the literature (Keller, 1994; Wirtz, et al., 2000) in conjunction with the FE model produced good predictions of the mechanical response of the bone described by strains and displacements for all load conditions. In the same

manner, the use of orthotropic models may provide interesting information about the probable material principal directions of the bone. In principle, the orthotropic models presented better prediction values than those of the isotropic model. However, small differences were found between the results of the material models for the modeling group of bones. For all bones and measurements, the directions corresponding to the isotropic loading at 15° showed the highest correlation and prediction values between all the models considered. The small differences between the isotropic and orthotropic models may be originated by the loading cases considered. These loading might not differ substantially from the mechanical physiology of the bone. In this respect, the authors of this study considered worthwhile to investigate the differences between the models for non-physiological load cases, e.g. during a fall to the side.

The predictions between the FEA and the experimental observations are in agreement with other studies in the literature (Yosibash, et al., 2007; Trabelsi, et al., 2011). In the latter, a large dataset of twelve bones were tested at a stance position reporting a good correlation and prediction by (R^2 = 0.93, slope 1.009).

In all cases, the modeling group of bones provided the better FE predictions than the control group of bones, which is logical, since the material property relationships were obtained from these specific bones. Nevertheless, correlation coefficients of 0.9 and higher were found for the regressions of the control group. On the one hand, the modeling group enabled a more comprehensive evaluation of the FE models from the numerical point of view. Thus, optimizing FE models may be more precisely carried out from the evaluation of model-specific FEA, which include the individual material properties.

To conclude, double level experimental procedure, not yet considered in the past –to the best of the authors' knowledge-, was used in this study for constructing specific finite element models. Hence, specific trabecular bone property relationships were empirically obtained from the same bones which were previously tested. In conjunction with a proposed FE modelling method, the results present a remarkable agreement between the analyses and the experiments. Moreover, the FE modelling procedure was kept as simple as possible, having in mind future clinical application requirements.

6 Finite Element Analysis of the Trabecular Specimens

6.1 Introduction

In the previous chapter, the proposed models of the complete femora explained with a high level of confidence the macroscopic mechanical behavior observed in the mechanical experiments. These models were based on QCT data in conjunction with the FE method enhanced with inhomogeneous material properties as a function of the BMD.

Commonly, the study of bone specimens at the meso level includes some techniques as micro CT. The resolution of this technique (10-30 μm) is higher than the CT scanners for clinical applications and enables the reconstruction of the trabecular structure with homogenous isotropic density-based properties (Chevalier, et al., 2007; Renders, et al., 2008). However, as it was mentioned in previous sections, this technique presents some disadvantages such as the size of the specimen and the high x-ray dose, which may make this technique not suitable for in-vivo experiments. Moreover, FE analyses based on complex micro-CT data require a high computation effort. For example, the computation of the heads of two femora (Verhulp, et al., 2008) needed more than 5 weeks of many processors of a supercomputer. Since the long-term purpose of this study is to predict the mechanical response of patient bones, the latter technique should be, in principle, dismissed.

Hence, the scope of the continuum-level voxel models was evaluated in this section by means of the experimental data from the trabecular bone specimens (Chapter 4) and numerical simulations from the QCT data of the specimens. Same inhomogeneous material relationships from the previous chapter were also considered, namely isotropic model as well as orthotropic model.

6.2 Method

The generation of the FE models of the trabecular specimens was similar to that for the complete femora. This included the scanning and segmentation of the CT images of the specimens, the material properties as well as the load and constraints definition (Fig. 6-1). However, these models presented some specific features. In first place, the segmentation should be manually performed, since the specimens were completely trabecular and there were any boundary, which marked out the specimen's geometry. The cubical geometry of the specimens was then defined by its 8 vertexes, taken from the cropped CT dataset of each specimen. The coordinates of the vertexes were directly used to create a simplified CAD model of every cubical specimen. As it was done in the previous chapter, from the CT data of each specimen, a text file was generated with MATLAB containing the equivalent bone mineral density and coordinates of the voxels (5.2.3). These material files were also imported into the FE-software in order to assign the corresponding material properties, i.e. elastic modulus.

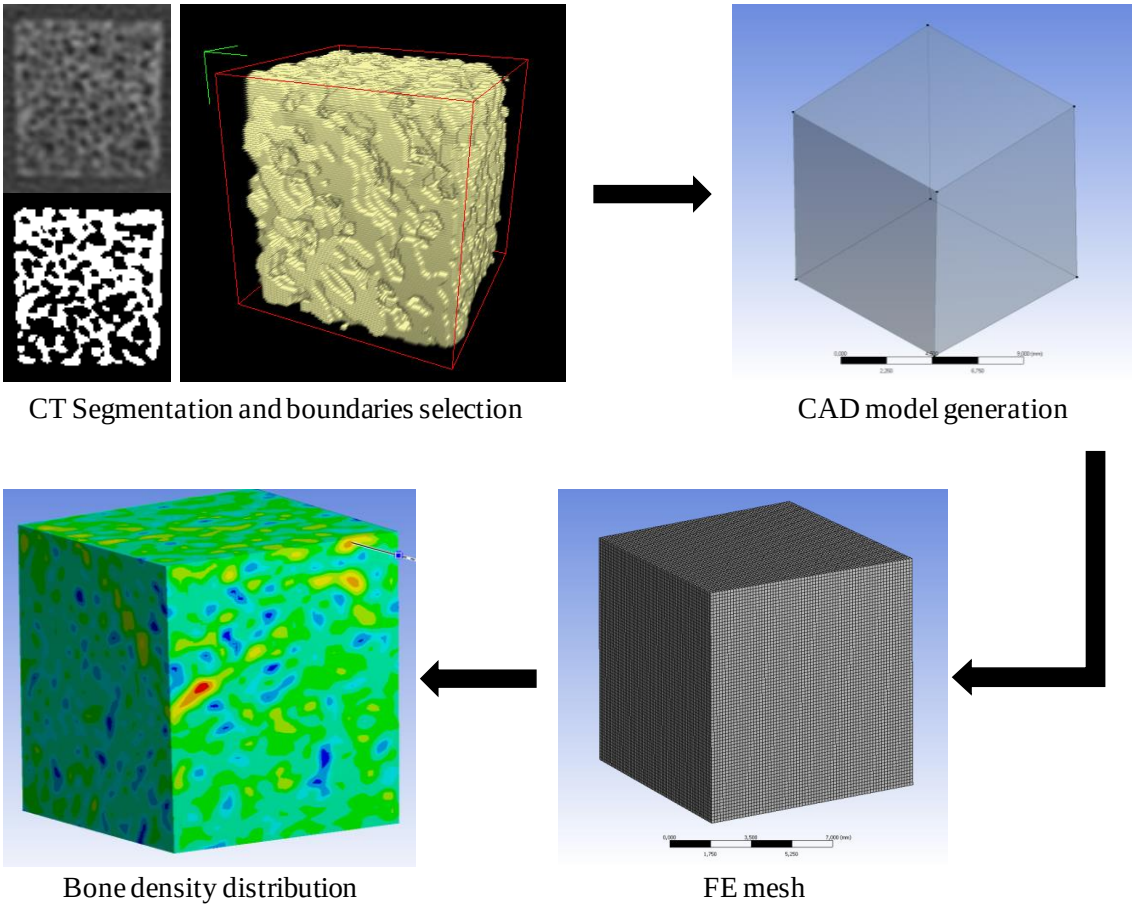

Fig. 6-1. Exemplary representation of a specimen's CT image. Left to right: original CT image, color representation and exemplary segmentation.

The second specific feature of the cubical specimen analysis was the definition of the principal material directions necessary in order to assign the orthotropic elastic properties. In this case, an image analysis of the specimen CT data was carried out to estimate the material directions. In contrast to the orthotropic models of the complete bone, whose

material directions were represented as a spatial function over the whole model geometry, the material directions for orthotropic models of the cubical specimens were considered to be constant within their whole geometry. The complete procedure is presented in the following sections.

6.2.1 Segmentation and generation of FE models

The CT images of the cubes could not be segmented using the same procedure for the femora. The reason was that the cubes comprised only trabecular bone. Thus, there was no cortical shell which defined the boundary of the geometry to be analyzed.

Therefore, the geometry of the cubical specimens had to be directly extracted from the CT images taking the position of their vertexes. Simple, not regular cubes were modeled in the CAD module of Ansys. Slight machining inaccuracies of the cubical specimens as well as the CT resolution leaded to smaller dimensions of the CAD models. However, this geometrical feature was desirable, since larger specimen dimensions would have caused an underestimation of the bone density at the boundary and consequently of the mechanical response of the whole FE model.

6.2.2 Mesh generation

The simple geometry of the specimen models enabled to use 3D 8-node hexahedrons. The size of the elements was chosen regarding the resolution of the original CT data of each specimen.

Since the elastic properties were mesh-dependent and the maximal refinement based on the CT data was feasible, it was considered that the selected mesh was considered as sufficiently accurate.

6.2.3 Image anisotropy analysis

As it was mentioned in the Chapter 4.2.1, the CT imaging of the cubical specimens was performed using a High Advanced Scanner (Philips) with an average voxel resolution of 100 x 100 x 300 μm.

The material directions can be estimated from the morphology parameter "fabric tensor". This consists of a second-rank tensor in the form of a 3x3 matrix and provides compact description of the orthotropic architectural anisotropy (Matsuura, et al., 2008). The most common imaging method for the computation of the fabric tensor is the mean intercept length (MIL), which consists first in evaluating, using a straight line, the amount of intercept with bone-marrow interface for a given orientation "n" and second in normalizing the resulting number by the length of the line. Therefore, the original CT image has to be converted to binary in order to determine the intercepts. The fabric tensor can be graphically represented as a 3D polar plot (Fig. 6-2). Because of this, it is also commonly referred to as fabric ellipsoid. The eigenvectors of the fabric tensor define the main directions, and the eigenvalues give the degree of concentration around the main directions.

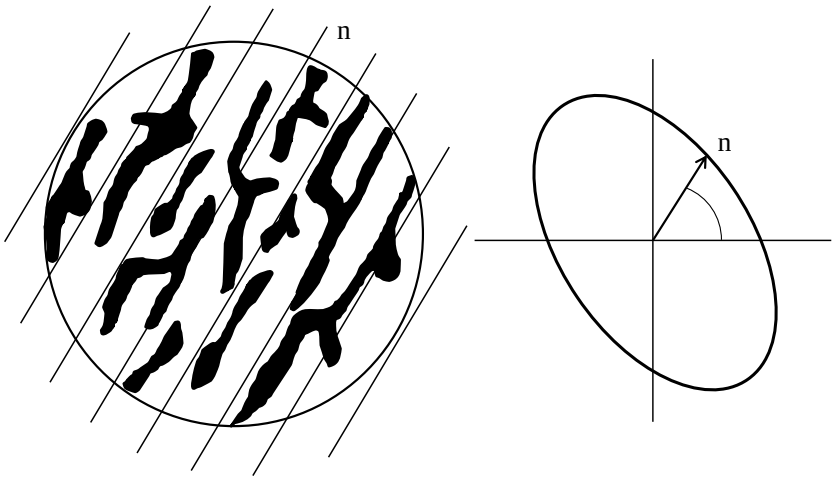

Fig. 6-2. Method of the mean intercept length and its two-dimensional polar representation (adapted from Zysset, 1994).

In contrast with other studies, the fabric tensor was assessed in the present study in order to estimate only the material directions, which were used with the orthotropic model proposed in the previous section.

The whole image analysis approach was performed using the ImageJ and its plugin, BoneJ (Doube, et al., 2010). For the analysis, a region of interest (8 x 8 x 8 mm^3) of each specimen was taken from the CT images. The cropped CT images were resized to obtain isotropic voxel geometry. Next, the CT images were segmented into binary images by thresholding consisting of only a trabecular bone phase and a marrow equivalent phase. Similar threshold criterion was taken into account for the CT image data included in the analysis.

Once the CT images were segmented the application "Trabeculae-Anisotropy" of the plugin BoneJ could be applied. This application generates a copy of input CT data aligned to its fabric tensor and provides the rotation matrix involved in this operation. The principal directions of the fabric tensor could be derived from this rotation matrix and then introduced into the FE model of the correspondent cubical specimen. The principal direction corresponding to the axial material direction was those with the largest MIL numerically and, graphically with the longest axis of the fabric ellipsoid.

Since the numerical implementation for calculating the fabric tensor is neither a trivial task (PhD. Theses: (Zysset, 1994; Wald, 2010)) nor the aim of the present study, the aforementioned application was taken into consideration for such purposes. The output results of the application were visually and subjectively evaluated using binary image stacks specifically created for that reason. In the same manner, the principal direction provided by the application was also graphically superimposed over the CT images of the bone specimens for a preliminary visual validation (Fig. 6-3).

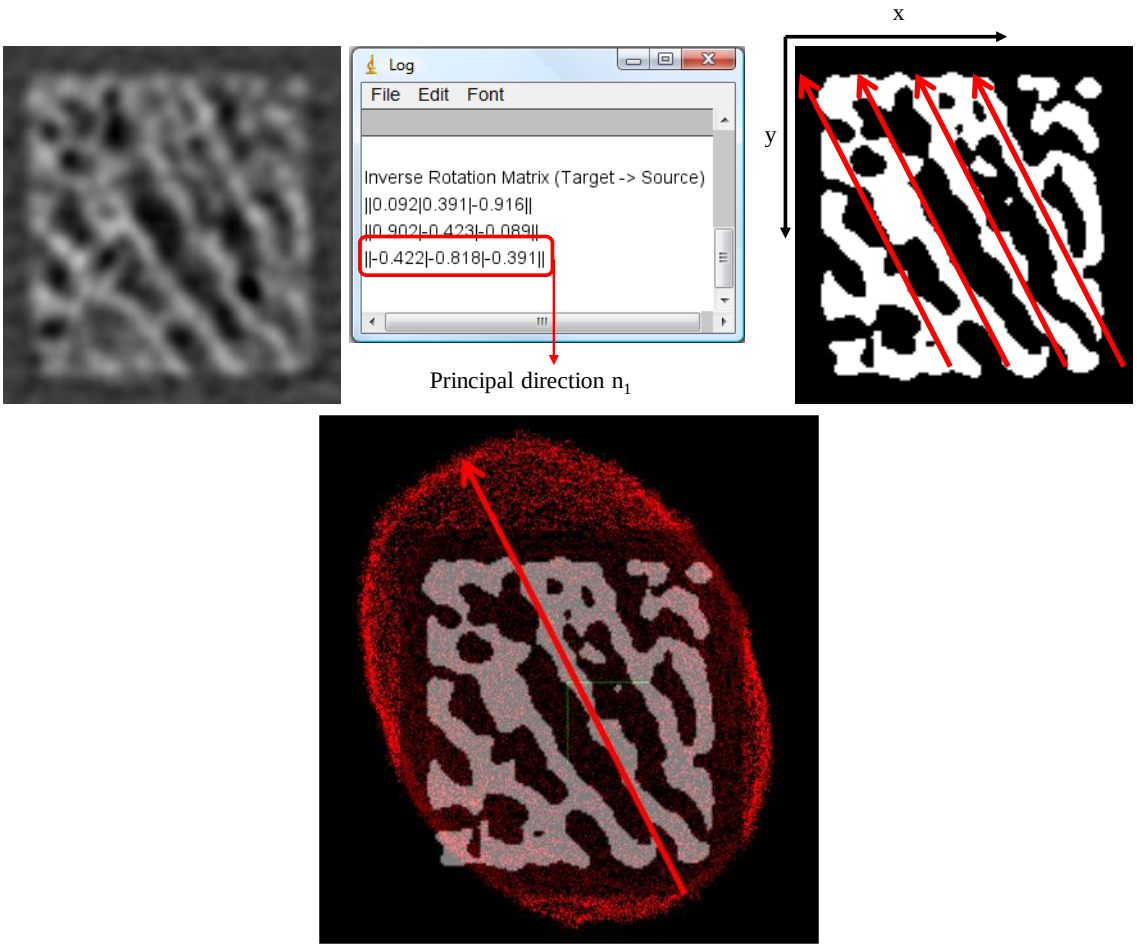

Fig. 6-3. Evaluation of the image application BoneJ-Anisotropy.

A local coordinate system was created in Ansys according to the principal directions of the fabric tensor. The first principal direction was defined as the axial material direction and aligned with the X-direction according to the Ansys notation. The transversal material directions were defined from the two other orthogonal principal directions from the fabric tensor analysis.

6.2.4 Material properties assignment

Same material property relationships as in section 5.2.5 were considered for FE analysis of the cubical specimens (Fig. 5-9). Likewise, the assignment was carried out following the same procedure. Hence, the CT images were converted to a test file to be imported as a "Table Array" into Ansys.

The bone density was assigned by node as a body temperature distribution. The elastic modulus was then internally interpolated for each element from its node temperature values and the material property relationships aforementioned.

The Poisson's ratio was assumed to be constant for the isotropic model ($\nu = 0.3$) having the same value as it was used for the bone models of the previous chapter (Keyak, et al., 2003; Yosibash, et al., 2007).

6.2.5 Load and constraint definition

The mechanical tests of the trabecular specimens were performed, as it was mentioned in section 4.2, using two polished steel plates in wet conditions (Fig. 6-4).

In order to quantify how much the contact for the pairing bone-steel influenced the simulations, several cases were evaluated for different boundary conditions (i.e. loads and constraints). The methods and results of this analysis were included in Appendix C.

The presence of friction leads to an overestimation of the elastic modulus. Several authors have estimated this overestimation to about 5% (Linde, et al., 1989; Odgaard, et al., 1991). Similar magnitude of overestimation was obtained in the present study (Appendix C). The contact between specimen and compression platens was modeled for coefficient of friction of 0.2, 0.3, 0.5 as well as a frictionless contact, which was used as reference. The difference in apparent modulus of the specimen with lower density (mean BMD = 269 mg/cm³) was found to be 5.73%, 6.33% and 7.54%, respectively. The specimen with higher density (mean BMD = 356 mg/cm³) presented a difference in apparent modulus of 2.55%, 3.18% and 3.95%, respectively.

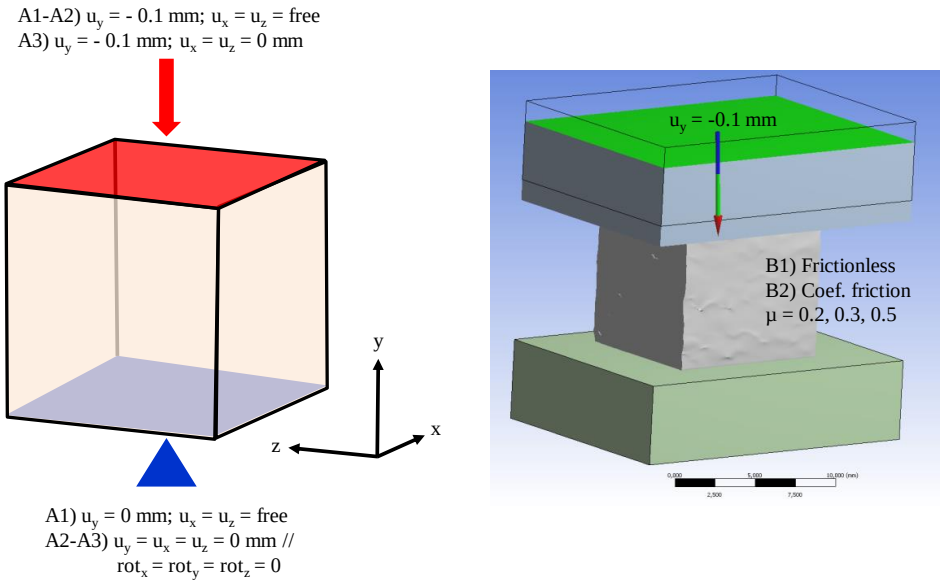

Fig. 6-4. Proposed boundary conditions for the evaluation of the influence of the boundary definition. The Case A (left) represents a simplified contact model and in Case B (right) the steel platens are included into the model.

Simplified models without steel platens were also generated and introduced in the analysis. The highest difference between the proposed models was found for the fully constrained specimen up to 11.75% and 7.49%, respectively for the specimen with low and high density.

Moreover, an slight overestimation was found between the simplified frictionless model without compression platens and the complex model with them to be 5.63% and 3.43%, for the specimen with low and high density. The results for the simplified frictionless model were comparable with the results of the complex models with a coefficient of friction ranged 0.2-0.3. The computational time for the simplified model

analyses was about 30 minutes and considerably shorter than for the complex friction analyses that required over 4 hours of computation.

Therefore, in view of all these results, it was considered that the simplified frictionless model may reproduce with suitable accuracy low friction contacts between the specimen and the compression platens with an additional advantage of reducing considerably the computation time.

6.3 Results

The BMD distributions of the cubical trabecular specimens were evaluated from the nodes of the FE models. In contrast to the BMD distribution obtained for the complete bones, the distributions for the trabecular specimens presented only one normally distributed region, revealing no presence of cortical bone. However it was reported the presence of voxels within the specimens with very high BMD values over 1000 mg/cm³ (Fig. 6-5, Fig. 6-6). Actually, at the microscopic level the single trabeculae show similar mechanical properties and density to those of the cortical bone (Chevalier, et al., 2007; Hamed, et al., 2010).

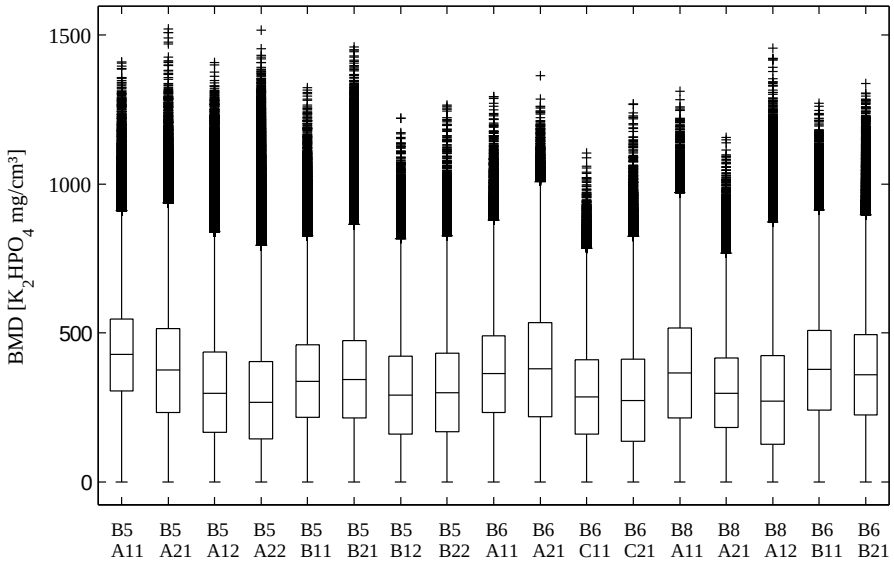

Fig. 6-5. Distribution of the bone density.

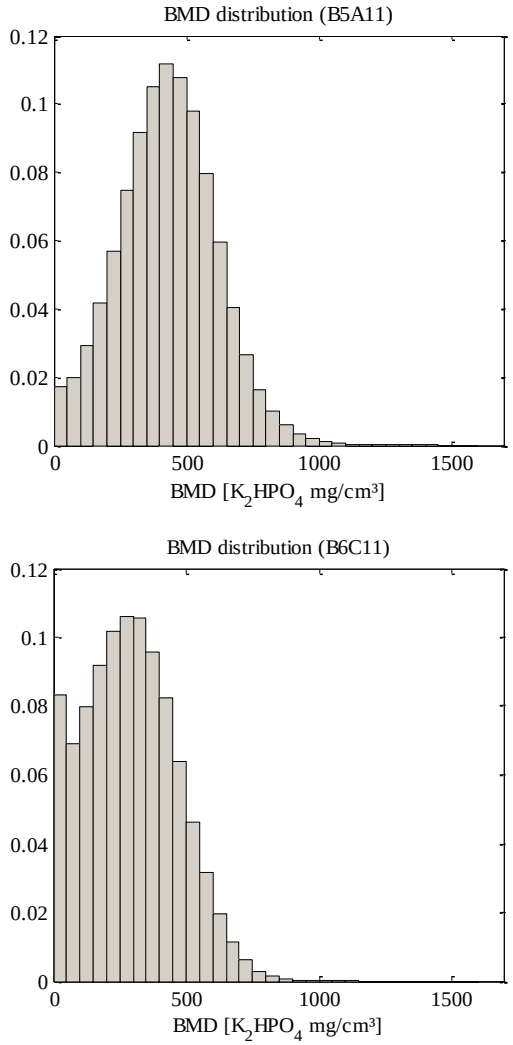

Fig. 6-6. Exemplary BMD distributions of the trabecular specimens.

Table 6-1. Summary of the BMD statistical measures of the trabecular bone specimens.

Specimen	Bone mineral density [K_2HPO_4 mg/cm³] Mean	Standard deviation(1)
B5 A11	431	182
B5 A21	374	202
B5 A12	313	206
B5 A22	285	201
B5 B11	343	183
B5 B21	348	197
B5 B12	287	182
B5 B22	297	184
B6 A11	366	186
B6 A21	375	216
B6 C11	278	171
B6 C21	271	187
B8 A11	356	208
B8 A21	269	168
B8 A12	277	209
B6 B11	360	197
B6 B21	346	200
B8 B11(2)	234	
B8 B21(2)	229	

(1) The standard deviation was measured from the FE models with the modified BMD distribution (Fig 6-4).
(2) For these specimens the CT data was mislaid after the BMD analysis and no FE models could be generated.

The solution of the FE analysis provided prediction values of the apparent elastic modulus of the specimens in each testing direction. The predicted apparent moduli were compared with the average experimental elastic moduli from Chapter 4. Two analyses of the data were carried out separately. First, the apparent moduli calculated by averaging the three orthogonal testing directions were compared with the results from the FE models. Second, the individual orthogonal elastic moduli corresponding to the three testing directions were introduced in the analysis. In addition, both material models were considered, namely the isotropic model and the orthotropic model whose principal directions have been previously assessed by means of the fabric tensor analysis.

Good correlation was found for average apparent moduli both for the isotropic and orthotropic models ($R^2 = 0.71$, slope 0.88 and $R^2 = 0.72$, slope 0.73, respectively; $p < 0.01$).

By contrast, the individual orthogonal apparent moduli were less correlated between the FEA predictions and experimental data. In this case, the orthotropic model provided

better correlation than the isotropic model ($R^2 = 0.63$, slope 0.54 and $R^2 = 0.52$, slope 0.56, respectively; $p < 0.01$).

(a)

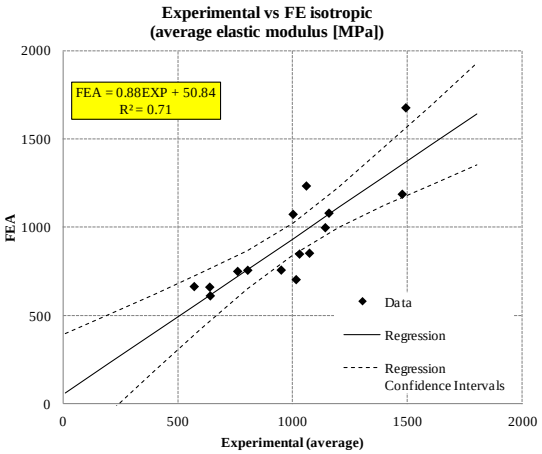

(b)

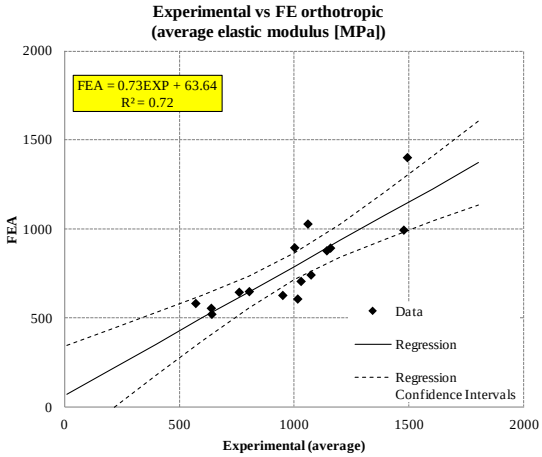

(c)

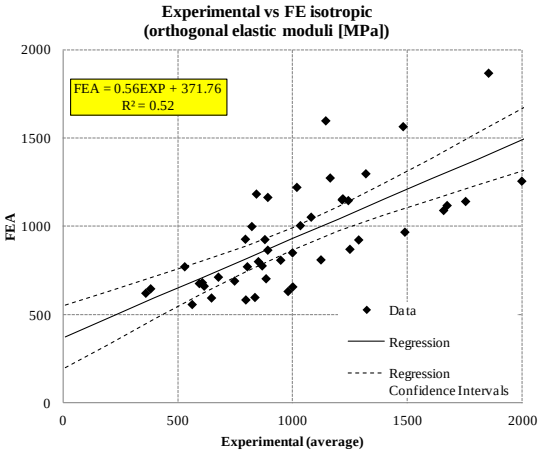

(d)

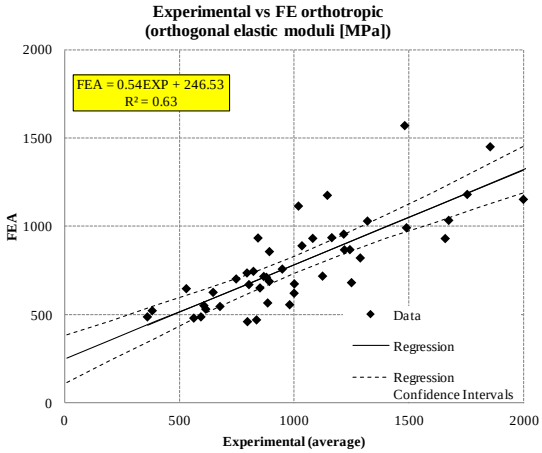

Fig. 6-7. Regressions between FE predictions and experimental observations: (a) average apparent modulus and FE isotropic model, (b) average apparent modulus and FE orthotropic model, (c) orthogonal moduli and FE isotropic model, (d) orthogonal moduli and FE orthotropic model.

A generalized underestimation in elastic modulus could be observed for the FE predictions. The isotropic material model provided a stiffer mechanical response of the specimens than the orthotropic models.

Table 6-2. Descriptive statistics of apparent elastic modulus for the experimental results (Exp) and FE predictions values of the isotropic model (FEA-Iso) and orthotropic model (FEA-Ortho)

	Elastic Modulus [MPa]		
n = 48	Exp	FEA Iso	FEA Ortho
Max	1997	1869	1572
Min	361	558	461
Mean	1018	942	794
SD	380	297	257

6.4 Discussion

This chapter presented the results of the finite element analysis performed on human trabecular bone specimens tested mechanically in Chapter 4, where two different material property relationships based on the BMD were obtained.

Based on QCT, inhomogeneous FE models were created. First, isotropic material models were considered to describe the elastic behavior of the trabecular specimens. Second, orthotropic material models were also introduced into the analysis. The models were implemented using a morphological evaluation of the trabecular bone from the fabric tensor analysis. The latter enabled the estimation of the principal material directions which were taken into account in the orthotropic model.

An additional analysis was performed in order to assess whether the boundary conditions of the FE models (e.g. presence of friction) could influence the evaluation of the apparent elastic modulus. In this manner, an overestimation of the apparent modulus due to the presence of friction could be assessed to be in a range of 6%.

In the previous chapter, continuum FE models of several femora could provide good predictions of the global mechanical response of the bones. In addition, it was considered worthwhile to evaluate these models based on QCT at the meso level of the trabecular specimens. Thus, the aim of this study was to look into the scope and limitations of the continuum FE models based on the BMD as well as to figure out several strategies in order to improve the FE predictions of this method.

The mean apparent modulus of the specimens, calculated by averaging the three orthogonal elastic moduli of the mechanical tests, could be significantly correlated with the predicted mean apparent moduli. Both the isotropic and orthotropic models presented similar correlation coefficients of 0.71 and 0.72, respectively. However, the orthotropic models produced higher underestimation of the apparent modulus than the isotropic models (slope 0.88 and slope 0.73, respectively for the isotropic and orthotropic models). When considering the orthogonal moduli of the specimens, the predictions from the models showed lower correlations. Thus, the predictions of the isotropic model correlated

with the experimental observations by (R^2 = 0.52), while the orthotropic model led to higher correlations by (R^2 = 0.63).

The underestimation of the predicted moduli may come from the averaging of densities within the whole trabecular specimen, on which the experimental correlations are based. It also could come from the segmentation of the specimens. The latter could be analytically discarded after having performed additional simulations with rescaled specimen dimensions. In the case of the orthotropic models it could be derived from the analysis of the material directions of the fabric tensor.

These results have to be interpreted taking into account the source of the bone material models. The experimental relations between elastic modulus and bone mineral density, on which the models were based, presented correlations ranged from 0.65 to 0.77. Therefore, the experimental data variability itself may be considered a major limitation of the models.

The simulation results are in the range of values found in previous studies (Goulet, et al., 1994; Matsuura, et al., 2008; Charlebois, 2008). In the latter two studies, the models were based on exhaustive morphological analyses of the micro structure of the trabecular specimens. The modulus predictions based on the axial fabric presented correlation coefficients passing from 0.69 to 0.79. In contrast to the present study, the specimens were obtained from different kinds of bones collecting a considerable large dataset. However, in all cases the specimens were cylindrical allowing them to be tested only in one spatial direction, which was usually aligned on purpose with the main trabecular/anisotropy direction. This led thus to a certain loss of essential information concerning the orthotropic mechanical response of the trabecular specimens.

In the current study, it was observed that the introduction of morphological analysis into the continuum FE models based on BMD experimental relations may improve the apparent modulus predictions. Although the principal anisotropy directions were considered the most relevant and actually the only considered parameters, the analysis of the fabric tensor or fabric ellipsoid may provide additional information, which should be considered in further studies.

7 Conclusions

In recent years, much effort has been spent in studying the mechanical properties of bone in order to understand its complex response to the external loads. The properly comprehension of the mechanical response of bones is of clinical relevance. From the analysis of the behavior of bone a large number of challenges could be undertaken: the estimation of fracture risk, the reduction of the stress shielding by means of more suitable and patient-specific implants preventing the aseptic loosening, revision cases, etc. In addition, the developments of theoretical and computational models, which describe the bone response, have to take into consideration both the improvement of the accuracy of the models and the applicability to the clinical requirements.

In this research project numerical and experimental techniques were used to analyze the mechanical response of the human femur as well as of the trabecular bone contained within the proximal femur. Experimental analyses of bone specimens led to an improved understanding of the mechanical behavior of trabecular bone and bone in general, and to the development of models to predict this behavior.

By means of the high resolution quantitative computer tomography FE models based on continuum mechanics were developed in order to evaluate and predict non-invasively the mechanical response of the human femur. The generation and validation of such models required a comprehensive biomechanical experimental study of the human femur and of the trabecular bone, which are mainly responsible for the anisotropic elastic response of the proximal femur. The aim of the present study was, on the one hand to characterize the mechanical properties and response of the bone using a double experimental procedure, and on the other hand, to develop and validate the FE models using those experimental data.

The experimental procedure took into account two structural levels. At the macro-level, complete human femora were mechanically tested. To cover a wider range of the mechanical response, the bones were tested under different load conditions and directions, which corresponded to different anatomical position. In the same manner, two load levels

were considered for the tests proving that the bone exhibited a linear mechanical response under the defined load conditions (Keaveny, et al., 1994). In all cases, the femora were distally fixed and the head was loaded. The bone response was measured from the strains, using strain gages glued to the bone surface and from the displacement of some landmarks by means of a 3D digitizing system (Microscribe). The mechanical tests were conducted paying great attention to the implementation of the FE models, so that the experiment conditions could be easily and accurately reproduced in the simulations.

At the meso-level, cubical trabecular specimens were harvested from the head of the bones tested previously. For that purpose, a standard specimen-taking procedure was developed. First, the axis of the femur head-neck was defined by means of a custom made device. Second, the main cutting plane was established containing the head-neck axis and the other cutting planes were defined orthogonally. Using these references, the proximal femora were cut with a diamond band saw. Prior to the mechanical test, complete QCT scans of the trabecular specimens were performed. The mechanical test comprised two different approaches in order to correct the experimental error involved in testing unconfined specimens by compression. On the one hand, the extensometer technique enabled to measure directly strains on the surface of the specimen and the stresses were calculated dividing the applied force by the cross section of the specimen. On the other hand, the pressure film technique enabled to estimate the effective contact area between the compression platens and the specimen sides, which could be used to correct the effective stress applied on the specimen. Strains across the total length of the specimen were taken from the corrected displacement of the actuator. In all cases, the specimens were tested in three orthogonal directions allowing for a better comprehension of the orthotropic properties of trabecular bone. The bone mineral density of the specimens, measured from the CT scans, could be highly correlated with the elastic modulus calculated from both experimental methods. From the correlation of the average apparent modulus, an isotropic material model was defined. Likewise, from the correlations of the orthogonal elastic moduli, an orthotropic model was also proposed.

The latter material models were used for developing continuum FE models of the femora. Using CT scans of the bone, which were taken before the mechanical testing, 3D solid models were generated. The modeling comprised the segmentation of the CT images in order to define the boundary surface of the bone. Subsequently, it was converted into a CAD surface and solid model to be imported to the FE software. At the same time, from the CT data an inhomogeneous material distribution data was created based on BMD calibration. The BMD assignment was accomplished by node, using a user-subroutine, thereby enabling the calculation of the elastic constants (i.e. elastic modulus) from the above mentioned material models. According to Wolf's law, it was assumed that the material directions of the orthotropic model coindicided with the principal directions of stresses, calculated in the isotropic models. The simulations reproduced the same load and constraint conditions as those from the mechanical tests of the femora. The predictions of the FE models could be highly correlated with the experimental observations.

In the final chapter, similar FE simulations were carried out for the cubical trabecular specimens. Since the correlations between the elastic modulus and the BMD were based on the average density over the whole specimens, it was looked into whether continuum FE models based on such correlations and a high voxel refinement could also explain the orthotropic elastic response at the meso-level of the trabecular specimens.

7.1 Discussion

The mechanical properties and their corresponding correlations were obtained from the compression testing of unconfined trabecular bone. As shown by Keaveny et al. (1997), this experimental procedure involves some systematic errors. Some of them could be avoided or minimized using an extensometer and embedding the ends of the specimen. For obvious reasons, the latter cannot be adopted for the evaluation of orthogonal mechanical properties. Although the use of the extensometer reduced the underestimation because of the end-artifacts, a considerable amount of experimental variability still remains (Appendix B), due mainly to the unknown phenomenon of platens-specimen contact. In this regard, a new approach was hereby proposed to estimate the effective contact area in compression testing of trabecular bone. This novel approach included a calibration procedure by means of biomaterial specimens and the image analysis of the pressure map images acquired by pressure sensitive film.

Some known features of the physiological loading of the human femur were not considered in the mechanical tests of the femora. The proposed experimental setup comprised a single loading condition applied on the head of the bone, leaving the muscle forces (Fig. 1-3) applied on the greater trochanter out of the experiments. Few studies have experimentally tested the human femur under complex load conditions and generally focused on the implant stability rather than on the bone mechanical response (Finlay, et al., 1991; Britton, et al., 2003; Park, et al., 2010). In that respect, more studies can be found only from the numerical point of view (Polgar, et al., 2003; Ramos, et al., 2006; Speirs, et al., 2007).

In order to cover a wider range of the mechanical response of the bone, the specimens were loaded at three different angle positions, which were considered to reproduce sufficiently the physiology of the bone (Speirs, et al., 2007; Juszczyk, et al., 2011). On the other hand, extremely non-physiological loading were also not introduced in the analyses. These non-physiological cases take place typically in accidents as, for example, a fall on the side (Verhulp, et al., 2008). In such cases, the anisotropic mechanical behavior of the bone becomes more important and that represents a major challenge to the numerical models. The mechanical response of the bone was captured from its global displacement, measured at several points, as well as its strain state, which was acquired continuously by some strain gages at different bone locations.

The continuum FE models and simulations were consequently designed in order to reproduce the same load and constraint conditions as those from the mechanical experiments. The generation of FE models on the basis of QCT scans may lead to some

numerical errors. At first, both the geometrical representation and the inhomogeneous material distribution are dependent upon the CT voxel resolution. Moreover, although in the last years the segmentation of the CT images has been partially automated, this process still requires the manual intervention of an operator, for instance, to specify thresholds and to close incomplete boundaries. The second major challenge in FE modeling is to be able to define accurately the loads and constraints and thus connecting the experimental coordinate system to that of the FE models. In order to overcome these shortcomings, the 3D digitizing system (Microscribe) used for measuring the displacement was also employed to capture the exact position and orientation of the bone with regard to the load and constraint.

Finally, the trabecular specimens were modeled from the QCT scans following a similar process to that used for the bones. In contrast to the latter, the segmentation was entirely manual and the material principal directions could not be directly acquired from the stress field. For such purpose, a morphological analysis was performed from the CT scans, which were conveniently converted into binary images. The fabric tensor employed in this analysis consists of a stereological measure of the anisotropy of the bone structure and it may provide the main anisotropy directions. The orthotropic model proposed in this study took advantage of this analysis assigning the material directions calculated from the fabric tensor, which improved the correlation between predicted and experimental orthogonal moduli.

Overall, the experimental procedure developed in the present study enabled the generation and validation of specific continuum FE models of the human femur, which provide comprehensive knowledge of the elastic mechanical response of this bone. On the other hand, further developments have to be achieved in order to improve the proposed models in view of their application in clinical studies.

7.2 Future work

The proposals can be divided into two groups, regarding the two disciplines involved in the present study, namely experimental and numerical. Likewise, another separation could be made concerning the scale of the study, such as the meso level which focuses on the study of bone tissue (i.e. small trabecular or cortical specimens) and the macro level which focuses on the mechanical response of complete bones.

From the experimental point of view, more effort is needed to enhance the understanding of the anisotropic mechanical response of the bone. In that respect, both physiological and non-physiological configurations have to be introduced in the experiments to cover a wider range of the bone behavior. On the other hand, at the meso level the orthotropy of the trabecular bone has been studied over the last years (Keyak, et al., 1994; Rho, et al., 1995; Majumdar, et al., 1998; Kaneko, et al., 2004). However, there is still a lack of standardization about the sample-taking procedure and about the mechanical testing protocols. The reproducibility and accuracy for evaluating the mechanical properties might be also improved introducing new experimental approaches,

such as the pressure film method which was developed in the present study. This technique could provide additional information by the mechanical testing of unconfined specimen, so minimizing the experimental error due to the end artifacts. In consequence, further calibration protocols will need to be undertaken to provide reliable estimation of the effective contact area for correcting the mechanical testing of unconfined trabecular specimens.

Furthermore, the finite element models can directly take advantage of the improvements of the experimental field either to generate more complex and reliable models or to validate these numerical models in a more precise way and for a wider range of anatomical situations. The developments from the numerical point of view should focus on two aspects. Firstly, the accuracy and complexity of the models should be further improved. Secondly, at the same time the modeling procedure should take into account future requirements for clinical applications, for instance, more simple integration of QCT data into the FEM tools as well as a substantial reduction of the computation time.

Appendix A Experimental data

A.1 Experimental data and FE predictions from the mechanical tests of the human femora

Specimen	Position angle [°]	Measure	Experimental	Isotropic model	Orthotropic model		
					0°	7°	15°
Bone 3	0°	SG1	NA	NA	NA	NA	NA
		SG2	-725	-845	-846	-849	-972
		SG3	-1357	-971	-1002	-999	-1025
		SG4	1028	705	627	629	805
		SG5	750	396	339	430	351
	7°	SG1	NA	NA	NA	NA	NA
		SG2	-817	-872	-882	-874	-890
		SG3	-1009	-684	-545	-541	-607
		SG4	664	439	345	341	448
		SG5	-112	-235	-294	-249	-257
	15°	SG1	NA	NA	NA	NA	NA
		SG2	-854	-811	-709	-696	-701
		SG3	-711	-198	-193	-181	-176
		SG4	433	262	44	40	44
		SG5	-686	-1041	-969	-988	-894
Bone 4	0°	MS1	385	607	541	585	582
		MS2	328	699	622	671	670
		MS3	252	503	444	482	467
		SG1	-177	-126	-182	-208	-126
		SG2	-940	-1227	-1088	-1118	-1207
		SG3	773	767	690	696	945
		SG4	-1027	-1070	-984	-966	-1002
		SG5	NA	NA	NA	NA	NA
	7°	MS1	221	155	176	177	205
		MS2	173	174	205	208	241
		MS3	130	124	133	133	150
		SG1	75	209	186	166	202
		SG2	-682	-420	-479	-476	-562
		SG3	712	413	462	460	637
		SG4	-986	-937	-983	-965	-970
		SG5	627	1154	1027	917	1115
	15°	MS1	416	610	559	603	540
		MS2	469	670	606	655	584
		MS3	399	553	505	541	485
		SG1	141	349	422	384	300
		SG2	362	692	632	682	604
		SG3	289	48	69	65	77
		SG4	-996	-906	-877	-861	-836
		SG5	516	694	641	593	627

NA: data not available

Specimen	Position angle [°]	Measure	Experimental	Isotropic model	Orthotropic model		
					0°	7°	15°
Bone 5	0°	MS1	145	180	171	176	186
		MS2	324	457	430	451	459
		MS3	437	656	619	650	667
		SG1	-363	-488	-458	-465	-482
		SG2	272	375	340	343	365
		SG3	-992	-1163	-1092	-1054	-1042
		SG4	551	707	688	698	736
		SG5	-1076	-1308	-1221	-1220	-1819
	7°	MS1	101	84	80	80	88
		MS2	131	135	125	128	145
		MS3	224	229	214	218	243
		SG1	-389	-382	-357	-360	-368
		SG2	227	298	269	271	289
		SG3	-971	-1102	-1122	-1082	-1058
		SG4	505	512	499	502	526
		SG5	-813	-701	-661	-655	-956
	15°	MS1	96	20	19	23	18
		MS2	300	227	220	238	214
		MS3	326	263	254	281	246
		SG1	-347	-259	-252	-248	-247
		SG2	151	215	225	230	239
		SG3	-907	-1049	-1105	-1067	-1032
		SG4	329	272	267	262	268
		SG5	-40	-82	-124	-115	-95
Bone 6	0°	MS1	624	647	608	652	656
		MS2	488	478	447	485	480
		MS3	424	408	381	420	405
		MS4	187	199	188	198	202
		SG1	-1030	-1812	-1773	-1742	-1732
		SG2	-501	-568	-518	-524	-537
		SG3	174	325	337	340	351
		SG4	713	768	710	717	824
		SG5	-264	-269	-292	-289	-306
		SG6	-1157	-1090	-984	-1043	-1054
	7°	MS1	199	222	216	210	241
		MS2	152	151	145	141	160
		MS3	82	65	56	60	73
		MS4	73	88	84	84	92
		SG1	-982	-1604	-1535	-1528	-1523
		SG2	-449	-459	-419	-422	-430
		SG3	130	255	265	266	274
		SG4	482	497	458	460	524
		SG5	-186	-175	-194	-193	-203
		SG6	-400	-335	-308	-304	-358
	15°	MS1	475	454	443	482	422
		MS2	439	407	398	431	380
		MS3	356	380	346	380	335
		MS4	NA	NA	NA	NA	NA
		SG1	-896	-1269	-1213	-1203	-1206
		SG2	-365	-318	-292	-291	-292
		SG3	84	162	172	170	173
		SG4	209	156	152	147	156
		SG5	-48	-62	-85	-84	-79
		SG6	613	621	596	666	561

Specimen	Position angle [°]	Measure	Experimental	Isotropic model	Orthotropic model		
					0°	7°	15°
Bone 7	0°	MS1	1108	937	876	909	945
		MS2	970	811	757	786	818
		MS3	885	733	684	711	735
		SG1	-1112	-890	-849	-845	-917
		SG2	788	765	701	715	733
		SG3	-1212	-1336	-1242	-1238	-1302
		SG4	1247	1438	1317	1449	1345
		SG5	NA	NA	NA	NA	NA
	7°	MS1	560	353	336	329	373
		MS2	491	302	288	282	320
		MS3	436	266	251	247	279
		SG1	-714	-681	-652	-646	-694
		SG2	398	495	451	457	469
		SG3	-912	-856	-802	-796	-828
		SG4	317	212	228	214	249
		SG5	NA	NA	NA	NA	NA
	15°	MS1	77	354	327	366	326
		MS2	77	345	328	346	311
		MS3	91	331	320	341	306
		SG1	-487	-512	-478	-469	-494
		SG2	369	354	325	322	331
		SG3	-450	-410	-394	-385	-384
		SG4	261	359	358	376	352
		SG5	NA	NA	NA	NA	NA
Bone 8	0°	MS1	64	64	59	61	59
		MS2	704	816	763	770	816
		MS3	931	1072	1004	1013	1075
		MS4	1104	1295	1216	1225	1305
		SG1	1424	1923	1821	1870	1841
		SG2	-1968	-1921	-1765	-1762	-1940
		SG3	849	866	814	816	845
		SG4	-1565	-2035	-1674	-1671	-1700
	7°	MS1	45	23	20	21	21
		MS2	449	391	363	364	397
		MS3	612	533	497	498	542
		MS4	751	669	626	627	683
		SG1	690	677	627	627	653
		SG2	-1520	-1187	-1092	-1089	-1188
		SG3	820	773	730	729	752
		SG4	-1596	-1772	-1645	-1633	-1656
	15°	MS1	47	32	31	32	30
		MS2	104	193	185	194	181
		MS3	125	210	202	213	197
		MS4	111	217	211	219	204
		SG1	-733	-1007	-965	-1020	-936
		SG2	-514	-138	-149	-146	-127
		SG3	685	518	496	493	493
		SG4	-1453	-1451	-1486	-1465	-1452

A.2 Experimental data from the mechanical tests of the trabecular bone specimens.

	BMD	Geometry [mm]			E Modulus (Pressure film method) [MPa]				E Modulus (Extensometer method) [MPa]			
Specimen	*[mg/cm³]*	*D1*	*D2*	*D3*	*D1*	*D2*	*D3*	*Mean*	*D1*	*D2*	*D3*	*Mean*
K5 A11	431	12.47	10.05	10.50	1636	1259	1708	1534	1325	1029	1996	1450
K5 A12	313	12.93	10.50	10.10	816	1074	1187	1026	789	924	1387	1033
K5 A21	374	12.93	10.53	10.98	896	1155	1229	1093	788	881	1407	1025
K5 A22	285	13.05	10.32	10.55	872	1248	919	1013	799	998	864	887
K5 B11	343	10.68	10.58	10.00	837	968	1463	1089	751	790	2042	1194
K5 B12	287	10.39	9.90	10.69	742	1032	1025	933	850	968	1473	1097
K5 B21	348	10.83	10.14	10.53	1037	1013	982	1011	1029	1147	801	992
K5 B22	297	10.88	10.05	10.43	821	837	1037	898	880	392	858	710
K8 A11	356	10.78	10.44	10.82	1713	715	1154	1194	1263	929	1172	1121
K8 A21	269	10.78	10.53	10.39	1212	576	538	775	556	1158	522	745
K8 A12	277	10.61	10.55	10.25	680	735	811	742	613	452	542	536
K8 B11	234	10.41	10.54	10.38	582	634	748	655	527	348	496	457
K8 B21	229	10.38	10.40	10.44	550	643	722	638	565	481	480	509
K6 A11	366	10.10	9.50	9.73	1636	1345	2024	1668	1677	1139	1197	1338
K6 A21	375	10.14	10.80	9.64	1272	2084	1530	1629	1164	1909	900	1324
K6 C11	278	10.25	9.60	9.70	836	397	489	574	658	324	724	569
K6 C21	271	10.90	10.30	9.60	591	1141	416	716	534	818	347	566
K6 B21	346	10.03	10.88	9.92	685	992	374	684	513	1064	947	841
K6 B11	360	10.01	9.89	9.73	635	597	573	602	820	855	665	780

FE predictions and average experimental results for apparent elastic modulus

Specimen	BMD [mg/cm³]	Average experimental E Modulus [MPa]			FE predicted E Modulus Isotropic model [MPa]			FE predicted E Modulus Orthotropic model [MPa]		
		D1	D2	D3	D1	D2	D3	D1	D2	D3
K5 A11	431	1480	1144	1852	1566	1599	1869	1572	1177	1452
K5 A12	313	803	999	1287	772	851	924	671	622	822
K5 A21	374	842	1018	1318	1184	1222	1299	935	1116	1031
K5 A22	285	836	1123	891	598	811	866	471	719	689
K5 B11	343	794	879	1752	928	926	1142	737	712	1182
K5 B12	287	796	1000	1249	584	658	871	461	675	682
K5 B21	348	1033	1080	892	1005	1053	1165	891	933	858
K5 B22	297	850	615	948	801	662	809	652	532	759
K6 A11	366	1657	1242	1672	1091	1147	1119	932	869	1035
K6 A21	375	1218	1997	1215	1157	1257	1151	868	1154	957
K6 C11	278	747	361	607	691	622	682	703	488	552
K6 C21	271	562	980	382	558	632	647	481	557	523
K8 A11	356	1488	822	1163	968	1000	1275	993	746	937
K8 A21	269	884	867	530	704	777	772	567	717	648
K8 A12	277	647	594	677	595	677	713	627	488	547

Appendix B FE Evaluation of the Influence of the stress distribution on deformation measures on a cubical specimen

The determination of the orthogonal elastic moduli of trabecular bone commonly involves mechanical compression tests of cubical and unconfined specimens. This kind of setup with unconfined (e.g. non-glued) specimens underestimates the elastic modulus compared to a setup using embedded end caps and an extensometer (Keaveny, et al., 1997). Since the end caps prevent the specimen to be tested in more than one direction, unconfined specimens have to be tested in order to evaluate the orthogonal elastic moduli. The use of an extensometer is highly recommendable to reduce the influence of the underestimation due to the end effect artifacts (Kaneko, et al., 2003). Thus, a series of four modulus measurements is generally made in each test direction attaching the extensometer to each side of the cubical specimen. Subsequently, these four moduli are averaged to give the apparent modulus in the corresponding direction (Morgan, et al., 2003). The stresses are evaluated by dividing the force by the initial cross sectional area, which is usually the only known.

This method is based on the homogenization hypothesis described by Saint-Venant's principle. Thus, it is assumed that the strains are regularly distributed within the specimen. However, this assumption could not be fully appropriate for unconfined specimens. Therefore, care has been taken to average the measurements from the extensometer.

The purpose of this study was to evaluate the systematic error associated to the method of the extensometer in compression testing of unconfined specimens. In view of these results, a suitable averaging method was proposed in order to determine the elastic modulus from the measurements of the extensometer.

A homogeneous cubical specimen (10 x 10 x 10 mm³) was modeled and several contact area definitions were proposed where the force and the support should be applied (Fig. B-1).

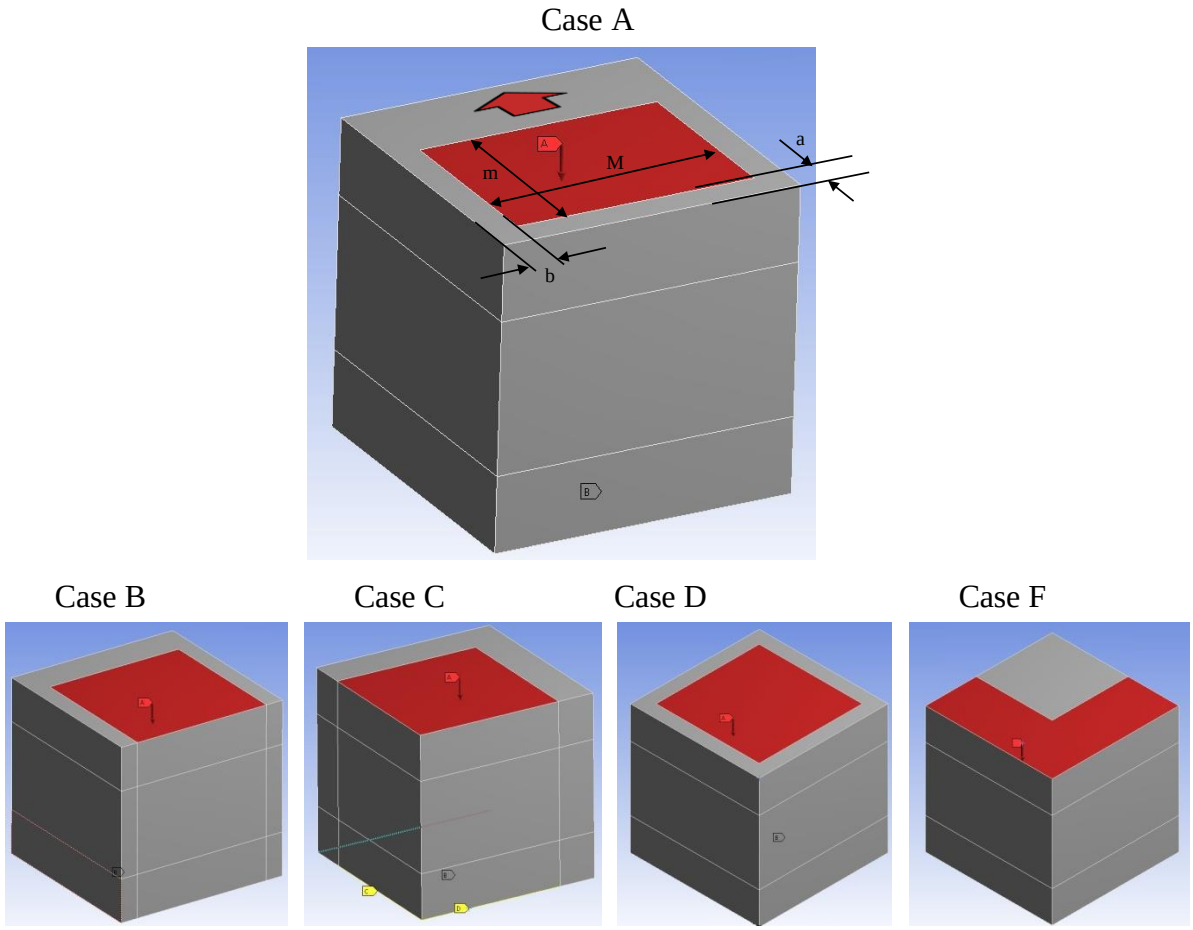

Fig. B-1. Theoretical irregular loading cases proposed in the analysis. The different cases are identified by a letter in order to make the results understandable. Note: a Case E nomenclature was not used to avoid possible misunderstanding with the nomenclature of the elastic moduli (E1, E2, E3).

Symmetric contact conditions were considered for the force and the constraint. The latter was defined as frictionless. A reference elastic modulus was established on 1000 MPa and Poisson's ration on 0.3.

From the solutions, the strain was measured in the same way that the extensometer would have done, i.e. from the relative displacement between the knife edges with an initial separation of 5 mm for the present study. In the models, the strains were calculated from the displacement of two lines separated 5 mm (Fig. B-1). The stresses were evaluated, as mentioned above, dividing the force by the cross section of the specimen (100 mm²).

The different load cases are summarized in Table B-1 with the results from the FE analyses.

Table B-1. Results summary for the theoretical loading cases of Figure B-1. The table includes the loading area and position, the partial moduli measured on the different sides (E1 to E4), the apparent moduli calculated following the method described in this appendix and, finally the numerical error of the averaging procedure.

	Load Area [mm²] (M x m)	Position (a x b)	E1 [MPa]	E2 [MPa]	E3 [MPa]	E4 [MPa]	Harmonic mean method E [MPa]	Error (%)
Case A1	32 (8x4)	1x1 mm	583	1373	1373	-3343	945	-5
Case A2	48 (8x6)	1x1 mm	902	1289	1289	-38753	1128	13
Case A3	56 (8x7)	1x1 mm	1089	1298	1298	3447	1220	22
Case B1	63 (9x7)	0x0.5	603	1166	1166	-7345	889	-11
Case B2	64 (8x8)	0x1	696	1406	1406	6696	1049	5
Case C1	48 (8x6)	0.5x1.5	651	932	2403	-6032	992	-1
Case C2	48 (8x6)	0x0	502	714	8292	-3508	854	-15
Case C3	64 (8x8)	0x0	684	684	6493	6493	974	-3
Case D1	64 (8x8)	centered	1328	1328	1328	1328	1328	33
Case D2	81 (9x9)	centered	1117	1117	1117	1117	1117	12
Case F1	51 (L 3x10)	-	506	506	3470	3470	884	-12
Case F2	64 (L 4x10)	-	608	608	2577	2577	983	-2
							Mean CV (%)	14.1%

The proposed averaging method was based on the harmonic mean (B-1) and taken into consideration the values of the partial elastic moduli.

Since the harmonic mean of a list of numbers tends strongly toward the least elements of the list, it tends (compared to the arithmetic mean) to mitigate the impact of large outliers and aggravate the impact of small ones. The harmonic and the arithmetical mean tend to be equal when the values of the dataset are equal.

$$H = \frac{n}{\sum_{i=1}^{n} \frac{1}{x_i}} \qquad \text{B-1}$$

The values were ordered by magnitude. If the highest value was negative (tension) or an order of magnitude higher than the smallest, it was taken out of the average calculation and the harmonic mean was calculated from the other three values. Else, if the four values are in the same order of magnitude with significant deviation, the average elastic modulus was determined from the harmonic mean of the four values.

As it can be observed in Table B-1, the position of the load distribution may have significant influences on the measurements of the extensometer. As a result, asymmetric load distributions produced a considerable variability among the elastic moduli measured on the different sides of the cube.

In the same way, a centered load distribution in an area representing the 64% of the cross section may produce an overestimation of the apparent modulus of 33%.

The proposed averaging method undertook to provide the most reproducible and reliable mean value of the apparent elastic modulus.

The coefficient of variation for all the load cases was determined as follows:

$$CV(\%) = \frac{1}{1000}\sqrt{\frac{\sum_{i=1}^{12}(1000 - x_i)^2}{12}} \qquad \text{B-2}$$

where, x_i is the mean elastic modulus of each case, 1000 (MPa) represents the theoretical elastic modulus assigned to the model and 12 is the number of cases considered.

Thus, the coefficient of variation was 14.1 % for the twelve load cases. This value did not represent the real experimental error but an estimation of the probable deviation due to the nature of the measuring technique of unconfined specimens with an extensometer.

Appendix C FE Evaluation of the boundary conditions and contact friction in compression testing of cubical trabecular specimens

The influence of the friction was evaluated in the following study in order to define the suitable boundary condition for the FE models of the trabecular specimens. Furthermore, the probable error due to the different boundary conditions of the FE models could be also quantified.

For that purpose, the FE models of two trabecular specimens were taken into consideration. They were selected regarding a wide range of bone mineral density (269 – 356 mg/cm³). Their geometry was simplified to regular parallelepipeds. Then, different cases were conceived varying the boundary conditions, which are presented as follows:

A. Cube model

For the first model, only the cubical specimen was modeled and some boundary conditions were applied on two of its sides (Fig. C-1).

A1. Free: there was no constraint for the Poisson's effect. A normal displacement was applied on one side of the cube and the opposite side was constrained only in the same normal direction of the displacement. Additional constraints were defined to avoid rigid body motion enabling the cube to deform in the other orthogonal directions. Instead of a pressure force, a displacement was applied to the model because it was considered to represent better the compression test with compression platens.

A2. Asymmetric constraint: the side with the displacement condition was allowed to deform in the two other orthogonal directions. The supported side was fully constrained.

A3. Symmetric constraint: the displacement was also restricted in all directions but in the normal. It represented the most extreme boundary condition with a fully restriction of the Poissson's effect on both sides of the cube.

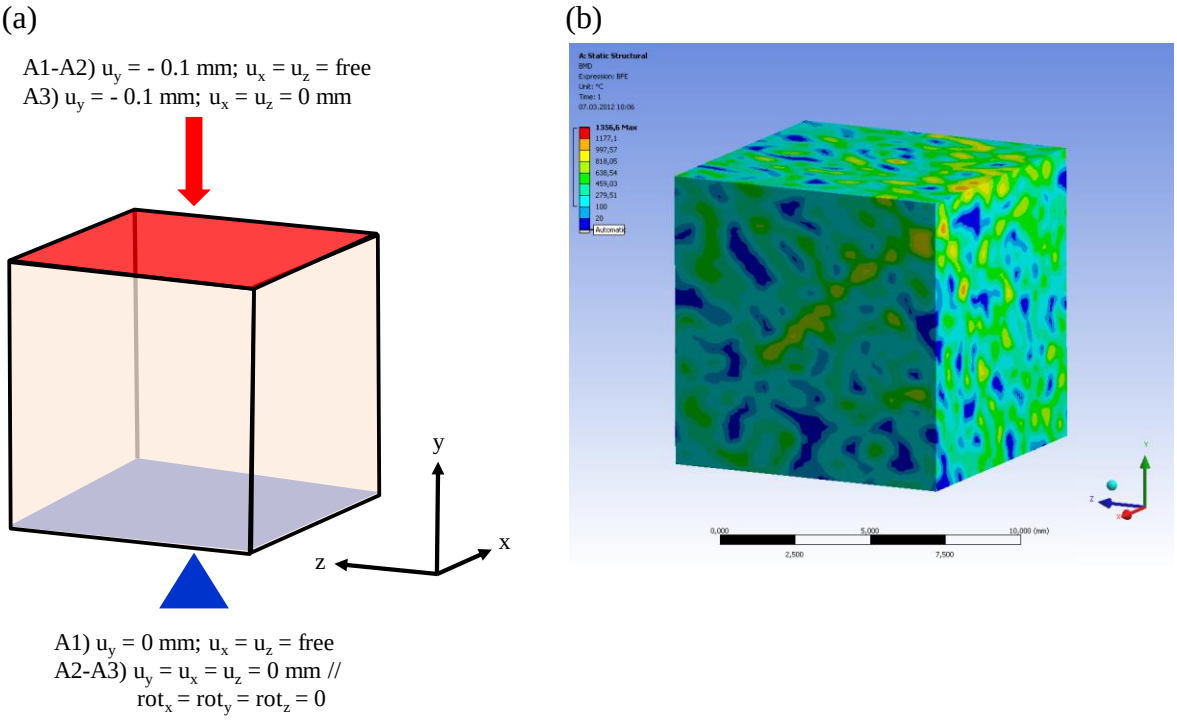

Fig. C-1. Simplified cube model. (a) Load and constraint definition for the different subcases, (b) BMD distribution of the selected specimen.

B. Cube and steel platens model

A second case, the compression platens were also included in the model and the contact between the specimen and platens was modeled (Fig. C-2).

B1. Frictionless: the contact between the cube and the compression platens was defined as frictionless allowing the relative movement between the contact surfaces involved.

B2. Friction: both contacts were modeled as frictional contacts considering different coefficients of friction (0.2, 0.3 and 0.5). The contacts were modeled with an Augmented-Lagrange algorithm, asymmetric behavior and "adjustment to touch". A refinement mesh at the contact areas was created using a hexahedral dominant method. Several tetrahedrons had to be automatically created within the steel platens models. It did not represent any inconvenience since the aim of the study did not focus on the inner strain field of the platens.

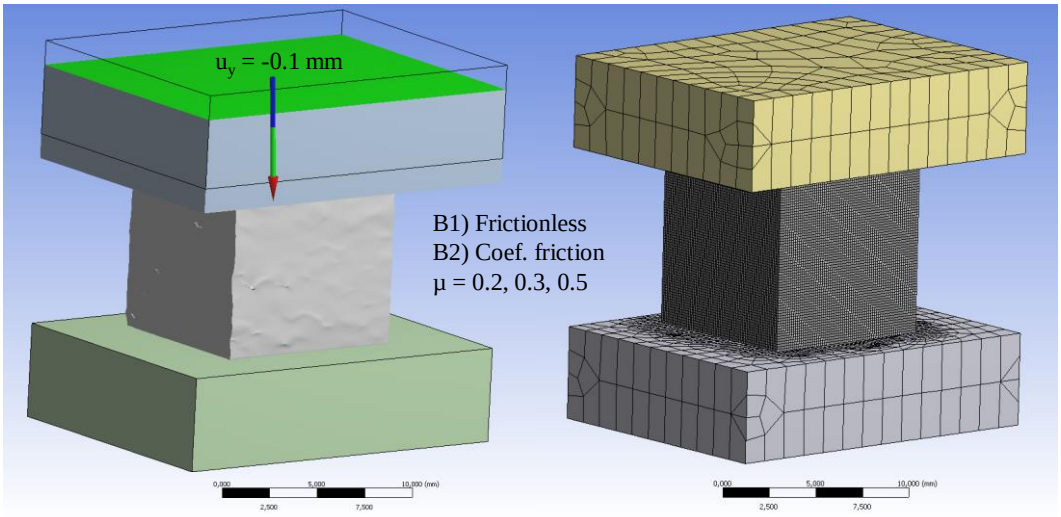

Fig. C-2. Specimen and compression platens model. The contact analysis was included in the model for different friction coefficients. Left, the loading consisted of an predefined displacement of 0.1 mm. Rigth, the mesh was adequately adapted to the contact problem.

Specimen low bone mineral density (B8A12, BMD =269 mg/cm³)

	Elastic modulus (MPa)	Variation (%)
A1	581	Ref. value for A
A2	597	2.84
A3	649	11.75
B1	550	Ref. Value for B
B2 (μ = 0.2)	582	5.73
B2 (μ = 0.3)	585	6.33
B2 (μ = 0.5)	592	7.54

μ = coefficient of friction

Specimen high bone mineral density (B8A11, BMD = 356 mg/cm³)

	Elastic modulus (MPa)	Variation (%)
A1	935	Ref. value for A
A2	955	2.15
A3	1005	7.49
B1	904	Ref. Value for B
B2 (μ = 0.2)	927	2.55
B2 (μ = 0.3)	933	3.18
B2 (μ = 0.5)	939	3.95

μ = coefficient of friction

The contact between specimen and compression platens was modeled for coefficient of friction of 0.2, 0.3, 0.5 as well as a frictionless contact, which was used as reference. The difference in apparent modulus of the specimen with lower density (mean BMD = 269

mg/cm³) was found to be 5.73%, 6.33% and 7.54%, respectively. The specimen with higher density (mean BMD = 356 mg/cm³) presented a difference in apparent modulus of 2.55%, 3.18% and 3.95%, respectively.

Simplified models without steel platens were also generated and introduced in the analysis. The highest difference between the proposed models was found for the fully constrained specimen sides up to 11.75% and 7.49%, respectively for the specimen with low and high density.

Moreover, an slight overestimation was found between the simplified frictionless model without compression platens and the complex model with them to be 5.63% and 3.43%, for the specimen with low and high density. The results for the simplified frictionless model were comparable with the results of the complex models with a coefficient of friction ranged 0.2-0.3. The computational time for the simplified model analyses was about 30 minutes and considerably shorter than for the complex friction analyses that required over 4 hours of computation.

Therefore, in view of all these results, it was considered that the simplified frictionless model may reproduce with suitable accuracy low friction contacts between the specimen and the compression platens and considerably reduced the computation time.

Appendix D Programming code

D.1 Coordinate system transformation: Microscribe to CT image (MATLAB)

```
function [PCTM,T] = CSTransformation(PCTA,PCTB,PCTC,PCTD,PMA,PMB,PMC,PMD)
%PCTM translation vector (output)
%T rotation matrix (output)
%PCTA/B/C/D reference points in CT coordinates (input)
%PMA/B/C/D reference points in Microscribe coordinates (input)
xcta = PCTA(1);
ycta = PCTA(2);
zcta = PCTA(3);
xma = PMA(1);
yma = PMA(2);
zma = PMA(3);

xctb = PCTB(1);
yctb = PCTB(2);
zctb = PCTB(3);
xmb = PMB(1);
ymb = PMB(2);
zmb = PMB(3);

xctc = PCTC(1);
yctc = PCTC(2);
zctc = PCTC(3);
xmc = PMC(1);
ymc = PMC(2);
zmc = PMC(3);

xctd = PCTD(1);
yctd = PCTD(2);
zctd = PCTD(3);
xmd = PMD(1);
ymd = PMD(2);
zmd = PMD(3);
```

```
33
34  e = ((xctb-xctc)*((yma-ymb)*(zmc-zmd)-(ymc-ymd)*(zma-zmb))-(xcta-
35  xctb)*((ymb-ymc)*(zmc-zmd)-(ymc-ymd)*(zmb-zmc))-(xctc-xctd)*((yma-
36  ymb)*(zmb-zmc)-(ymb-ymc)*(zma-zmb)))/((ymc-ymd)*((xma-xmb)*(zmb-zmc)-
37  (xmb-xmc)*(zma-zmb))-(xmc-xmd)*((yma-ymb)*(zmb-zmc)-(ymb-ymc)*(zma-
38  zmb))-(zmc-zmd)*((xma-xmb)*(ymb-ymc)-(xmb-xmc)*(yma-ymb)));
39
40  f = -((xctb-xctc)*((xma-xmb)*(zmc-zmd)-(xmc-xmd)*(zma-zmb))-(xcta-
41  xctb)*((xmb-xmc)*(zmc-zmd)-(xmc-xmd)*(zmb-zmc))-(xctc-xctd)*((xma-
42  xmb)*(zmb-zmc)-(xmb-xmc)*(zma-zmb)))/((ymc-ymd)*((xma-xmb)*(zmb-zmc)-
43  (xmb-xmc)*(zma-zmb))-(xmc-xmd)*((yma-ymb)*(zmb-zmc)-(ymb-ymc)*(zma-
44  zmb))-(zmc-zmd)*((xma-xmb)*(ymb-ymc)-(xmb-xmc)*(yma-ymb)));
45
46  g = ((xctb-xctc)*((xma-xmb)*(ymc-ymd)-(xmc-xmd)*(yma-ymb))-(xcta-
47  xctb)*((xmb-xmc)*(ymc-ymd)-(xmc-xmd)*(ymb-ymc))-(xctc-xctd)*((xma-
48  xmb)*(ymb-ymc)-(xmb-xmc)*(yma-ymb)))/((ymc-ymd)*((xma-xmb)*(zmb-zmc)-
49  (xmb-xmc)*(zma-zmb))-(xmc-xmd)*((yma-ymb)*(zmb-zmc)-(ymb-ymc)*(zma-
50  zmb))-(zmc-zmd)*((xma-xmb)*(ymb-ymc)-(xmb-xmc)*(yma-ymb)));
51
52  h = ((yctb-yctc)*((yma-ymb)*(zmc-zmd)-(ymc-ymd)*(zma-zmb))-(ycta-
53  yctb)*((ymb-ymc)*(zmc-zmd)-(ymc-ymd)*(zmb-zmc))-(yctc-yctd)*((yma-
54  ymb)*(zmb-zmc)-(ymb-ymc)*(zma-zmb)))/((ymc-ymd)*((xma-xmb)*(zmb-zmc)-
55  (xmb-xmc)*(zma-zmb))-(xmc-xmd)*((yma-ymb)*(zmb-zmc)-(ymb-ymc)*(zma-
56  zmb))-(zmc-zmd)*((xma-xmb)*(ymb-ymc)-(xmb-xmc)*(yma-ymb)));
57
58  i = -((yctb-yctc)*((xma-xmb)*(zmc-zmd)-(xmc-xmd)*(zma-zmb))-(ycta-
59  yctb)*((xmb-xmc)*(zmc-zmd)-(xmc-xmd)*(zmb-zmc))-(yctc-yctd)*((xma-
60  xmb)*(zmb-zmc)-(xmb-xmc)*(zma-zmb)))/((ymc-ymd)*((xma-xmb)*(zmb-zmc)-
61  (xmb-xmc)*(zma-zmb))-(xmc-xmd)*((yma-ymb)*(zmb-zmc)-(ymb-ymc)*(zma-
62  zmb))-(zmc-zmd)*((xma-xmb)*(ymb-ymc)-(xmb-xmc)*(yma-ymb)));
63
64  j = ((yctb-yctc)*((xma-xmb)*(ymc-ymd)-(xmc-xmd)*(yma-ymb))-(ycta-
65  yctb)*((xmb-xmc)*(ymc-ymd)-(xmc-xmd)*(ymb-ymc))-(yctc-yctd)*((xma-
66  xmb)*(ymb-ymc)-(xmb-xmc)*(yma-ymb)))/((ymc-ymd)*((xma-xmb)*(zmb-zmc)-
67  (xmb-xmc)*(zma-zmb))-(xmc-xmd)*((yma-ymb)*(zmb-zmc)-(ymb-ymc)*(zma-
68  zmb))-(zmc-zmd)*((xma-xmb)*(ymb-ymc)-(xmb-xmc)*(yma-ymb)));
69
70  k = ((zctb-zctc)*((yma-ymb)*(zmc-zmd)-(ymc-ymd)*(zma-zmb))-(zcta-
71  zctb)*((ymb-ymc)*(zmc-zmd)-(ymc-ymd)*(zmb-zmc))-(zctc-zctd)*((yma-
72  ymb)*(zmb-zmc)-(ymb-ymc)*(zma-zmb)))/((ymc-ymd)*((xma-xmb)*(zmb-zmc)-
73  (xmb-xmc)*(zma-zmb))-(xmc-xmd)*((yma-ymb)*(zmb-zmc)-(ymb-ymc)*(zma-
74  zmb))-(zmc-zmd)*((xma-xmb)*(ymb-ymc)-(xmb-xmc)*(yma-ymb)));
75
76  l = -((zctb-zctc)*((xma-xmb)*(zmc-zmd)-(xmc-xmd)*(zma-zmb))-(zcta-
77  zctb)*((xmb-xmc)*(zmc-zmd)-(xmc-xmd)*(zmb-zmc))-(zctc-zctd)*((xma-
78  xmb)*(zmb-zmc)-(xmb-xmc)*(zma-zmb)))/((ymc-ymd)*((xma-xmb)*(zmb-zmc)-
79  (xmb-xmc)*(zma-zmb))-(xmc-xmd)*((yma-ymb)*(zmb-zmc)-(ymb-ymc)*(zma-
80  zmb))-(zmc-zmd)*((xma-xmb)*(ymb-ymc)-(xmb-xmc)*(yma-ymb)));
81
82  m = ((zctb-zctc)*((xma-xmb)*(ymc-ymd)-(xmc-xmd)*(yma-ymb))-(zcta-
83  zctb)*((xmb-xmc)*(ymc-ymd)-(xmc-xmd)*(ymb-ymc))-(zctc-zctd)*((xma-
84  xmb)*(ymb-ymc)-(xmb-xmc)*(yma-ymb)))/((ymc-ymd)*((xma-xmb)*(zmb-zmc)-
85  (xmb-xmc)*(zma-zmb))-(xmc-xmd)*((yma-ymb)*(zmb-zmc)-(ymb-ymc)*(zma-
86  zmb))-(zmc-zmd)*((xma-xmb)*(ymb-ymc)-(xmb-xmc)*(yma-ymb)));
87
88  T = [e f g; h i j; k l m];
89
```

```
PCTM = PCTA' - T*PMA';

%The points of interests (bone landmarks, SGs position and directions, etc) in Microscribe coordinates are converted into CT coordinates (i.e. FE model coordinates)
%PointMS, array with the coordinates of the points of interest (POIs) in Microscribe coordinates (input)
%PointCT, array with the coordinates of the points of interest (POIs) in CT coordinates (output)
for i=1:n
    PointsCT(:,i)=PCTM+T*PointMS(i,:)';
end
```

D.2 Composition and formatting of the material property array (MATLAB)

```
Imx=imx; %CT image resolution width (pixels)
Imy=imy; %CT image resolution height (pixels)
Imz=imz; %CT image resolution depth (pixels)
Px=px; %pixel size (mm)
Py=py; %pixel size (mm)
Pz=pz; %slice thickness (mm)

Composicion=zeros(Imy,Imx,Imz);
dim1=(Imy+1)*Imz;
dim2=Imx+1;
Matxyz=zeros(dim1,dim2);

for i=1:Imz %3D Matrix from the CT image files
   %j=i;
   if (i<10)
   file=strcat('Dicom-00', num2str(i),'.txt');
   Composicion(:,:,i)=load(file);
   elseif (i>9)
   file=strcat('Dicom-0', num2str(i),'.txt');
   Composicion(:,:,i)=load(file);
   elseif (i>99)
   file=strcat('Dicom-', num2str(i),'.txt');
   Composicion(:,:,i)=load(file);
   end
end
for i=1:Imz %Reformatting in Ansys Table parameter array
   zz=1+(Imy+1)*(i-1);
   Matxyz(zz,1)=Pz*i-Pz;
   for cm=1:Imy
      for cn=1:Imx
         n=cn+1;
         m=1+(Imy+1)*(i-1)+cm;
         if (Composicion(cm,cn,i)>1)
         Matxyz(m,n)=int16((Composicion(cm,cn,i)-
calibration_intercept)/calibration_slope); %Transformation of HU into BMD from calibration phan-
toms
         else
            Matxyz(m,n)=0;
         end
         Matxyz(m,1)=Py*cm-Py;
         Matxyz(zz,n)=Px*cn-Px;
      end
   end
end
save BMDMatrix.txt Matxyz -ascii -tabs
```

D.3 Material properties assignment (ANSYS APDL)

```
/PREP7
*DIM,MaterialArray,table,ydim,xdim,zdim,Y,X,Z !Create new table array
*TREAD,MaterialArray,C:\Path\...\Filename,txt, ,0 !Read text file and write table array
BF,ALL,TEMP,%MaterialArray% !Assignment of material properties as node temperature
```

D.4 Calculation of the principal directions from the stress tensor of the isotropic model solutions (ANSYS APDL)

```
/POST1
*GET,Numelem,ELEM,0,COUNT
*DIM,Arrays,ARRAY,Numelem,6,1,,,
*DIM,Dirc,ARRAY,Numelem,9,1,,,
*DIM,stprinc,ARRAY,Numelem,3,1,,,
*DIM,direct,ARRAY,Numelem,6,1,,,

SET, FIRST
AVPRIN,0,,
ETABLE,S_X,S,X
AVPRIN,0,,
ETABLE,S_Y,S,Y
AVPRIN,0,,
ETABLE,S_Z,S,Z
AVPRIN,0,,
ETABLE,S_XY,S,XY
AVPRIN,0,,
ETABLE,S_YZ,S,YZ
AVPRIN,0,,
ETABLE,S_XZ,S,XZ
AVPRIN,0,,
ETABLE,S_1,S,1
AVPRIN,0,,
ETABLE,S_2,S,2
AVPRIN,0,,
ETABLE,S_3,S,3

*VGET,stprinc(1,1),ELEM,1,ETAB,S_1,,,2 !Get principal stresses
*VGET,stprinc(1,2),ELEM,1,ETAB,S_2,,,2
*VGET,stprinc(1,3),ELEM,1,ETAB,S_3,,,2

*VGET,Arrays(1,1),ELEM,1,ETAB,S_X,,,2 !Get stress tensor
*VGET,Arrays(1,2),ELEM,1,ETAB,S_Y,,,2
*VGET,Arrays(1,3),ELEM,1,ETAB,S_Z,,,2
*VGET,Arrays(1,4),ELEM,1,ETAB,S_XY,,,2
*VGET,Arrays(1,5),ELEM,1,ETAB,S_YZ,,,2
*VGET,Arrays(1,6),ELEM,1,ETAB,S_XZ,,,2
*VFUN,dirc(1,1),DIRCOS,arrays(1,1)

*CFOPEN,strprinc,dat,,, !Write file of principal stresses
*VWRITE,stprinc(1,1),stprinc(1,2),stprinc(1,3)
(F8.3,'       ',F8.3,'       ',F8.3)
*CFCLOS
```

```
44
45  *CFOPEN,dircoscomp,dat, , , !Write principal directions not in order
46  *VWRITE,dirc(1,1),dirc(1,2),dirc(1,3),dirc(1,4),dirc(1,5),dirc(1,6),dirc(1,7),dirc(1,8),d
47  irc(1,9)
48  (F6.4,'       ',F6.4,'       ',F6.4,'       ',F6.4,'       ',F6.4,'       ',F6.4,'       ',F6.4,'
49  ',F6.4,'       ',F6.4)
50  *CFCLOS
51
52  *DO,I,1,Numelem,1 ! Rank principal stresses and assignement of principal directions
53        *IF,stprinc(I,1),ABGT,stprinc(I,3),THEN
54        direct(I,1)=dirc(I,1)
55        direct(I,2)=dirc(I,2)
56        direct(I,3)=dirc(I,3)
57        *ELSE
58        direct(I,1)=dirc(I,7)
59        direct(I,2)=dirc(I,8)
60        direct(I,3)=dirc(I,9)
61        *ENDIF
62        direct(I,4)=dirc(I,4)
63        direct(I,5)=dirc(I,5)
64        direct(I,6)=dirc(I,6)
65  *ENDDO
66
67  *CFOPEN,directions,dat, , , !Write principal directions in descending order
68  *VWRITE,direct(1,1),direct(1,2),direct(1,3),direct(1,4),direct(1,5),direct(1,6)
69  (F6.4,'       ',F6.4,'       ',F6.4,'       ',F6.4,'       ',F6.4,'       ',F6.4)
70  *CFCLOS
```

D.5 Material directions assignment of the orthotropic models (ANSYS APDL)

```
/PREP7
*GET,Numelem,ELEM,0,COUNT
*DIM,dircos,ARRAY,Numelem,6,1, , ,
*VREAD,dircos(1,1),C:\Path\...\filename,dat,,JIK,6,Numelem,0
(F6.4,'       ',F6.4,'       ',F6.4,'       ',F6.4,'       ',F6.4,'       ',F6.4)

*DO,E,1,Numelem,1 !Assignment of principal directions to the element coordinate system
      icor=1000+E
      CSYS,0
      ESEL,s,ELEM,,E
      NSLE,s
      x_=CENTRX(E)
      y_=CENTRY(E)
      z_=CENTRZ(E)
      CSYS,4

WPLANE,1,x_,y_,z_,x_+dircos(E,1),y_+dircos(E,2),z_+dircos(E,3),x_+dircos(E,4),y_+
dircos(E,5),z_+dircos(E,6)
      CSWPLA,icor,0
      EMODIF,E,ESYS,icor
*ENDDO

*CFOPEN,dircosread,dat, , , !Check directions assignment
*VWRITE,dircos(1,1),dircos(1,2),dircos(1,3),dircos(1,4),dircos(1,5),dircos(1,6), , , ,
(F6.4,'       ',F6.4,'       ',F6.4,'       ',F6.4,'       ',F6.4,'       ',F6.4)
*CFCLOS
```

Bibliography

Anderson, A. E. (2007). Computational modeling of the hip joint mechanics. *PhD Thesis, The University of Utah.*

ANSYS Inc. (2010). Documentation Release 13.0.

Augat, P., Link, T., Lang, T. F., Lin, J. C., Majumdar, S., & Genant, H. K. (1998). Anisotropy of the elastic modulus of trabecular bone specimens from different anatomical locations. *Medical Engineering and Physics* (20): 124-131.

Bachus, K. N., DeMarco, A. L., Judd, K. T., Horwitz, D. S., & Brodke, D. S. (2006). Measuring contact area, force, and pressure for bioengineering applications: Using Fuji Film and TekScan systems. *Medical Engineering & Physics* (28): 483-488.

Banse, X., Delloye, C., Cornu, O., & Bourgois, R. (1996). Comparative left-right mechanical testing of cancellous bone from normal femoral heads. *Journal of Biomechanics* (29(10)): 1247-1253.

Bauchau, O. A., & Craig, J. (2009). *Structural Analysis.* Springer.

Bessho, M., Ohnishi, I., Matsuyama, J., Matsumoto, T., Imai, K., & Nakamura, K. (2007). Prediction of strength and strain of the proximal femur by a CT-based finite element method. *Journal of Biomechanics* (40): 1745-1753.

Bianchi, R., Clerici, P., & Miani, A. (1985). Quantitative and comparative stress analysis in human femur under two different static situations by three-dimensional photoelasticity. *The Anatomical Record* (211(3)): 323-328.

Borner, M., Bauer, A., & Lahmer, A. (1997). Computer-guided robot-assisted hip endoprosthesis. *Orthopade* (26): 251-257.

Bourne, B. C., & Meulen, M. C. (2004). Finite element models predict cancellous apparent modulus when tissue modulus is scaled from specimen CT-attenuation. *Journal of Biomechanics* (37): 613-621.

Bowman, S., Guo, X., Cheng, D., Keaveny, T., Gibson, L., & Hayes, W. (1998). Creep contributes to fatigue behavior of bovine trabecular bone. *Journal of Biomechanical Engineering* (120): 647-654.

BQS-Qualitätsreport. (2006). *BQS-Qualitätsreport.* Von www.bqs-qualitaetsreport.de abgerufen

Britton, J., Walsh, L., & Prendergast, P. (2003). Mechanical simulation of muscle loading on the proximal femur: analysis of cemented femoral component migration with and without muscle loading. *Clinical Biomechanics* (18): 637-646.

Burgers, T. A., Mason, J., Niebur, G., & Ploeg, H. L. (2008). Compressive properties of trabecular bone in the distal femur. *Journal of Biomechanics* (41): 1077-1085.

BVMed. (2007). *BVMed*. Von http://www.bvmed.de abgerufen

Canal, C. E., Hung, C. T., & Ateshian, G. A. (2008). Two-dimensional strain fields on the cross-section of the bovine humeral head undercontact loading. *Journal of Biomechanics* (41): 3145-3151.

Cann, C. E. (1988). Quantitative CT for determination of Bone mineral density: A Review. *Radiology* (166): 509-522.

Charlebois, M. (2008). Constitutive Law for Trabecular Bone in Large Strain Compression. *PhD Thesis, Technische Universität Wien* .

Charlebois, M., Pretterklieber, M., & Zysset, P. (2010). The role of fabric in the large strain compressive behavior of human trabecular bone. *J. Biomech. Eng.* (132(12)): 121006.

Chevalier, Y., Pahr, D., Allmer, H., Charlebois, M., & Zysset, P. (2007). Validation of a voxel-based FE method for prediction of the uniaxial apparent modulus of human trabecular bone using macroscopic mechanical tests and nanoindentation. *Journal of Biomechanics* (40): 3333-3340.

Ciarelli, M. J., Goldstein, S. A., Kuhn, J. L., Cody, D. D., & Brown, M. B. (1991). Evaluation of orthogonal mechanical properties and density of human trabecular bone from the mayor metaphyseal regions with materials testing and computed tomography. *Journal of Orthopaedic Research* (9): 674-682.

Cuppone, M., Seedhom, B. B., Berry, E., & Ostell, A. E. (2004). The Longitudinal Young's Modulus of Cortical Bone in the Midshaft of Human Femur and its Correlation with CT Scanning Data. *Calcif Tissue Int.* (74): 302-309.

Dagan, D., Be'ery, M., & Gefen, A. (2004). Single-trabecula building blocks for large-scale finite element models of cancellous bone. *Medical & Biological Engineering & Computing* (42): 549-556.

Dalstra, M., Huiskes, R., & Erning, A. O. (1993). Mechanical and textural properties of pelvic trabecular bone. *Journal of Biomechanics* (26(4)), pp. 523-535.

Davim, J. P., & Marques, N. (2004). Dynamical experimental study of friction and wear behaviour of bovine cancellous bone sliding against a metallic counterface in a water lubricated environment. *Journal of Materials Processing Technology* (152(3)): 389-394.

Dendorfer, S., Maier, H., & Hammer, J. (2009). Fatigue damage in cancellous bone: An experimental approach from continuum to micro scale. *Journal of mechanical behavior of biomedical materials* (2(1)): 113-119.

Dendorfer, S., Maier, H., Taylor, D., & Hammer, J. (2008). Anisotropy of the fatigue behaviour of cancellous bone. *Journal of Biomechanics* (41): 636-641.

Doblare, M., & Garcia, J. (2001). Application of an anisotropic bone-remodellingmodel based on a damage-repair theory to the analysis of the proximal femur before and after total hip replacement. *Journal of Biomechanics* (34): 1157-1170.

Dong, X., & Guo, X. (2004). The dependence of transversely isotropic elasticity of human femoral cortical bone on porosity. *Journal of Biomechanics* (37): 1281-1287.

Doube, M., Kłosowski, M. M., Arganda-Carreras, I., Cordelières, F. P., Dougherty, R. P., Jackson, J. S., et al. (2010). BoneJ: free and extensible bone image analysis in ImageJ. *Bone* (46(6)): 1076-1079.

Dphil, J. C. (2009). Measurement of the Mechanical Properties of Bone. *Clin Orthop Relat Res* (467): 1948-1954.

Drewniak, E. I., Crisco, J. J., Spenciner, D. B., & Fleming, B. C. (2007). Accuracy of circular contact area measurements with thin-film pressure sensors. *Journal of Biomechanics* (40): 2569-2572.

Eswaran, S., Gupta, A., & Keaveny, T. (2007). Locations of bone tissue at high risk of initial failure during compressive loading of the human vertebral body. *Bone* (41): 733-739.

Finlay, J. B., Chess, D. G., Hardie, W. R., Rorabeck, C. H., & Bourne, a. R. (1991). An Evaluation of Three Loading Configurations for the In Vitro Testing of Femoral Strains in Total Hip Arthroplasty. *Journal of Orthopaedic Research* (9): 749-759.

Ford, C. M., & Keaveny, T. (1996). The dependence of shear failure properties of trabecular bone on apparent density and trabecular orientation. *Journal of Biomechanics* (29(10)): 1309-1317.

Fregly, B. J., & Sawyer, G. W. (2003). Estimation of discretization errors in contact pressure measurements. *Journal of Biomechanics* (36(4)): 609-613.

Fujii, G.-Z. J., Matsumoto, H., Gunji, M. H., Hakozaki, K., & Akira, Y. A. (2008). Correlation among geometric, densitometric, and mechanical properties in mandible and femur of osteoporotic rats. *J. Bone Miner. Metab.* (26): 130-137.

Fung, Y. (1993). *Biomechanics. Mechanical properties of living tissues.* New York: Springer.

Geraets, W., Ruijven, L. v., Verheij, J., Stelt, P. v., & Eijden, T. v. (2008). Spatial orientation in bone samples and Young's modulus. *Journal of Biomechanics* (41): 2206-2210.

Gore, D. R., Murray, M. P., Gardner, G. M., & Sepic, S.B. (1977). Roentgenographic Measurements after Muller Total Hip Replacement. *Journal of Bone and Joint Surgery Am.* (59): 948-53.

Goulet, R. W., Goldstein, S. A., Ciarelli, M. J., Kuhn, J. L., & Feldkamp, M. B. (1994). The relationship between the structural and orthogonal compressive properties of trabecular bone. *Journal of Biomechanics* (27(4)): 375-389.

Grimal, Q., Haupert, S., Mitton, D., Vastel, L., & Laugier, P. (2009). Assessment of cortical bone elasticity and strength: Mechanical testing and ultrasound provide complementary data. *Medical Engineering & Physics* (31): 1140-1147.

Hall, S. (2007). *Basic Biomechanics. Fifth Edition.* McGraw-Hill.

Hamed, E., Lee, Y., & Jasiuk, I. (2010). Multiscale modeling of elastic properties of cortical bone. *Acta Mech.* (213): 131-154.

Handels, H., Ehrhardt, J., Plotz, W., & Poppl, S. (2001). Simulation of hip operations and design of custom-made endoprostheses using virtual reality techniques. *Methods Inf. Med.* (40): 74-77.

Hangartnera, T. N., & Short, D. F. (2007). Accurate quantification of width and density of bone structures by computed tomography. *Med. Phys* (34(10)): 3777-3784.

Heimkes, T. P.-M. (2009). Function-Orientated Structural Analysis of the Proximal Human Femur. *Cell Tissues Organs* (190): 247-255.

Hoffmeister, B. K., Smith, S., Handley, S., & Rho, J. (2000). Anisotropy of Young's modulus of human tibial cortical bone. *Med. Biol. Eng. Comput.* (38): 333-338.

Huiskes, R. (2000). If bone is the answer, then what is the question? *Journal of Anatomy* (197): 145-156.

Jensen, J. S. (1978). A photoelastic study of a model of the proximal femur. *Acta orthop Scand* : 54-59.

Joshi, M. G., Advani, S. G., Miller, F., & Santare, M. H. (2000). Analysis of a femoral hip prosthesis designed to reduce stress shielding. *Journal of Biomechanics* (33): 1655-1662.

Juszczyk, M. M., Cristofolini, L., & Viceconti, M. (2011). The human proximal femur behaves linearly elastic up to failure under physiological loading conditions. *Journal of Biomechanics* (44(12)): 2259-2266.

Kaneko, T. S., Bell, J. S., Pejcic, M. R., Tehranzadeh, J., & Keyak, J. H. (2004). Mechanical properties, density and quantitative CT scan data of trabecular bone with and without metastases. *Journal of Biomechanics* (37): 523-530.

Kaneko, T. S., Pejcic, M. R., Tehranzadeh, J., & Keyak, J. H. (2003). Relationships between material properties and CT scan data of cortical bone with and without metastatic lesions. *Medical Engineering & Physics* (25): 445-454.

Keaveny, T. M., Borchers, R. E., Gibson, L. J., & Hayes, W. C. (1993). Theretical analysis of the experimental artifact in trabecular bone compressive modulus. *Journal of Biomechanics* (26(4)): 599-607.

Keaveny, T. M., Borchers, R. E., Gibson, L. J., & Hayes, W. C. (1993). Trabecular Bone modulus and stength can depend on specimen geometry. *Journal of Biomechanics* (26-8): 991-1000.

Keaveny, T. M., Guo, E., Wachtel, E. F., McMahon, T. A., & Hayes, W. C. (1994). Trabecular bone exhibits fully linear elastic behavior and yields at low strains. *Journal of Biomechanics* (27-9): 1127-1136.

Keaveny, T. M., Pinilla, T. P., Crawford, R. P., Kopperdahl, D. L., & Lou, A. (1997). Systematic and ramdom errors in compression testing of trabecular bone. *Journal of Orthopaedic Research* (15(1)): 101-110.

Keller, T. S. (1994). Predicting the compressive mechanical behavior of bone. *Journal of Biomechanics* (27-9): 1159-1168.

Keyak, J. H., & Falkinstein, Y. (2003). Comparison of in situ and in vitro CT scan-based finite element model predictions of proximal femoral fracture load. *Medical Engineering & Physics* (25): 781-787.

Keyak, J. H., Lee, I. Y., & Skinner, a. H. (1994). Correlations between orthogonal mechanical properties and density of trabecular bone: Use of different densitometric measures. *Journal of biomedical materials research* (28): 1329-1336.

Keyak, J. (2001). Improved prediction of proximal femoral fracture load using nonlinear finite element models. *Medical Engineering & Physics* (23): 165-173.

Keyak, J., Fourkas, M., Meagher, J., & and Skinner, H. (1993). Validation of Automated Method of Three-Dimensional Finite Element Modelling of Bone. *J. Biomed. Eng.* (15): 505-509.

Keyak, J., Lee, I., & Skinner, H. (1994). Correlations between orthogonal mechanical properties and density of trabecular bone: Use of different densitometric measures. *Journal of biomedical materials research* (28): 1329-1336.

Keyak, J., Meagher, J., Skinner, H., & Mote, J. C. (1990). Automated three-dimensional finite element modelling of bone: a new method. *J. Biomed. Eng.* (12): 389-397.

Laza, P. J., Stowe, J. Q., Baldwin, M. A., Petrella, A. J., & Rullkoetter, P. J. (2007). Incorporating uncertainty in mechanical properties for finite element-based evaluation of bone mechanics. *Journal of Biomechanics* (40): 2831-2836.

Leppanen, O. V., Sievanen, H., & Jarvinen, T. L. (2008). Biomechanical testing in experimental bone interventions —May the power be with you. *Journal of Biomechanics* (41): 1623-1631.

Liggins, A., Hardie, W., & Finlay, J. (June 1995). The spatial and pressure resolution of Fuji Pressure sensitive film. *Experimental Mechanichs* (35(2)): 166-173.

Linde, F., & Hvid, I. (1989). The effect of constraint on the mechanical behavior of trabecular bone specimens. *Journal of Biomechanics* (22(5)): 485-490.

Linde, F., Christian, H., & Sorensen, F. (1993). The effect of different storage methods on the mechanical properties of trabecular bone. *Journal of Biomechanics* (25): 359-368.

Linde, F., Hvid, I., & Madsen, F. (1992). The effect of specimen geometry on the mechanical behavior of trabecular bone specimens. *Journal of Biomechanics* (25(4)): 359-368.

Link, T. M., Majumdar, S., Lin, J. C., Newitt, D., Augat, P., Ouyang, X., et al. (1998). A Comparative Study of Trabecular Bone Properties in the Spine and Femur Using High Resolution MRI and CT. *Journal of Bone and mineral research* (13): 122-132.

Lotz, J. C., Gerhart, T. N., & Hayes, W. C. (1990). Mechanical properties of trabecular bone from the proximal femur: A quantitative CT Study. *Journal of Computer Assisted Tomography* (14): 107-114.

Love, A. (1927). *A treatise on the mathematical theory of elasticity.* Cambridge University Press.

Majumdar, S., Kothari, M., Augat, P., Newitt, D. C., Link, T. M., Lin, J. C., et al. (1998). High-Resolution Magnetic Resonance Imaging: Three-Dimensional Trabecular Bone Architecture and Biomechanical Properties. *Bone* (25(5)): 445-454.

Malchau, H., Herberts, P., Eisler, T., Garellick, G., & Söderman, P. (2002). The Swedish Total Hip Replacement Register. *Journal of bone and joint surgery. American Volume* (84(4) Suppl. 2): 2-20.

Martin, R. B. (1998). *Skeletal Tissue Mechanics.* New York: Springer-Verlag, ISBN: 0-387-98474-7.

Matsuura, M., Eckstein, F., Lochmüller, E.-M., & Zysset, P. K. (2008). The role of fabric in the quasi-static compressive mechanicalproperties of human trabecular bone from various anatomical locations. *Biomechan. Model Mechanobiol* (7): 27-42.

MatWeb, L. (kein Datum). *Online Materials Information Resource - MatWeb*. (MatWeb, LLC) Von www.matweb.com abgerufen

McDermott, I., Lie, D., Edwards, A., Bull, A., & Amis, A. (2008). The effects of lateral meniscal allograft transplantation techniques on tibio-femoral contact pressures. *Knee Surg Sports Traumatol Arthrosc* (16): 553-560.

Mertz, B., Niederer, P., Muller, R., & Ruegsegger, P. (1996). Automated Finite Element Analysis of Excised Human Femura Based on Precision-QCT. *J. Biomech. Eng.* (118): 387-390.

Moisio, K., Podolskaya, G., Barnhart, B., Berzins, A., & Sumner, D. (2003). pQCT provides better prediction of canine femur breaking load than does DXA. *J Musculoskelet Neuronal Interact* (3(3)): 240-245.

Morgan, Elise F., Bayraktar, Harun H. & Keaveny, Tony M. (2003). Trabecular bone modulus–density relationships depend on anatomic site. *Journal of Biomechanics (36*): 897-904.

Moore, T. L., & Gibson, L. J. (2003). Fatigue of bovine trabecular bone. *Journal of Biomechanical Engineering* (125): 761-768.

Mulder, G., Renders, L., Langenbach, G., Ruijven, L. v., & Eijden, T. v. (2008). Biomechanical effect of mineral heterogeneity in trabecular bone. *Journal of Biomechanics* (41): 1793-2798.

Nazarian, A., Stechow, D. v., Zurakowski, D., Müller, R., & Snyder, B. D. (2008). Bone Volume Fraction Explains the Variation in Strength and Stiffness of Cancellous Bone Affected by Metastatic Cancer and Osteoporosis. *Calcif. Tissue Int.* (83): 368-379.

Niethard, K. B. (2004). Anatomical and biomechanical investigations of the iliotibial tract. *Surg. Radiol. Anat.* (26): 433-446.

Odgaard, A., & Linde, F. (1991). The underestimation of young's Modulus in compressive testing of cancellous bone specimens. *Journal of Biomechanics* (24(8)): 691-698.

Öhman, C., Baleani, M., Perilli, E., Dall'Ara, E., Tassani, S., Baruffaldi, F., et al. (2007). Mechanical testing of cancellous bone from the femoral head: Experimental errors due to off-axis measurements. *Journal of Biomechanics* (40): 2426-2423.

Pahr, D. H., & Zysset, P. K. (2009). From high-resolution CT data to finite element models: development of an integrated modular framework. *Computer Methods in Biomechanics and Biomedical Engineering* (12): 45-47.

Palomar, A. P., Calvo, B., & Doblare, M. (2008). An accurate finite element model of the cervical spine under quasi-static loading. *Journal of Biomechanics* (41): 523-531.

Park, M. C., Cadet, E. R., Levine, W. N., Bigliani, L. U., & Ahmad, C. S. (2005). Tendon-to-Bone Pressure Distributions at a Repaired Rotator Cuff Footprint Using Transosseous Suture and Suture Anchor Fixation Techniques. *American Journal of Sports Medicine* (33), pp. 1154-1159.

Park, Y., Albert, C., Yoon, Y.-S., Fernlund, G., Frei, H., & Oxland, T. R. (2010). The effect of abductor muscle and anterior-posterior hip contact load simulation on the in-vitro primary stability of a cementless hip stem. *Journal of Orthopaedic Surgery and Research* (5(40)).

Peng, L., Bai, J., Zeng, X., & Zhou, Y. (2006). Comparison of isotropic and orthotropic material property assignments on femoral finite element models under two loading conditions. *Medical Engineering & Physics* (28): 227-233.

Perilli, E., Baleani, M., Ohman, C., Fognani, R., Baruffaldi, F., & Viceconti, M. (2008). Dependence of mechanical compressive strength on local variations in microarchitecture in cancellous bone of proximal human femur. *Journal of Biomechanics* (41): 438-446.

Polgar, K., Gill, H. S., Viceconti, M., Murray, D. W., & O'Connor, J. J. (2003). Strain distribution within the human femur due to physiological and simplified loading: Finite element analysis using the muscle standardized femur model. *Proceedings of the Institution of Mechanical Engineers, Part H: Journal of Engineering in Medicine* (217(3)): 173-189.

Prevrhal, S., & Gennat, H. (1999). Quatitative Computertomographie. *Radiologie* (39): 194-202.

Ramos, A., Fonseca, F., & Simões, J. (2006). Simulation of Physiological Loading in Total Hip Replacements. *J. Biomech. Eng.* (128): 579-587.

Renders, G., Mulder, L., Langenbach, G., Ruijven, L. v., & Eijden, T. v. (2008). Biomechanical effect of mineral heterogeneity in trabecular bone. *Journal of Biomechanics* (41): 2793-2798.

Rho, B. K. (2000). Anisotropy of Young's modulus of human tibial cortical bone. *Med. Biol. Eng. Comput.* (38): 333-338.

Rho, J. Y., Hobatho, M., & Ashman, R. (1995). Relations of mechanical properties to density and CT numbers in human bone. *Medical Engineering & Physics* (17(5)): 347-355.

Rho, J., Ashman, R., & Turner, H. (1993). Young'smodulus of trabecular and cortical bone material: ultrasonic and microtensile measurements. *Journal of Biomechanics* (26): 111-119.

Rohl, L., Larsen, E., Linde, F., Odgaard, A., & Jorgensen, J. (1991). Tensile and Compressive properties of cancellous bone. *Journal of Biomechanics* (24(12)): 1143-1149.

Rudman, K., Aspden, R., & Meakin, J. (2006). Compression or tension? The stress distribution in the proximal femur. *Biomedical Engineering OnLine* (5(12)): 1-7.

Ruijven, W. G., Verheij, J., Stelt, P. v., & Eijden, T. v. (2008). Spatial orientation in bone samples and Young's modulus. *Journal of Biomechanics* (41): 2206-2210.

Saparin, P., Thomsen, J. S., Kurths, J., Beller, G., & Gowin, W. (2006). Segmentation of bone CT images and assessment of bone structure using measures of complexity. *Med. Phys* (33(10)): 3857-3873.

Sasso, M., Haıat, G., Yamato, Y., Naili, S., & Matsukawa, M. (2008). Dependence of ultrasonic attenuation on bone mass and microstructure in bovine cortical bone. *Journal of Biomechanics* (41): 347-355.

Sciavicco, L., & Siciliano, B. (2000). *Modelling and Control of Robot Manipulators. Advanced Textbooks in Control and Signal Processing series.* Springer.

Sharpe, W. N., & Sharpe, J. W. (2008). *Handbook of Experimental Solid Mechanics.* Springer.

Sigal, I. A., Hardisty, M. R., & Whyne, C. M. (2008). Mesh-morphing algorithms for specimen-specific finite element modeling. *Journal of Biomechanics* (41): 1381-1389.

Siu, W. S., Qin, L., & Leung, a. K. (2003). pQCT bone strength index may serve as a better predictor than bone mineral density for long bone breaking strength. *J. Bone Miner. Metab.* (21): 316-322.

Skuban, T. P., Vogel, T., Baur-Melnyk, A., Jansson, V., & Heimkes, B. (2009). Function-Orientated Structural Analysis. *Cells Tissues Organs* (190): 247-255.

Speirs, A. D., Heller, M. O., Duda, G. N., & Taylor, W. R. (2007). Physiologically based boundary conditions in finite element modelling. *Journal of Biomechanics* (40): 2318-2323.

Taddei, F., Schileo, E., Helgason, B., Cristofolini, L., & Viceconti, M. (2007). The material mapping strategy influences the accuracy of CT-based finite element models of bones: An evaluation against experimental measurements. *Medical Engineering & Physics* (29): 973-979.

Taylor, W., Roland, E., Ploeg, H., Hertig, D., Klabunde, R., Warner, M., et al. (2002). Determination of orthotropic bone elastic constants using FEA and modal analysis. *Journal of Biomechanics* (35): 767-773.

Tenga, Z., Ochoa, I., Li, Z., Lin, Y., Rodriguez, J. F., Bea, J. A., et al. (2008). Nonlinear mechanical property of tracheal cartilage: A theoretical and experimental study. *Journal of Biomechanics* (41): 1995-2002.

Trabelsi, N., & Yosibash, Z. (2011). Patient-Specific Finite-Element Analyses of the Proximal Femur with Orthotropic Material Properties Validated by Experiments. *Journal of Biomechanical Engineering* (133(6)): 061001.

Trabelsi, N., Yosibash, Z., Wutte, C., Augat, P., & Eberle: (2011). Patient-specific finite element analysis of the human femur—A double-blinded biomechanical validation. *J. Biomechanics* (44): 1666-1672.

Turner, C. H., Rho, J., Takano, Y., Tsui, T. Y., & Pharr, G. M. (1999). The elastic properties of trabecular and cortical bone tissues are similar: results from two microscopic measurement techniques. *Journal of Biomechanics* (32): 437-441.

Verhulp, E., Rietbergen, B. v., & Huiskes, R. (2008). Load distribution in the healthy and osteoporotic human proximal femur during fall to the side. *Bone* (42): 30-35.

Viceconti, M., Bellingeri, L., Cristofolin, L., & Toni, A. (1998). A comparative study on different methods of automatic mesh generation of human femurs. *Medical Engineering & Physics* (20): 1-10.

Viceconti, M., Chiarini, A., Testi, D., Taddei, F., Bordini, B., Traina, F., et al. (2004). New aspects and approaches in pre-operative planning of hip reconstruction: a computer simulation. *Langenbecks Arch. Surg.* (389): 400-404.

Wald, M. J. (2010). Mapping Trabecular Bone Fabric Tensor by in Vivo Magnetic Resonance Imaging. *PhD. thesis, University of Pennsylvania* .

Wirtz, D. C., Pandorf, T., Portheine, F., Radermacher, K., Schiffers, N., Prescher, A., et al. (2003). Concept and development of an orthotropic FEmodel of the proximal femur. *Journal of Biomechanics* (36): 289-293.

Wirtz, D. C., Schiffers, N., Pandorf, T., Radermacher, K., Weichert, D., & Forst, R. (2000). Critical evaluation of known bone material properties to realize anisotropic FE-simulation of the proximal femur. *Journal of Biomechanics* (33): 1325-1330.

Wirtz, D.C., & Niethard, F.U. (1997). Hüftendoprothesenlockerung – eine Standortbestimmung. Z. *Orthop* (135): 257-270.

Xiong, Y., Zhao, Y., Xing, S., Du, Q., Sun, H., Wang, Z., et al. (2010). Comparison of interface contact profiles of a new minimum contact locking compression plate and the limited contact dynamic compression plate. *International Orthopaedics* (34): 715-718.

Yang, H., Ma, X., & Guo, T. (2010). Some factors that affect the comparison between isotropic and orthotropic inhomogeneous finite element material models of femur. *Medical Engineering & Physics* (32): 553-560.

Yoon, Y., & Cowin, S. (2008). The Estimated Elastic Constants for a Single Bone Osteonal Lamella. *Biomech Model Mechanobiol.* (7): 1-11.

Yosibash, Z., Padan, R., Joskowicz, L., & Milgrom, C. (2007). A CT-Based High-Order Finite Element Analysis of the Human Proximal Femur Compared to In-vitro Experiments. *Journal of Biomechanical Engineering* (129): 297-309.

Yosibash, Z., Trabelsi, N., & Milgrom, C. (2007). Reliable simulations of the human proximal femur by high-order finite element analysis validated by experimental observations. *Journal of Biomechanics* (40): 3688-3699.

Zannoni, C., Mantovani, R., & Viceconti, M. (1998). Material properties assignment to finite element models of bone structures: a new method. *Medical Engineering & Physics* (20): 735-740.

Zhang, J., Niebur, G. L., & Ovaert, T. C. (2008). Mechanical property determination of bone through nano- and micro-indentation testing and finite element simulation. *Journal of Biomechanics* (41): 267-275.

Zhu, M., Keller, T. S., & Spengler, D. M. (1994). Effects of specimen load-bearing and free surface layers on the compressive mechanical properties of cellular materials. *Journal of Biomechanics* (27(1)): 57-66.

Zysset, P. (1994). A Constitutive Law for Trabecular Bone. *PhD. Thesis, École Polytechnique Fédérale de Lausanne* .

Zysset, P. K., Guo, X. E., Hoffler, C. E., Moore, K. E., & Goldstein, S. A. (1999). Elastic modulus and hardness of cortical and trabecular bone lamellae measured by nanoindentation in the human femur. *Journal of Biomechanics* (32): 1005-1012.